Nanofluidics for Biomolecular Separations

By

Michael Andrei Startsev

A thesis submitted to Macquarie University
for the degree of
Doctor of Philosophy
Department of Physics and Astronomy
November 2015

Typeset in LaTeX 2_ε.

Except where acknowledged in the customary manner, the material presented in this thesis is, to the best of my knowledge, original and has not been submitted in whole or part for a degree in any university.

Michael Andrei Startsev

Acknowledgements

I would like to thank my supervisor, Dr. David Inglis, for his encouragement when I was in doubt, his equanimity when experiments didn't work, and for his guidance when I lost my way. I would also like to thank Professor Ewa Goldys for her guidance earlier in my research and for arranging the Biofocus conferences that I found fascinating. Thank you to Dr. Martin Ostrowski for his guidance in extracting Bacillus cereus DNA and for permitting me to use his facilities despite the administrative difficulties that followed. Thanks to Joanna Szymanska for repeatedly performing thermal oxide growths on my many wafers in the University of New South Wales. Thank you Ben Johnson for permitting me to use the wafer dicer and the oven so many times.

Thank you to Annemarie Nadort for sharing those moments of casual conversation in the office with me to unwind the tension, and for inviting me to your 30's themed party which turned out to be such a good time. Thank you, Christian Leiterer for accompanying me in experiments and offering a critical perspective when I needed one. Also, thanks for keeping me company in the clean room when I had to work with acids. I didn't burn myself even once, so I consider that a success. Thanks to Michael Nguyen for sharing some of the interesting work you were doing with droplet microfluidics. Thank you Artur Sawiki for assisting me with assembling the gel electrophoresis equipment and for opening doors for me when I didn't have keys to the lab. Thanks to all the students in E7B-148 for sharing this experience with me.

List of Publications

- Michael A. Startsev, David W. Inglis, Mark S. Baker, Ewa M. Goldys *Nanochannel pH Gradient Electrofocusing of Proteins.* Analytical Chemistry **2013** 85(15), pp 7133 - 7138

- Michael A. Startsev and Abdulhakem Y. Elezzabi *Terahertz Frequency Continuous-Wave Spectroscopy and Imaging of Explosive Substances.* ISRN Optics, vol. 2013, Article ID 419507, 8 pages doi:10.1155/2013/419507

- Cameron J. E. Straatsma, Michael A. Startsev, Abdulhakem Y. Elezzabi *An Investigation of Terahertz Particle Plasmons: Affect of Particle Size on the Transparency of a Metallic Particle Ensemble.* Journal of infrared, millimeter and terahertz waves; **2010** 31(6), pp 659-666. DOI:10.1007/s10762-010-9623-2

- Wei-Lun Hsu; David W. Inglis; Michael A. Startsev; Ewa M. Goldys; Malcolm R. Davidson; Dalton J.E. Harvie *Isoelectric Focusing in a Silica Nanofluidic Channel: Effects of Electromigration and Electroosmosis.* Analytical Chemistry; **2014** 86(17), pp 8711-8718

Conferences and other contributions

- Presentation at the 20th Australian Institute of Physics Congress "pH Gradient Electrofocusing for Proteomics" Michael A Startsev, David W Inglis, Ewa M Goldys, Macquarie University, Sydney NSW 2109, Australia

- W.L. Hsu, M. A. Startsev, D. W. Inglis, E. M. Goldys, M. R. Davidson and D. J. E. Harvie 17th International Conference on Miniaturized Systems for Chemistry and Life Sciences 27-31 October 2013, Freiburg, Germany, pp. 766-768, (2013).

Professional Service

- Peer review for the Journal of Infrared, Millimeter, and Terahertz Waves. Peer review for Lab on a Chip (www.rsc.org/loc). Peer review for Journal of Applied Physical Science International.
- Seminar coordinator for the MQ Biofocus Research Centre (2011-2013)

Abstract

Nanofluidics, microfluidics and lab-on-a-chip technology has garnered much attention in recent years due to the opportunities it offers in analytical chemistry and point-of-care. However, an understanding of the physicochemical phenomena associated with biomolecular separations within nanofluidic devices is needed to enable those possibilities. The work presented in this manuscript describes a novel nanofluidic device designed to simultaneously separate and concentrate dilute biomarkers within low volume samples. The mechanism of separation driving biomolecules within the nanofluidic device is the continuous counteracting forces of electrophoresis and electro-osmosis in the presence of a spatial gradient that modulates molecular mobility (conductivity gradient or pH gradient) induced along the nanochannels of the device.

R-phycoerythrin, streptavidin-Dylight, DNA, and PNA (peptide nucleic acid) were focused and separated within the nanochannel under various conditions and their respective behaviours were characterized. A pH gradient was applied along the nanochannel device by introducing two different pH buffers at opposite terminals of the nanochannel and applying an axial voltage across the channel. Fluorescent proteins, phycoerythrin and Dylight labelled streptavidin, were concentrated within the channel reaching concentration enhancement (CE) factors of over 380 within 5 minutes. A conductivity gradient was also applied along the nanochannel by introducing buffers of dissimilar salt concentrations at the terminals of the nanochannel in order to create a trapping condition similar to the pH gradient method. Simultaneous separation and concentration of Bacillus cereus DNA and R-phycoerythrin was achieved to a CE of over 900. The conductivity gradient technique was also used to detect hybridization between oligonucleotides and complementary strands of PNA. This work illustrates how these electrofocusing devices are capable of matrix-free separation and concentration of biomarkers. In the future, this technology may enable on-chip integration of orthogonal separation techniques with mass spectrometry.

Contents

List of Figures

List of Tables

1 Introduction

Biomolecular analysis, dealing with the separation and identification of various biomarkers (in the form of proteins, DNA, metabolites, etc) presents countless diagnostics opportunities, from the detection of rare genetic disorders to the development of personalized drug treatments. While DNA encodes genetic instructions for the growth and function of all known organisms, proteins are the main components of the metabolic pathways of cells, acting in enzyme catalysis, transport, mechanical support, organelle constituents, storage reserves, metabolic control, and osmotic pressure control (and many more). The study of DNA and proteins can elucidate the mechanisms by which many diseases and disorders evolve. Characterizing these biomarkers within their complex biological fluids is essential for understanding disease since they often result from changes in DNA structure or changes in global protein expression.

1.1 Motivation for a Nanofluidics Approach

Microscale (< 1 um) and nanoscale (< 100 nm) fluidic separation techniques present unique advantages in terms of process automation and miniaturization [1]. Often times, protein samples of interest are found in restrictively small quantities and up-scaling the samples to detectable levels can be infeasible or prohibitively costly. For instance, if

one wished to investigate the protein population contained within a single cell, the conventional desk-top methods such as 2D electrophoresis and traditional flow-based enzyme-linked immunosorbent assays ELISA [2] would be unsuitable without first amplifying the targeted biomarkers to a reasonable detectable concentration. However, nanostructure geometry devices are inherently ideal for dealing with such small volumes of analytes. It was the microscale nature of capillary electrophoresis (CE) that made possible the completion of the human genome project earlier than expected and within budget [3]. Further advancement of microfluidics separation on chip architectures may make a similar contribution to other "omics" fields, such as proteomics, metabolomics, lipidomics etc.

In addition to the benefit of working with smaller analyte volumes, nanofluidics offers possible cost savings owing to reduced consumption of expensive reagents, faster turnaround times, and fewer personnel requirements. In the future, nanofluidic separation of biomarkers may be automated and computer controlled on miniaturized lab-on-chip devices, enabling untrained individuals to perform what would otherwise be complex and expensive analyses. Since it is possible to perform analysis in nanofluidic arrays, throughput of analysis may also be improved.

The physics at nanoscale may prove to be advantageous and interesting in its own right. At nanofluidic scales, physical effects that are otherwise negligible become significant. Fluid viscosity behaves differently and electric double layer (EDL) surface effects, such as electro-osmotic forces, take part in the motion of particles. In a microfluidic channel, bulk fluid flow can be induced with electroosmotic drag force that creates a nearly uniform velocity profile, which has several advantages over a pressure induced "plug-like" velocity profile. An electro-osmotic flow profile results in reduced sample species dispersion which not only improves a device's capability for mixing and molecular separation, but also has promising applications in fluid pumping and non-mechanical valves. A second electrokinetic phenomenon present within micro/nanofluidic devices is electrophoresis: motion of dispersed particles relative to surrounding fluid under the influence of a spatially uniform electric field. Electrophoresis is used in conventional polyacrylamide gel electrophoresis (PAGE) to separate DNA and RNA according to their size but it is readily applied to novel nanofluidic applications.

Given these methods of molecular motion, we can manipulate the behaviour of biomarkers within a fluid but also possibly combine these methods with conventional techniques to create more effective and versatile devices.

One example of a potential application for nanofluidic biomolecular separations is proteomics research in autoimmune disorders such as Celiac disease (CD) which is

characterized by small-intestinal mucosal injury and nutrient malabsorption. CD autoimmune reaction has a defined trigger in the body: gluten proteins from ingested wheat or cereals in the presence of HLA-DQ2 or HLA-DQ8 serotypes [4]. The standard methods of testing for the disorder requires a small-intestine biopsy. Shamir et al. [5] demonstrated a method to diagnose CD by applying ELISA analysis to detect Immunoglobulin A (IgA) anti-endomysial antibodies (EMA) that are specific to CD. However, these techniques are limited since they depend on the quantity of EMA within the sample[6] and also require multiple process steps that must be carried out by trained professionals. Considering the advantages of nanofluidics/microfluidics discussed earlier, it can be envisaged that a nanofluidic approach could be a faster, cheaper, and simpler method to detect these antibodies.

While microfluidic biochips are growing progressively more complex, and more common in industry, reliable models of electroosmosis and electrophoresis are lacking, especially when used in concert. Recently, many nanofluidics studies [7][8][9] have been concerned with biomarker preconcentration in order to increase the detection sensitivity of trace analytes. However, when investigating protein biomarkers found in complex media such as blood plasma, preconcentration is unlikely to improve detectability. The novel nanofluidic device studied in this thesis functions upon the idea that, by placing a electrokinetic mobility modulating gradient within a nanochannel, continuous separation and concentration of biomarkers can be performed simultaneously. Biomarkers may be trapped and concentrated at unique points along the nanochannel depending on the biomarker's mobility properties which are affected by the gradient. Two types of gradients are studied in this manuscript: pH gradients, and conductivity gradients (salt concentration gradients).

1.2 Gradient Electrofocusing

As mentioned previously, the electrofocusing techniques of greatest interest to this project are counter-flow gradient methods wherein two counteracting forces within the device act upon the analyte. Typically, a gradient of some transport variable is induced along the channel such that, under an electric field, the mobilities of molecules or the acting forces within the device are modulated along the channel thus resulting in travelling molecular separations (e.g. CE and isotachophoresis [10]) or stationary focusing locations (e.g. Isoelectric focusing). The following is a list of the various possible approaches to inducing a gradient for the purpose of electrofocusing. Each item is described in further detail below.

- **Chromatographic Velocity Focusing** – A hydrodynamic (bulk solution flow) velocity gradient is generated along the device. Protein charge, current, and conductivity is held constant throughout the channel. This is demonstrated in counteracting chromatographic electrophoresis (CACE).

- **pH Gradient Focusing** – proteins having a charge dependent on local pH, focus at a location along the gradient where the protein net charge becomes zero (e.g. Isoelectric focusing). Hydrodynamic velocity may be zero.

- **Conductivity Gradient Focusing** – A conductivity gradient is created in the focusing channel. Hydrodynamic velocity, protein charge and axial current is held constant.

- **Current Gradient Focusing** – Axial current gradient is generated within along the device. Hydrodynamic velocity, protein charge, and conductivity is held constant.

- **Mobility Gradient Focusing** – A mobility gradient is created along the focusing channel. Chromatographic velocity, protein charge, conductivity, and current is held constant. This method is theoretically possible but has not been demonstrated in experiment yet [11]. One possible way to accomplish this may be to use a chaotropic agent such as urea or an organic solvent like acetonitrile to partially unfold a protein population and then analyze that population using a reverse gradient to fractionate the unfolded forms.

1.2.1 Chromatographic Velocity Focusing

In 1985, O'Farrell described a technique of counteracting chromatographic electrophoresis (CACE) [12]. He was motivated by some of the major drawbacks of IEF such as poor solubility and degradation of analytes at their isoelectric points. O'Farrell's technique was independent from the isoelectric point focusing. Instead, O'Farrel created a discrete junction between two different gels packed in a column. An electric field drove the proteins electrophoretically and a counteracting hydrodynamic flow was applied. The proteins experience high electrophoretic velocity in one gel and low electrophoretic velocity in the other. In this way, the proteins would travel quickly in the high velocity gel, slow in the low velocity gel and eventually focus at the gel interface. CACE was shown to focus proteins at high concentrations but it was difficult to use this process for separation of protein mixtures and the separations are typically time consuming.

Ivory and Gobie [13] developed a method of continuous feed CACE that was able to achieve binary protein separations. However, the limitations of CACE mentioned above prevented its widespread use.

1.2.2 PH Gradient Focusing

The earliest attempts at protein separation and focusing were based on pH gradient methods. In the mid 1950's, Kolin [14] was the first to establish a pH gradient separation system using acidic solutions at the anode and alkaline in the cathode of his device. The anode and cathode of the device are set at different voltages such that there is a current induced in the solution. Proteins placed into the focusing solution chamber move along the pH gradient by the electric field force acting on the net charge of the protein. Since proteins have an inherent charge to pH relationship, at some point along the pH gradient the proteins acquire a net charge of zero (isoelectric point) and concentrate at that point. This protein migration process occurs regardless of where the protein starts within the chamber. Kolin demonstrated concentrations of proteins as narrow bands in excess of 1 mg/mL. However, one significant drawback of this technique was that the pH gradients formed by simple buffers were difficult to stabilize pH values would drift in position over the time required for focusing.

Immobilized pH Gradients

The problems with pH stability were largely overcome by the introduction of immobilized pH gradient polyacrylamide "gels" [15] and ampholytes. Ampholytes used within a dispersion medium are able to maintain a stationary pH gradation under the influence of an electric field. This stability allowed for isoelectric focusing techniques consistent and accurate enough for commercial applications. The extension of this immobilized gradient technique into a two dimensional process enabled a more efficient method to test two characteristics of proteins simultaneously. O'Farrel [16] demonstrated the — appropriately named— 2D-electrophoresis technique in 1975. Typically, this technique first separates substances on the basis of their charge by isoelectric focusing (IEF) as in the single dimensional case. Then, in the second dimension (movement set perpendicular to first spread), a size separation is performed by sodium dodecyl sulphate polyacrylamide gel electrophoresis (SDS-PAGE). Advancements in matrix assisted laser desorption ionization and time-of-flight mass spectrometry to the mass analysis of peptide digests of protein spots from 2D gel processes allowed for the construction of a peptide mass fingerprint database such that it is now possible to rapidly and accurately

identify proteins for which sequence information is included in the database [17].

1.2.3 Conductivity Gradient Focusing

Conductivity gradient focusing (CGF) can be created within the focusing channel by spatially varying the buffer salt concentration. A simple salt such as NaCl dissociates in the solution and generates Na and Cl ions that serve as charge carriers. By continuously flushing two buffers of different conductivity for the cathode and anode ends of the channel, a diffusion equilibrium, in the form of a conductivity gradient will be created in the space along the nanochannel. Greenlee and Ivory [18] demonstrated that conductivity gradients can also be formed by running two parallel buffer streams in concurrent flow and in contact across a dialysis membrane. This formed a conductivity gradient in each of the streams and electro focusing could be achieved in one of the channels. Another method that utilizes conductivity gradients is field amplified stacking (FAS) [19]. A gradient in electric field is induced due to a difference in conductivity within the channel. Since the current density along the axis of the channel must be uniform, the low conductivity region experiences a higher electric field. Charged particles in the low conductivity (high velocity) region are pushed into the high conductivity (low velocity) region and accumulate near the boundary. Under the influence of the conductivity gradient, analytes with distinct electrophoretic mobilities will experience different electrophoretic velocities along the channel [18]. The opposing actions of electrophoretic and electro-osmotic forces within the channel effectively trap and concentrate the various analyte proteins to discernible equilibrium positions depending on their respective electrophoretic mobilities.

1.2.4 Temperature Gradient Focusing

Ross and Locascio [20] developed a system that created an electrophoretic velocity gradient without the use of semipermeable structures but instead by generating a temperature gradient along the length of the separation channel. In the presence of a counter flowing bulk buffer, there is a unique position where the electrophoretic velocity and bulk counter flow velocity sum to zero. The analytes focus at that point. This technique, termed temperature gradient focusing (TGF), was easier to implement than electric field gradient focusing (EFGF) and it was capable of focusing a wider class of analytes. The main disadvantage of TGF was the fact that in order for this method to operate, a specific buffer with a temperature dependent ionic strength such as tris-borate must be used. Temperature dependent ionic strength buffers were initially

limited in variety. Alternative heating methods were recently developed for TGF. Kim et al. [21] developed a device for TGF with variable width channels that exploited Joule heating to create a temperature gradient.

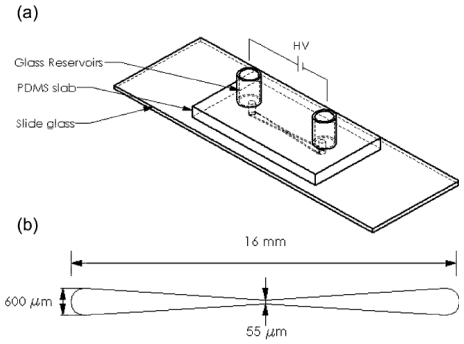

Figure 1.2-1: Temerature gradient due to joule heating effects at the narrowing section of the channel [21]

1.2.5 Current Gradient Focusing

Another method to achieve a focusing effect is to spatially vary the current density while maintaining a constant hydrodynamic counter-flow. Koegler and Ivory [22] have demonstrated charged protein separation and focusing within an electric field gradient using a column packed with size exclusion chromatography (SEC) resin. The chamber was designed such that the coolant that travelled coaxially in the opposite direction of the inner dialysis tube chamber that flowed buffer solution. The coolant chamber was fluted (the cross-sectional area was varied such that it widened along the length of the column) so that the circulating electrolyte (coolant) created a fixed linear gradient in the electric field which drove the proteins against the constant pressure driven flow of the buffer. Electrophoretic velocity of the proteins equals the product of electrophoretic mobility and the electric field. Each analyte slows down as it approaches the location of the column where the analyte electrophoretic velocity and bulk buffer velocity sums to zero. If a mixture of protein analytes is introduced to the system, they would focus in discrete bands with accordance to their specific electrophoretic mobilities. This technique was later termed as an electric field-gradient focusing (EFGF). In a paper by Huang and Ivory [23], an alternative current gradient method was developed through the use of electrode arrays to manipulate the field rather than cross-sectional area variation. Using this method, they were not only able to induce nonlinear gradients, but also tune the field during operation with a high degree of control. The device was

composed of 50 computer controlled electrodes and was shown to separate 40 proteins within 30 minutes. Myers and Bartle [24] later developed a similar device consisting of only five electrodes which could separate up to 6 proteins within 15 minutes.

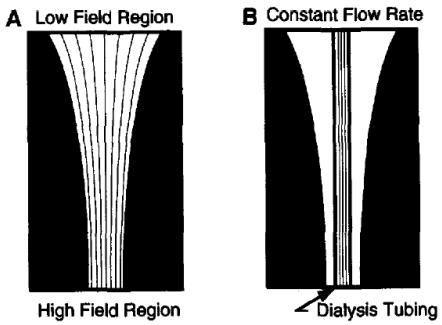

FIGURE 1.2-2: Koegler's design for electric field gradient electrofocusing. [22]

1.3 Progress of Nanofluidic Separations

The gradient methods mentioned earlier depend on dynamic equilibrium between two or more forces in order to form a stable focus. These are the methods of interest for this thesis. However, while some of these methods (such as CACE), can employ some nanoscale physics, they are not exclusive to microfluidic and nanofluidic technology. There are many modes of biomolecular separation that occur at the nanoscale regime through various phenomena which can be categorized as steric [25][26], hydrodynamic [27][28], entropic [29][30][31], electrical [32][33][34], and ratcheting [35][36]. The most often separated biomolecule of interest has been DNA, but recent studies have performed separations on proteins as well, through field effect transport [37], using pH to control protein diffusion [38], and for the purpose of preconcentration [39][8][9]. For the moment, this has been a brief listing of current work in nanofluidic biomolecular separations, but we will elaborate upon some of these techniques in the context of their relevance to our work within the introduction sections of the following chapters.

As an aside, the phenomenon of dielectrophoresis is of interest to us as well since it is a related phenomenon to electrophoresis and can potentially be performed on devices such as ours. First described by Pohl et al. [40], dielectrophoresis does not inherently depend on counteracting electrophoresis or electroosmosis induced by a constant electric field to create a trapping condition, but rather the dielectrophoretic force is isolated from electrophoresis by the application of an alternating polarity voltage

(AC current) at the electrodes which essentially averages out the electrophoretic and electro osmotic contributions to particle motion to zero. The dielectrophoretic force is then free to move the particles and focus them toward locations of either minimum or maximum electric field, depending on their polarizability [41]. While we don't expand on this phenomenon in this thesis, it presents an interesting direction for future work.

1.4 Theory, Simulations and Modelling

In order for dynamic equilibrium separation techniques to advance, there must be a robust theoretical understanding of the physics involved. Several studies focused on modelling and simulations of the various methods of electrofocusing. Tolley et al. [42] have undertaken an exhaustive theoretical description of electric field gradient focusing (EFGF). Warnick et al. [43] contributed and elaborated on the theory. Locke and Carbonell [44] performed both experimental and theoretical studies of CACE. Ghosal and Horek [45] did theoretical work on gradient focusing and generalized TGF theory to include focusing using alternative gradients to temperature gradients. They also incorporated Taylor dispersion [46] to calculate time evolution of a peak as it approaches equilibrium width and location within the focusing channel.

Even the seemingly elementary task of quantifying and predicting the inherent charge on glass surfaces has proven to be elusive in microfluidic channels. Surface charge of glass has a critical effect on the electroosmotic velocity within a glass channel. Since glass has been a standard substrate for microfluidic devices and electrophoretic capillaries, there have been several experimental and theoretical studies on quantifying the charge on glass surfaces. Behrens and Grier [47] presented a method of calculating electric charge density of silica surfaces in contact with aqueous electrolytes in conditions of low specific surface area and low ionic strength solutions. The charge of silica and glass surfaces nearly in contact with a second anionic surface could be calculated from an exact solution of the nonlinear Poisson-Boltzmann equation. It was also shown that the additional presence of van der Waals forces should be taken into account when interpreting interaction experiments since they pose a significant contribution to the forces. Tandon et al. made a thorough report on zeta potential and the electroosmotic mobility in microfluidic devices [48][49], wherein they discussed electrokinetic characterization of hydrophobic polymers and addressed the complexities of determining the origin of charge when modelling electrokinetics of microfluidic devices. The second part of the report addressed issues concerning the impact of hydrodynamic slip and the role of diffuse interfacial structures.

1.4.1 Performance Comparison

As mentioned earlier, the nanofluidic modalities of electrofocusing have certain advantages over the standard capillary electrophoresis (CE) methods. At this point in time, however, biomolecular separations are primarily performed with capillary instruments rather than chip based devices. This is partially due to the fact that the capillary systems are more mature, but also due to the fact that resolution and detection limits are still somewhat higher in capillary systems.

However, over the years, there have been improvements to concentration and accumulation time for nanofluidic device methods, as well as improvements to resolution. One primary advantage of on-chip counter-flow gradient focusing is that it can have much shorter channels than CE. While CE focus bands are limited in that they must manifest while travelling down the limited length of the tube, nanofluidic chip focus peaks can be stationary by design so accumulation time is not limited and their positions may be adjusted by controlling the bulk back flow or voltage. Another major advantage is that counter flow electrofocusing does not necessarily require a specific injection point or timing. The analytes will travel toward the zero velocity position and focus regardless of their initial position or distribution. So it appears we may be on the brink of a shift in what may be considered the "standard" in biomolecular separation in the future.

1.5 Scope

The main goal of this project was to investigate the effectiveness and feasibility of our proposed technique for simultaneous concentration and separation of biomarkers. The combined effects of electrokinetic and electromagnetic phenomena at the nanoscale were observed. The best parameters for focusing were established in order to maximize the concentration and separation resolution of the specific target molecules.

In addition, with our design, we address some of the limitations and challenges that come with the inherently small scale of nanofluidic chips. Since nanofluidics involves a much smaller volume of sample compared to conventional techniques, the molecules of interest within the sample can become too few in number to yield adequate detectability. As mentioned earlier, there are many studies[50][51] dedicated to creating a pre-concentration or a selective depletion condition in order to bring the analyte biomolecule concentrations to reasonable detectability levels before separation and identification can be performed. This, in part, motivates our project, since our

novel technique enables simultaneous concentration and separation of biomarkers without preconcentration or selective depletion phases. Furthermore, it has advantages in having no need for membranes, external pumps, temperature gradients or ampholytes [52].

The remainder of this manuscript will proceed as follows. In chapter 2 we describe the key principles and theory at play in the nanofluidic flow regime. Chapter 3 demonstrates pH gradient protein focusing of R-phycoerythrin and streptavidin within the nanofluidic device. In chapter 4 we investigate the separation and concentration of protein (R-phycoerythrin) and DNA (extracted from Bacillus cereus). Chapter 5 explores how the device may be employed to detect molecular interactions, specifically, a hybridization reaction between DNA and a complementary sequence of peptide-nucleic-acid (PNA).

References

[1] Marcus Joshua and Thorsen Todd. Progress in nanofluidics for cell biology. In *Electrical Engineering Handbook*, pages 26–1–26–27–. CRC Press, 2007. 1

[2] P. Grosso, S. Carrara, C. Stagni, and L. Benini. A low-cost point-of-care system for parallel elisa essays. In *Biomedical Circuits and Systems Conference, 2009. BioCAS 2009. IEEE*, pages 269–272–, 2009. 2

[3] F.S. Collins, M. Morgan, and A. Patrinos. The human genome project: lessons from large-scale biology. *Science*, 300:286–290–, 2003. 2

[4] Valli De Re, Maria Paola Simula, Vincenzo Canzonieri, and Renato Cannizzaro. Proteomic analyses lead to a better understanding of celiac disease: focus on epitope recognition and autoantibodies. *Digestive Diseases and Sciences*, 55(11):3041–3046, 2010. 3

[5] Raanan Shamir, Rami Eliakim, Nitza Lahat, Esther Sobel, and Aaron Lerner. Elisa of anti-endomysial antibodies in the diagnosis of celiac disease: Comparison with immunofluorescence assay of anti-endomysial antibodies and tissue transglutaminase antibodies. *Israel Medical Association Journal*, 7:594–596, 2002. 3

[6] V Thongboonkerd and JB Klein. *Overview of Proteomics*, volume 141. S.Karger, 2004. 3

[7] Kuan-Da Huang and Ruey-Jen Yang. A nanochannel-based concentrator utilizing the concentration polarization effect. *Electrophoresis*, 29(24):4862–4870, 2008. 3

[8] Kathleen C. Kelly, Scott A. Miller, and Aaron T. Timperman. Investigation of zone migration in a current rectifying nanofluidic/microfluidic analyte concentrator. *Analytical Chemistry*, 81(2):732–738, 2009. PMID: 19072034. 3, 8

[9] Ying-Chih Wang, Anna L. Stevens, and Jongyoon Han. Million-fold preconcentration of proteins and peptides by nanofluidic filter. *Analytical Chemistry*, 77(14):4293–4299, 2005. 3, 8

[10] A. Adam and C. Schots. *Biochemical and biological applications of isotachophoresis: proceedings of the first international symposium, Baconfoy, May 4-5, 1979.* Analytical chemistry symposia series. Elsevier Scientific Pub. Co., 1980. 3

[11] C. F. Ivory. A brief review of alternative electrofocusing techniques. *Separation Science and Technology*, 35:1777–1793–, 2000. 4

[12] P.H. O'Farrell. Separation techniques based on the opposition of two counteracting forces to produce a dynamic equilibrium. *Science*, 227(4694):1586–1589, 1985. 4

[13] Cornelius F. Ivory and William A. Gobie. Continuous counteracting chromatographic electrophoresis. *Biotechnology Progress*, 6:21–32, 1990. 5

[14] A. Kolin. Separation and concentration of proteins in a ph field combined with an electric field. *The Journal of Chemical Physics*, 22:1628–1629–, 1954. 5

[15] G. Dale and A. L. Latner. Isoelectric focusing in polyacrylamide gels. *Lancet*, 1:847–848, 1968. 5

[16] P.H. O'Farrell. High resolution two-dimensional electrophoresis of proteins. *Journal of Biological Chemistry*, 250:4007–4021–, 1975. 5

[17] D. J. C. Pappin, P. Hojrup, and A. J. Bleasby. Rapid identification of proteins by peptide-mass fingerprinting. *Current Biology*, 3:327–332–, 1993. 6

[18] Robert D. Greenlee and Cornelius F. Ivory. Protein focusing in a conductivity gradient. *Biotechnology Progress*, 14:300–309–, 1998. 6

[19] Rajiv Bharadwaj and Juan G. Santiago. Dynamics of field-amplified sample stacking. *Journal of Fluid Mechanics*, 543:57–92–, 2005. 6

[20] David Ross and Laurie E. Locascio. Microfluidic temperature gradient focusing. *Analytical chemistry*, 74:2556–2564, 2002. 6

[21] S. M. Kim, G. J. Sommer, M. A. Burns, and E. F. Hasselbrink. Low-power concentration and separation using temperature gradient focusing via joule heating. *Analytical chemistry*, 78:8028–8035–, 2006. xv, 7

[22] Wendy S. Koegler and Cornelius F. Ivory. Focusing proteins in an electric field gradient. *Journal of Chromatography A*, 726:229–236–, 1996. xv, 7, 8

[23] Z. Huang and C. F. Ivory. Digitally controlled electrophoretic focusing. *Analytical chemistry*, 71:1628–1632, 1999. 7

[24] P. Myers and K. D. Bartle. Towards a miniaturised system for dynamic field gradient focused separation of proteins. *Journal of Chromatography A*, 1044:253–258–, 2004. 8

[25] Sumita Pennathur, Fabio Baldessari, Juan G. Santiago, Michael G. Kattah, Jonathan B. Steinman, and Paul J. Utz. Free-solution oligonucleotide separation in nanoscale channels. *Analytical Chemistry*, 79(21):8316–8322, 2007. PMID: 17883279. 8

[26] Joshua David Cross, Elizabeth A. Strychalski, and H. G. Craighead. Size-dependent dna mobility in nanochannels. *Journal of Applied Physics*, 102(2):–, 2007. 8

[27] Lotien Richard Huang, Edward C. Cox, Robert H. Austin, and James C. Sturm. Continuous particle separation through deterministic lateral displacement. *Science*, 304(5673):987–990, 2004. 8

[28] Masumi Yamada, Megumi Nakashima, and Minoru Seki. Pinched flow fractionation: Continuous size separation of particles utilizing a laminar flow profile in a pinched microchannel. *Analytical Chemistry*, 76(18):5465–5471, 2004. PMID: 15362908. 8

[29] J. Han and H. G. Craighead. Entropic trapping and sieving of long dna molecules in a nanofluidic channel. *Journal of Vacuum Science & Technology A*, 17(4):2142–2147, 1999. 8

[30] J. Han, S. W. Turner, and H. G. Craighead. Entropic trapping and escape of long dna molecules at submicron size constriction. *Phys. Rev. Lett.*, 83:1688–1691, Aug 1999. 8

[31] J.T. Mannion, C.H. Reccius, J.D. Cross, and H.G. Craighead. Conformational analysis of single {DNA} molecules undergoing entropically induced motion in nanochannels. *Biophysical Journal*, 90(12):4538 – 4545, 2006. 8

[32] Anthony L. Garcia, Linnea K. Ista, Dimiter N. Petsev, Michael J. O'Brien, Paul Bisong, Andrea A. Mammoli, Steven R. J. Brueck, and Gabriel P. Lopez. Electrokinetic molecular separation in nanoscale fluidic channels. *Lab Chip*, 5:1271–1276, 2005. 8

[33] Tzu-Chi Kuo, Donald M. Cannon, Yanning Chen, Joseph J. Tulock, Mark A. Shannon, Jonathan V. Sweedler, and Paul W. Bohn. Gateable nanofluidic interconnects for multilayered microfluidic separation systems. *Analytical Chemistry*, 75(8):1861–1867, 2003. PMID: 12713044. 8

[34] EA Strychalski, HW Lau, and LA. Archer. Nonequilibrium separation of short dna using nanoslit arrays. *Journal of Applied Physics.*, 106(2), 2009. 8

[35] Richard W. Hammond, Joel S. Bader, Steven A. Henck, Michael W. Deem, Gregory A. McDermott, James M. Bustillo, and Jonathan M. Rothberg. Differential transport of dna by a rectified brownian motion device. *Electrophoresis*, 21(1):74–80, 2000. 8

[36] J.S. Bader, M.W. Deem, R.W. Hammond, S.A. Henck, J.W. Simpson, and J.M. Rothberg. A brownian-ratchet dna pump with applications to single-nucleotide polymorphism genotyping. *Applied Physics A*, 75(2):275–278, 2002. 8

[37] Rohit Karnik, Kenneth Castelino, and Arun Majumdar. Field-effect control of protein transport in a nanofluidic transistor circuit. *Applied Physics Letters*, 88(12):–, 2006. 8

[38] Reto B. Schoch, Arnaud Bertsch, and Philippe Renaud. ph-controlled diffusion of proteins with different pi values across a nanochannel on a chip. *Nano Letters*, 6(3):543–547, 2006. PMID: 16522059. 8

[39] Sun Min Kim, Mark A. Burns, and Ernest F. Hasselbrink. Electrokinetic protein preconcentration using a simple glass/poly(dimethylsiloxane) microfluidic chip. *Analytical Chemistry*, 78(14):4779–4785, 2006. PMID: 16841895. 8

[40] Herbert A. Pohl. The motion and precipitation of suspensoids in divergent electric fields. *Journal of Applied Physics*, 22(7):869–871, 1951. 8

[41] Swagatika Dash and Swati Mohanty. Dielectrophoretic separation of micron and submicron particles: A review. *Electrophoresis*, 35(18):2656–2672, 2014. 9

[42] H. D. Tolley, Q. G. Wang, D. A. LeFebre, and M. L. Lee. Equilibrium gradient methods with nonlinear field intensity gradient: A theoretical approach. *Analytical chemistry*, 74:4456–4463–, 2002. 9

[43] Karl F. Warnick, Scott J. Francom, Paul H. Humble, Ryan T. Kelly, Adam T. Woolley, Milton L. Lee, and H. Dennis Tolley. Field gradient electrophoresis. *Electrophoresis*, 26:405–414–, 2005. 9

[44] B. R. Locke, R. G Carbonell, P.C Wankat, E. Gruska, and Van Oss. *Separation and Purification Methods*, volume 18. Marcel Dekker, New York, 1989. 9

[45] S. Ghosal and J. Horek. Mathematical model describing gradient focusing methods for trace analytes. *Analytical chemistry*, 77:5380–5384–, 2005. 9

[46] Geoffrey Taylor. Dispersion of soluble matter in solvent flowing slowly through a tube. In *Proceedings of the Royal Society of London. Series A. Mathematical and Physical Sciences*, volume 219, pages 186–203–, 1953. 9

[47] Sven H. Behrens and David G. Grier. The charge of glass and silica surfaces. *The Journal of Chemical Physics*, 115:6716–6721–, 2001. 9

[48] Vishal Tandon, Sharath K. Bhagavatula, Wyatt C. Nelson, and Brian J. Kirby. Zeta potential and electroosmotic mobility in microfluidic devices fabricated from hydrophobic polymers: 1. the origins of charge. *Electrophoresis*, 29:1092–1101–, 2008. 9

[49] Vishal Tandon and Brian J. Kirby. Zeta potential and electroosmotic mobility in microfluidic devices fabricated from hydrophobic polymers: 2. slip and interfacial water structure. *Electrophoresis*, 29:1102–1114–, 2008. 9

[50] Pudun Zhang, Guowang Xu, Jianhui Xiong, Yufang Zheng, Xianzhe Shi, Qing Yang, and Fusheng Wei. Enhancing the sensitivity of capillary electrophoresis using a microcolumn solid phase extraction setup. *Journal of Separation Science*, 26:1527–1532–, 2003. 10

[51] Jozef L. Beckers and Petr Bocek. Sample stacking in capillary zone electrophoresis: Principles, advantages and limitations. *Electrophoresis*, 21:2747–2767, 2000. 10

[52] David W. Inglis, Ewa M. Goldys, and Nils P. Calander. Simultaneous concentration and separation of proteins in a nanochannel. *Angewandte Chemie International Edition*, 50(33):7546–7550, 2011. 11

2

Basic Principles and Theory

The following is a discussion of the relevant theoretical concepts that lay the foundation of this experimental thesis project. This section not comprehensive, but rather a distillation of the key concepts applicable to this thesis. Specifically, we examine the physics that apply to microfluidics and nanofluidics, addressing the implications of the decreasing size of device geometries and investigating unique phenomena occurring in liquids confined at the nanoscale. Those who are interested in a more in-depth treatment of the concepts are referred to textbooks on the subject by Hsueh-Chia Chang [1], Probstein [2], and others [3][4].

2.1 Flow Approximations

Throughout this text, we consider fluid to be of a single continuum phase that is continuously and indefinitely divisible. In this way, all macroscopic physical, chemical and thermodynamic quantities are uniformly distributed over any infinitesimal volume. This continuum approximation treatment enables us to attach a value to a quantity at a point, which is mathematically useful. However, the continuum approximation disregards the molecular nature of the fluid and may require additional techniques to account for these interactions.

Although the general forms of equations will be provided where possible, the fluids dealt with here are typically approximated as "incompressible" liquids since changes in pressure do not result in appreciable changes in liquid density as would be the case with compressible gas flow. It should be noted that, although "incompressible" is often used to describe constant density, at low-speeds, gaseous flow may be regarded as constant density despite being highly compressible. Similarly, an electrolytic solution under a centrifugal force develops a strong density gradient. Despite the solution being incompressible, in such a case, it cannot be considered constant density. In reality, one must consider the fluid's ability to experience shear stresses, i.e., a real fluid is viscous. These viscous behaviours are more generally described as "transport effects" and can include diffusion of mass, heat, and charge.

Viscous flow can be compartmentalized into regimes of laminar and turbulent flows. Our focus will be on *laminar flow*, where the fluid moves predictably, as if it is layered, with each layer moving with different velocity. *Turbulent flow*, on the other hand, exhibits unpredictable, chaotic behaviour. When convection is forced, motion will be either laminar or turbulent, depending on the size of the Reynolds number compared with the "critical value". This will be addressed later in section 2.4 of this chapter. Turbulence presents a problem because it increases rates of transfer and mixing beyond rates typically expected from molecular diffusion and a thorough, fundamental understanding for turbulent flow is not yet established to this day.

Micro and nanofluidics often deals with suspensions of small particles which can include molecules, colloids, and cells. The shapes of these particles are often complex, nonrigid, and may change configuration under static and dynamic conditions within different environments 2.1-1. Given these varieties, it becomes a challenge to model the interactions of these particles within fluid systems. In our treatments, we consider the particles to be regular geometric shapes, i.e., spheres – the most commonly used model. However, there are other treatments which consider the particles as oblate and prolate spheroids, rods, and disks [5].

Biological macromolecules such as proteins, composed of amino acid residues joined consecutively by peptide bonds, and DNA (Deoxyribonucleic acid), composed of nucleobases connected by a sugar-phosphate backbone can be described as spherical without much consequence to the analytical rigour of the treatment of fluid flow. Furthermore, synthetic polymers dispersed in suspension, like polystyrene latex have been viewed to be very nearly spherical. Clay and crystalline material are often plate-like and can be modelled as thin disks. Fibrous collagen and certain viruses can be regarded as

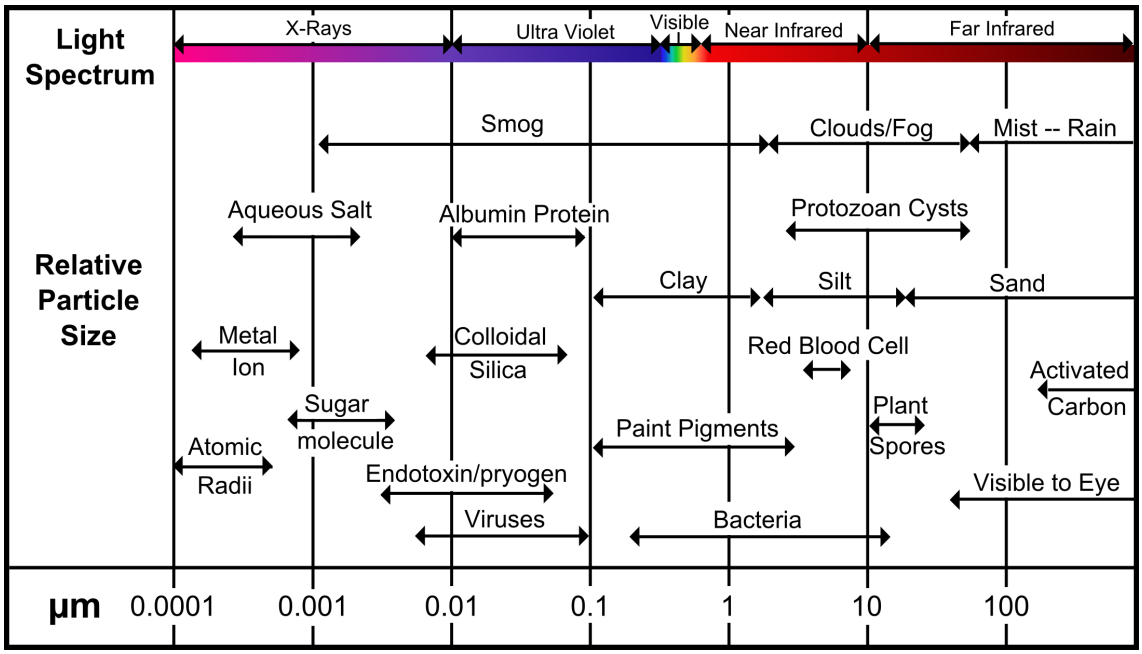

FIGURE 2.1-1: Some particles and their relative sizes.

cylindrical rods.

The particle suspensions considered here are generally assumed to be monodisperse – all particles in the system are considered to be the same. Real particle suspension solutions are considered polydisperse – composed of particles with a distribution of size and shape characteristics.

2.2 Transport in Fluids

2.2.1 Continuum Hydrodynamics

In order to understand the fundamental concepts of electrokinetics - the motion of fluid induced by electric fields - we must understand how the electrostatic theories couple with the hydrodynamic models which describe fluid motion.

For our purposes, it is important to make the assumption that the fluid behaves in a "continuum" regime. At a microscopic scale, fluid is comprised of individual molecules so the physical properties of each molecule at any given time - such as size, mass and velocity - are drastically non-uniform. However, hydrodynamics are studied at the macroscopic scale so we do not consider molecular details. This is what is referred to as "continuum" fluid. The observable behaviour of the fluid is viewed at a coarse enough

scale that even a small fluid element contains a huge number of molecules. In this way, we can assign a bulk flow velocity $\mathbf{u}(x, y, z, t)$ to a fluid element at point, x, y, z, at a time, t, by averaging over the many fluctuating Brownian molecular velocities. Other values such as density, $\rho(x, y, z, t)$, etc can also be locally averaged and then their value will vary smoothly with position x, y, z. These assumptions directly lead to the partial differential form of the fundamental equations of hydrodynamics.

Assuming that the flows occurring within microchannels are within the continuum regime as discussed previously, the motion of the fluid with a density ρ will be governed by several conservation equations which can be derived from the Reynolds transport theorem (equation 2.1) [6][7].

$$\frac{d}{dt}\int_{\Omega} L dV = -\int_{\partial\Omega} L\mathbf{u}\cdot\mathbf{n}dA - \int_{\Omega} Q dV \tag{2.1}$$

where, L represents any intensive property (a physical property that does not depend on the system size or the amount of material in the system) defined over a volume Ω. The Reynolds transport equation states that the sum of changes of L within the system over time must equal to the loss or gain of that property through the boundaries of the volume (represented by the $\int_{\partial\Omega} L\mathbf{u}\cdot\mathbf{n}dA$ term) and what is created or consumed by sources or sinks within the volume (represented by the term $\int_{\Omega} QdV$). Equation 2.1 can be simplified by applying the *divergence theorem* and Leibniz's Rule to arrive at the simplified equation 2.2.

$$\frac{dL}{dt} + \nabla\cdot(L\mathbf{u}) + Q = 0 \tag{2.2}$$

This theorem can be used to arrive at conservation equations and other intensive relationships.

Material Derivative

It is necessary to understand the concept of the *material derivative* before moving on to deal with equations of motion and the conservation equations. A standard time derivative $\frac{d}{dt}$ is the rate of change of an intensive property at a stationary point, however, the material derivative $\frac{D}{Dt}$ is the rate of change of an intensive property while, at the same time, accounting for the particle velocity (or volume element velocity).

$$\frac{D}{Dt} = \frac{\partial}{\partial t} + u_i\frac{\partial}{\partial x_i} \tag{2.3}$$

where the reference frame velocity is defined as u_i. The material derivative is useful in arriving at somewhat more compact equations so we shall evoke it in later sections.

Conservation of Mass

We can see simply how mass conservation takes the form of Reynold's transport equation by considering a volume V bounded by surface S fixed in space. The decrease of mass inside the volume is given in the form of "rate decrease" of mass density ρ in an infinitesimal volume.

$$\text{mass decrease} = -\frac{d}{dt}\int_V \rho dV = -\int_V \frac{\partial \rho}{\partial t} dV \tag{2.4}$$

We also consider the movement of mass out of the volume V by observing that the rate of outward mass flux across any small surface area element dS of S is $\rho\mathbf{u} \cdot d\mathbf{S}$, where $d\mathbf{S}$ represents the element's infinitesimal surface area orthogonal to unit vector $\hat{n}$. The flux is integrated over the element outward normal vectors.

$$\text{Mass flux out} = \int_S \rho\mathbf{u} \cdot d\mathbf{S} = \int_V \nabla \cdot (\rho\mathbf{u}) dV \tag{2.5}$$

Figure 2.2-2 illustrates how the surface integral in equation 2.5 converts into the volume integral: the sum of components entering and leaving the element can be represented by the divergence of the infinitesimal volume.

$$\nabla \cdot (\rho\mathbf{u}) = \frac{\partial \rho u_x}{\partial x} + \frac{\partial \rho u_y}{\partial y} + \frac{\partial \rho u_z}{\partial z} \tag{2.6}$$

where u_x, u_y, u_z represent the velocity components in each direction. For mass to be conserved everywhere, the right sides of equations 2.4 and 2.5 must be equal for any volume V.

$$\int_V \frac{\partial \rho}{\partial t} dV = -\int_V \nabla \cdot (\rho\mathbf{u}) dV \tag{2.7}$$

$$\int_V \left\{ \frac{\partial \rho}{\partial t} + \nabla \cdot (\rho\mathbf{u}) \right\} dV = 0 \tag{2.8}$$

or in differential form

$$\frac{\partial \rho}{\partial t} + \nabla \cdot (\rho\mathbf{u}) = 0 \tag{2.9}$$

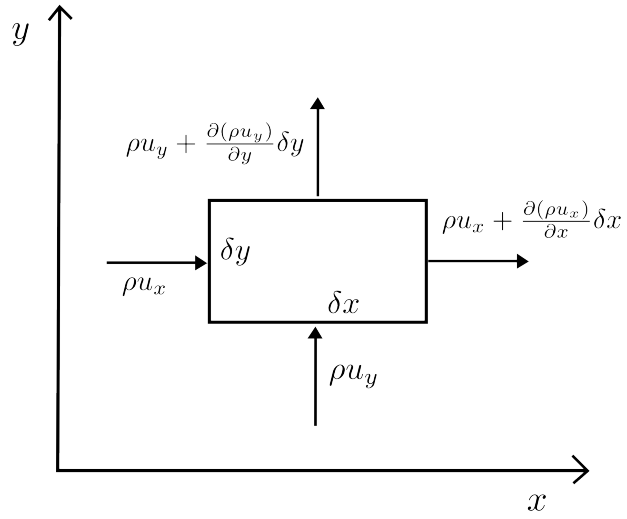

FIGURE 2.2-2: The mass flux entering and leaving an element viewed in a simplified 2D case.

by applying the product rule, we can write:

$$\frac{\partial \rho}{\partial t} + \rho \nabla \cdot \mathbf{u} + (\mathbf{u} \cdot \nabla)\rho = 0 \tag{2.10}$$

which is also often written using the material derivative, D/Dt

$$\frac{D\rho}{Dt} + \rho \nabla \cdot \mathbf{u} = 0 \tag{2.11}$$

Under the special condition where ρ is constant ($D\rho/Dt = 0$), we arrive at the continuity equation for incompressible flow:

$$\nabla \cdot \mathbf{u} = 0 \tag{2.12}$$

Conservation of Momentum

Similarly to the above approach, it is possible to interpret the conservation of momentum from a hydrodynamics perspective. But it is simpler to approach it from Newton's second law:

$$\mathbf{F} = m\mathbf{a} \tag{2.13}$$

Since we are operating with a fixed control volume and infinitesimal fluid parcels, we can substitute density for mass. We will also replace $\mathbf{b} = \mathbf{F}$ to represent the total

body forces.

$$\mathbf{b} = \rho \frac{d}{dt}\mathbf{u}(x, y, z, t) \tag{2.14}$$

expanding by chain rule

$$\mathbf{b} = \rho \left(\frac{\partial \mathbf{u}}{\partial t} + \frac{\partial \mathbf{u}}{\partial x}\frac{\partial x}{\partial t} + \frac{\partial \mathbf{u}}{\partial y}\frac{\partial y}{\partial t} + \frac{\partial \mathbf{u}}{\partial z}\frac{\partial z}{\partial t} \right) \tag{2.15}$$

simplifying to a more compact form, we can write

$$\mathbf{b} = \rho \left(\frac{\partial \mathbf{u}}{\partial t} + \mathbf{u} \cdot \nabla \mathbf{u} \right) \tag{2.16}$$

applying the material derivative described in equation 2.3 we get:

$$\rho \frac{D\mathbf{u}}{Dt} = \mathbf{b} \tag{2.17}$$

which is the conservation of momentum equation in it's simplest form.

2.2.2 Constitutive Equations

The principle of momentum conservation, energy conservation, mass conservation and charge conservation quantitatively describe the states of fluid systems. However, these relations alone are insufficient to uniquely define the the behaviour of the system. Relations involving the material behaviour are also required. Examples of relations that describe material behaviour would be: Newton's law of stress proportionality to rate of strain, Fourier's law of heat transfer rate proportionality to temperature and Fick's Law of mass transfer proportionality to concentration gradient. These are called constitutive equations and they may be defined through material coefficients such as viscosity, heat conduction, etc, which are determined directly from molecular dynamics. However, often times, the coefficients are determined empirically through the phenomena themselves as observed in experiments while the molecular description merely provides the basis for the interpretation of the data. For this reason, the continuum model and it's concepts are considered a "phenomenological description". The constitutive equations describe the manner in which fluxes depend upon spatial gradients. In the following sections, we shall describe momentum flux (related to velocity gradient by fluid viscosity), heat flux (related to temperature gradient by fluid thermal conductivity), mass flux (related to concentration gradient by the fluid diffusivity), and current density (related to to electrostatic potential gradient by the

specific conductivity. Most of these fluxes are vector quantities and are analogous except momentum flux/stress, which is a second order tensor and must be treated somewhat differently.

2.2.3 Viscosity, Shear Stresses and Momentum Transport

Newton's law of viscosity states that in a Newtonian fluid, there is a linear relation between the shear stresses and rates of strain. The Figure 2.2-3 illustrates an infinitesimal fluid element within a flow $u(y)$ in the $+x$ direction with u increasing linearly as y increases. Pressure p is applied on both sides of the element equally. A shear stress can be defined as an exerted force at the edges of the element in the x direction on the top and bottom surfaces. Consider the convention that the positive y face of the shear to is pointing in the positive x direction, the negative y face shear is pointing in the negative x direction. Shear stress can be defined as the force applied per unit area so the balanced forces in Figure 2.2-3 is:

$$\Sigma F_x = \left(\frac{\partial \tau_{yx}}{\partial y}\right) \Delta y \Delta x \tag{2.18}$$

Under a steady flow condition, time change is zero ($\partial/\partial t = 0$) and there are no velocity components in the y direction so

$$\frac{\Sigma F_x}{\Delta y \Delta x} = \left(\frac{\partial \tau_{yx}}{\partial y}\right) = 0 \tag{2.19}$$

or, in other words, τ_{yx} = constant. In this case there is only a single strain rate component, du/dy and a single stress component, τ_{yx}. As mentioned earlier, the Newton formulation assumes that shear stress is a linear relation to the strain rate so the Newtonian viscosity Law can be written as simply:

$$\tau_{yx} = \mu \frac{du}{dy} \tag{2.20}$$

where μ is the viscosity coefficient, which is generally a function of temperature and pressure, but it is often possible to approximate it as only a function of temperature. Another value commonly used is the "kinematic viscosity", $\nu = \mu/\rho$. Considering the effect of one infinitesimal element on another, it can be envisioned that one element imparts some of its momentum to the adjacent element of fluid, causing it to to move in the x direction. τ_{yx} may be interpreted as the viscous flux of x momentum into the

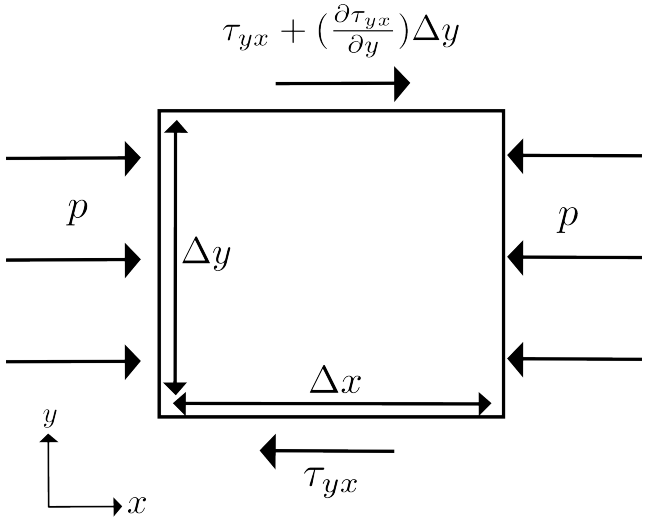

Figure 2.2-3: Shear stress on an infinitesimal element within a horizontal flow.

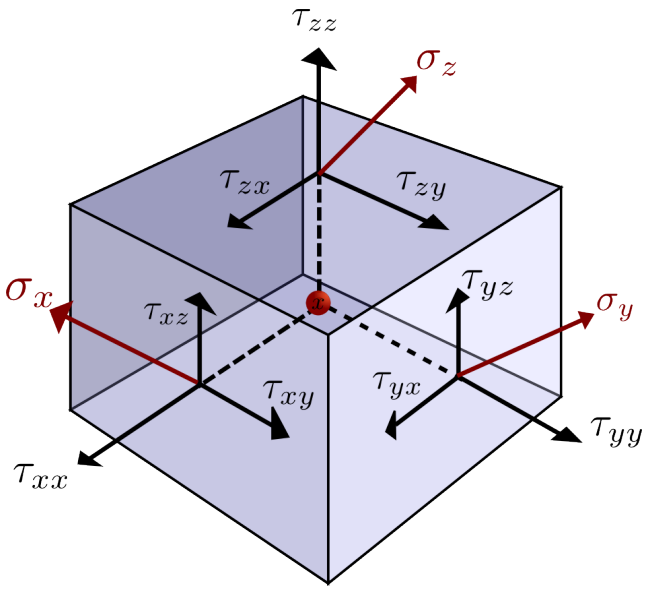

Figure 2.2-4: Cartesian components of the reference stresses (σ_i) and stress tensor components (τ_{ij}) with respect to a point x in a fluid. The cube volume represents an infinitesimal element.

y direction.

Generalized to three dimensions, the Newtonian viscosity takes the form of a tensor which can then be parsed into stresses upon a 3 virtual orthogonal surfaces representing each of the 3 dimensions, x, y, and z as shown in Figure 2.2-4. Each of the reference stress vectors (σ_x, σ_y, σ_z) may be written in components (Appendix A.9 compact Cartesian form):

$$\begin{aligned} \sigma_x &= \tau_{xx}n_x + \tau_{yx}n_y + \tau_{zx}n_z \\ \sigma_y &= \tau_{xy}n_x + \tau_{yy}n_y + \tau_{zy}n_z \\ \sigma_z &= \tau_{zx}n_x + \tau_{yz}n_y + \tau_{zz}n_z \end{aligned} \tag{2.21}$$

The first subscript of τ indicates the axis to which the σ vector is perpendicular and the second subscript indicates to which direction the shear stress is parallel. A Cartesian tensor notation may be written in the form of $\sigma_i = \tau_{ji}n_j$ to describe the nine reference stress tensor components. The stress tensor allows us to completely describe the state of stress in a continuum fluid that may depend on position and time, but is not dependent on the orientation of the surface.

For the 3 dimensional stress tensor case we make the following assumptions about a Newtonian fluid.

1. The fluid is isotropic, i.e., having properties independent of direction.

2. In static or inviscid fluid, the stress tensor must reduce to hydrostatic pressure condition.

$$\tau_{ij} = -p\delta_{ij} \quad \text{where } \delta_{ij} = \begin{cases} 1, & \text{if } i = j \\ 0, & \text{if } i \neq j \end{cases} \tag{2.22}$$

3. The stress tensor τ_{ij} can be at most a linear function of the rate of strain tensor ε_{ij}

$$\varepsilon_{ij} = \frac{1}{2}\left(\frac{\partial u_i}{\partial x_j} + \frac{\partial u_j}{\partial x_i}\right) \tag{2.23}$$

For a general case it can be shown (Batchelor's treatment)[8] that the stress tensor of a Newtonian fluid becomes:

$$\tau_{ij} = -\rho\delta_{ij} + 2\mu(\epsilon_{ij} - \frac{1}{3}\epsilon_{kk}\delta_{ij}) \tag{2.24}$$

$$\text{where} \qquad \epsilon_{kk} = \frac{\partial u_k}{\partial x_k} = \nabla \cdot \mathbf{u} \tag{2.25}$$

For constant density flows where $\nabla \cdot \mathbf{u} = 0$ (when the fluid is considered incompressible), the stress tensor simplifies significantly. Assuming the Cartesian components to be x, y, z, coordinates with u_x, u_y, u_z velocity components, the stress tensor components become:

$$\begin{aligned}
\tau_{xx} &= -p + 2\mu \frac{\partial u_x}{\partial x} \\
\tau_{yy} &= -p + 2\mu \frac{\partial u_y}{\partial y} \\
\tau_{zz} &= -p + 2\mu \frac{\partial u_z}{\partial z} \\
\tau_{xy} = \tau_{yx} &= \mu \left(\frac{\partial u_x}{\partial y} + \frac{\partial u_y}{\partial x} \right) \\
\tau_{xz} = \tau_{zx} &= \mu \left(\frac{\partial u_x}{\partial z} + \frac{\partial u_z}{\partial x} \right) \\
\tau_{yz} = \tau_{zy} &= \mu \left(\frac{\partial u_y}{\partial z} + \frac{\partial u_z}{\partial y} \right)
\end{aligned} \tag{2.26}$$

In expanded format convention, we can further express the stress tensor σ in two terms: the volumetric stress tensor, which has a tendency to change the volume of the body, and the stress deviator tensor, which has a tendency to deform the body. The volumetric stress tensor represents the force which sets the volume of the body (typically pressure). The stress deviator represents the forces which determine the body deformation, composed of the shear stresses on the body.

$$\sigma = -\underbrace{\begin{pmatrix} p & 0 & 0 \\ 0 & p & 0 \\ 0 & 0 & p \end{pmatrix}}_{\substack{\text{volumetric} \\ \text{stress tensor}}} + \underbrace{\begin{pmatrix} \tau_{xx} + p & \tau_{xy} & \tau_{xz} \\ \tau_{yx} & \tau_{yy} + p & \tau_{yz} \\ \tau_{zx} & \tau_{zy} & \tau_{zz} + p \end{pmatrix}}_{\text{stress deviator tensor, } \mathbf{T}} \tag{2.27}$$

If $\nabla \cdot \mathbf{u} = 0$, we can insert the values for τ from equation 2.26.

$$\sigma = -\begin{pmatrix} p & 0 & 0 \\ 0 & p & 0 \\ 0 & 0 & p \end{pmatrix} + \mu \begin{pmatrix} 2\frac{\partial u_x}{\partial x} & \frac{\partial u_x}{\partial y} + \frac{\partial u_y}{\partial x} & \frac{\partial u_x}{\partial z} + \frac{\partial u_z}{\partial x} \\ \frac{\partial u_y}{\partial x} + \frac{\partial u_x}{\partial y} & 2\frac{\partial u_y}{\partial y} & \frac{\partial u_y}{\partial z} + \frac{\partial u_z}{\partial y} \\ \frac{\partial u_z}{\partial x} + \frac{\partial u_x}{\partial z} & \frac{\partial u_z}{\partial y} + \frac{\partial u_y}{\partial z} & 2\frac{\partial u_z}{\partial z} \end{pmatrix} \tag{2.28}$$

Denoting the volumetric stress tensor as pI, where I is the identity matrix, and the deviator tensor as $\mathbf{T}$, we arrive at a compact form.

$$\sigma = -pI + \mathbf{T} \tag{2.29}$$

2.2.4 Navier-Stokes Equation

To arrive at a balanced equation of forces due to the stresses and strains on an infinitesimal volume, we again consider a volume V bounded by a surface S that moves with the flow, always containing the same "material" components. The momentum total will be $\int_V dV \rho \mathbf{u}$ and the rate of change of that momentum is $\int_V dV \rho \frac{d\mathbf{u}}{dt}$ (mass ρdV of each element is constant). This change of momentum must be equal to the net forces acting upon the element. There are two such forces:

- Long ranged external **body forces** – Forces that penetrate matter and act equally on all material in any element dV. (this force is usually gravity, so we define it as $\rho \mathbf{g} dV$ where g is the gravitational acceleration)
- Short ranged molecular **surface forces** – Internal forces within the fluid that arise from interactions at the thin surface layers of adjacent elements. Recall, in the 3D case there are 3 sets of surface planes bounding any element. Each of the 3 planes experiences a 3-component force resulting in 9 components in all, which are described as a tensor σ. The tensor is defined as the force exerted per unit area ($\sigma \cdot \hat{\mathbf{n}}$) across a surface element $\mathbf{dS} \equiv S\hat{\mathbf{n}}$. The total force is the sum of body and surface forces.

$$\text{total force} = \int_V \mathbf{b} dV = \underbrace{\int_V dV \rho g}_{\text{body forces}} + \underbrace{\int_S \sigma \cdot d\mathbf{S}}_{\text{surface forces}} = \int_V dV (\rho g + \nabla \cdot \sigma) \tag{2.30}$$

$$\mathbf{b} = \nabla \cdot \sigma + \rho g \tag{2.31}$$

Applying this $\mathbf{b}$ (total force) to the conservation of momentum equation 2.17, we arrive at:

$$\rho \frac{D\mathbf{u}}{Dt} = \nabla \cdot \sigma + \rho g \tag{2.32}$$

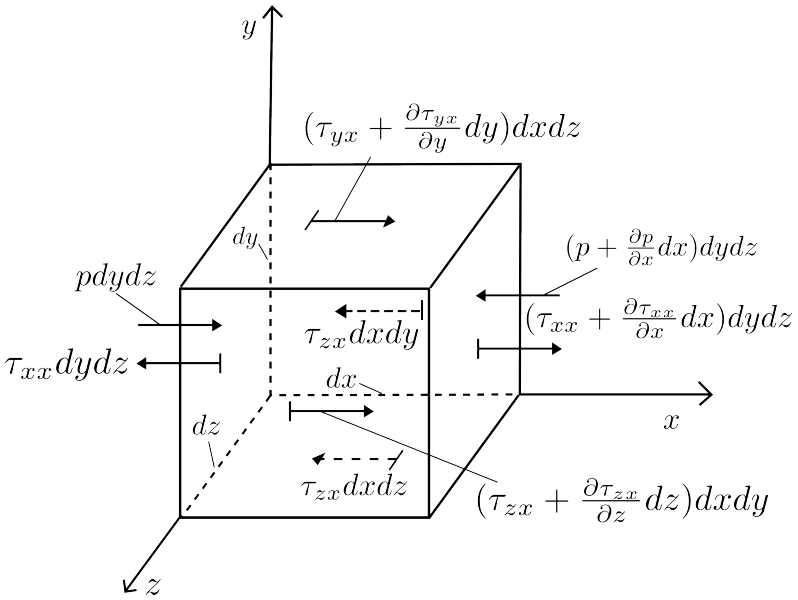

FIGURE 2.2-5: The shear and stretch forces on an infinitesimal moving fluid element. Only the x direction forces are shown.

To visualize how these forces act upon an infinitesimal volume element we can focus on just the x component forces as shown in Figure 2.2-5. Adding up all the surface force components for x, y, z planes, it is possible to see that they can be expressed as the divergence of the stress tensor $\nabla \cdot \sigma$.

From equation 2.29, we plug in σ and we arrive at the general form of the Navier-Stokes equation

$$\rho \frac{D\mathbf{u}}{Dt} = -\nabla p + \nabla \cdot \mathbf{T} + \rho g \tag{2.33}$$

In Cartesian notation, using the general values for τ from equation 2.24, we can also write the general Navier-Stokes equation as

$$\rho \frac{Du_i}{Dt} = -\frac{\partial p}{\partial x_i} + \frac{\partial}{\partial x_j}\left\{\left(\frac{\partial u_i}{\partial x_j} + \frac{\partial u_j}{\partial x_i} - \frac{2}{3}\delta_{ij}\frac{\partial u_k}{\partial x_k}\right)\right\} + \rho g_i \tag{2.34}$$

2.2.5 Explanation of Navier-Stokes Equation

The Navier-Stokes equation (2.33) makes intuitive sense if one is to examine each of its component terms.

- $\rho \frac{D\mathbf{u}}{DT}$: The force each fluid element experiences.

- $-\nabla p$: The pressure term (*volumetric stress tensor*) which prevents stresses due to counteracting normal stresses. Internal fluid pressure prevents the volume from shrinking upon itself.

- $\nabla \cdot \mathbf{T}$: The stress term (*stress deviator tensor*) which causes motion due to horizontal friction and shear stresses. Shear stress can cause viscous flow and turbulence. Nearby elements are "dragged" along by these viscous forces.

- ρg : The force experienced by every fluid element (gravity). It can be simply defined as f_{body} if there is another source of body forces.

If the viscosity μ is constant, and the flow is incompressible, the divergence of the deviator stress tensor seen in equation 2.33 is often expressed as a vector Laplacian. It is easiest to see this using the compact Cartesian form for τ values shown in equation 2.24.

$$\nabla \cdot \mathbf{T} = \mu \frac{\partial}{\partial x_j}\left(\frac{\partial u_i}{\partial x_j} + \frac{\partial u_j}{\partial x_i}\right) = \mu \frac{\partial^2 u_i}{\partial x_j^2} + \mu \frac{\partial}{\partial x_i}\underbrace{\left(\frac{\partial u_j}{\partial x_j}\right)}_{=0} \tag{2.35}$$

$$\nabla \cdot \mathbf{T} = \mu \nabla^2 \mathbf{u} \tag{2.36}$$

The right most term of equation 2.35 is cancelled because of incompressibility ($\nabla \cdot \mathbf{u} = 0$) so the Navier-Stokes equation reduces to:

$$\rho \frac{D\mathbf{u}}{Dt} = -\nabla p + \mu \nabla^2 \mathbf{u} + \rho g \tag{2.37}$$

Navier-Stokes Approximation Criteria

In order to apply the Stokes flow to model liquid transport in nanochannels, it is important to examine the assumptions made for deriving the full Navier-Stokes equations for in-compressible flow and to ensure they are valid. Recall these assumptions are as follows:

1. The fluid is a continuum

2. The viscosity is independent of the shear rate (Newtonian fluid)

3. The fluid is incompressible (time independent density $\rho \neq \rho(t)$)

In the case of gaseous systems, the continuum condition can be checked by use of the Knudsen number (K_n) [9]. which is simply defined as the ratio of the mean free path (λ_{mfp}) of a molecule and the system length L (sometimes, for fluid applications, referred to as the hydraulic diameter)

$$K_n = \frac{\lambda_{mfp}}{L} \tag{2.38}$$

However, in liquid state, molecules are too densely packed for the mean-free-path to be a meaningful quantity. Therefore λ_{mfp} is instead defined as the "interaction length" which is an estimation based on the number of molecules with which the target molecule interacts. K_n can be used as a measure of the deviation from the state of material continuum as follows:

continuum	$K_n < 0.01$
slip flow	$0.01 < K_n < 0.1$
transition region	$0.1 < K_n < 10$
molecular flow	$10 < K_n$

The continuum condition ($K_n < 0.01$) typically applies to flow within larger channels with an interaction length of approximately 3 nm. K_n values between 0.1 and 10 occur at the transition between continuum and free molecule flow. Slip flow will be addressed later in this chapter.

The second assumption applied to the Navier-Stokes equations is the condition that viscosity is independent of the shear rate. A Newtonian fluid experiences viscous stress arising from its flow that is linearly proportional to the strain rate at any point. In other words, a fluid is Newtonian if the tensors that describe the viscous stress and strain rate are related by a constant viscosity tensor that does not depend on the stress state and velocity of the flow. According to the molecular dynamic work by Loose and Hess [10], liquids act Newtonian if they have strain rates up to twice the molecular frequency, $(1/\tau_{freq})$.

$$\tau = \frac{\partial u}{\partial y} \leq \frac{2}{\tau_{freq}} \tag{2.39}$$

$$\text{where} \qquad \tau_{freq} = \sqrt{\frac{m l_{mol}}{N_A k T}} \tag{2.40}$$

τ represents the shear rate as defined before, τ_{freq} is the molecular frequency, l_{mol} [m] is the molecular length scale , m is the molecular mass [kg mol^{-1}], N_A is Avogadro's

number, k is Boltzmann's constant, and T [K] is the temperature. At reasonable nanofluidic channel geometries and flow rates, this requirement is usually satisfied. However, Qiao and Aluru [11], found in simulation that channels with perpendicular dimensions less than 1.5 nm resulted in a breakdown of the Newtonian assumption and shear rates became higher than can be expected under realistic conditions.

The requirement of incompressibility must also be assessed. The compressibility of water is approximately 1% per 20 MPa [12]. This is relatively small and will only have an appreciable effect at high pressures ($>$ 10 MPa). Most microfluidic applications do not exceed such pressures.

Under typical conditions, in nanofluidic channels with at least 10 nm perpendicular dimensions, Stokes flow can be reasonably applied.

2.2.6 Diffusivity and Mass Transport

Diffusion of mass is a transport of mass whenever there is a spatial gradient in the proportions of the mixture, i.e., a concentration gradient. This is analogous to heat transfer and momentum transfer. In a solution, there are typically two ways to define concentration, mass concentration and molar concentration.

Recall that the standard "moles" [mol] unit provides a convenient and more manageable measure of a quantity of molecules (1 mol = 6.0221415×10^{22} molecules). The mass of a molecule depends on its molecular composition. So in order to determine the mass, "molar mass" (M [kg/kmol]) can be determined from the sum of the atomic numbers of the constituent atoms composing the molecule, e.g., water H_2O contains one oxygen (atomic number 16) and 2 hydrogen atoms (atomic number 1) so $16 + (1 + 1) = 18$ kg/kmol. Now mass $m = nM$ where n represents the number of moles, and m is the mass, as usual.

Table 2.1 shows the most common definitions of concentration. i indices represents individual species of a multicomponent fluid. Fluid velocity is often characterized as

TABLE 2.1: Conventions of Concentration

mass concentration	$\rho_i = \frac{m_i}{V}$	$\frac{\text{mass of species } i}{\text{volume of solution}}$	(kg m^{-3})
molar concentration	$c_i = \frac{n_i}{V}$	$\frac{\text{\# of moles of species } i}{\text{volume of solution}}$	(mol m^{-3})
mass fraction	$\omega_i = \frac{\rho_i}{\rho}$	$\frac{\text{mass conc. of species } i}{\text{mass density of solution}}$	-
molar fraction	$x_i = \frac{c_i}{c}$	$\frac{\text{molar conc. of species } i}{\text{molar density of solution}}$	-

an average "bulk" motion. For a multicomponent system, mass average velocity is

$$\mathbf{u} = \frac{1}{\rho}\Sigma\rho_i\mathbf{u}_i \tag{2.41}$$

The mass flux, $\mathbf{j}_i$ is defined as quantity $\rho_i\mathbf{u}_i$ flowing through a unit area normal to the $\mathbf{u}$ mass velocity vector with respect to a fixed coordinate reference frame. Typically the mass average flux for each species is taken in reference to the average bulk mass flow.

$$\mathbf{J}_i = \rho_i(\mathbf{u}_i - \mathbf{u}) \tag{2.42}$$

where the quantity $\rho_i\mathbf{u}$ represents the bulk convective fluxes. Within a spatial concentration gradient, Fick's first law of diffusion states that there is a linear relation between the species flux and the concentration gradient. For instance, in a two species system:

$$\mathbf{J}_1 = \mathbf{j}_1 - \rho_1\mathbf{u} = -\rho D_{12}\nabla\omega_1 \tag{2.43}$$

$D_{12} = D_{21}$ is the mass diffusion coefficient (mass diffusivity) within the binary system. In the case of liquids, ρ is constant so it can be cancelled out of equation 2.42 recalling from table 2.1 that the mass fraction ω contains bulk density of the fluid. Fick's law can be generalized to more species so long as the system contains sufficiently dilute solutions that the species are unaffected by the presence of one another

$$\mathbf{J}_i = \mathbf{j}_i - \rho_i\mathbf{u} = -D_i\nabla\rho_i \tag{2.44}$$

By the same process, this can also be expressed in terms of molar concentration (c_i) instead of mass concentration ρ_i.

$$\mathbf{J}_i^* = \mathbf{j}_i^* - c_i\mathbf{u}^* = -D_i\nabla c_i \tag{2.45}$$

where $\mathbf{u}^*$ is the molar average velocity instead of the mass average velocity. These last equations describe Fick's First law.

2.2.7 Ionic and Molecular Transport

The electric field $\mathbf{E}$ is the negative gradient of electrostatic potential:

$$\mathbf{E} = -\nabla\phi \tag{2.46}$$

Recall the force on a point charge (q) induced by an electric field is $q\mathbf{E}$. This relationship can also be expressed as force per mole of charge carrier.

$$\text{Force per mole} \quad = -z_i N_A e \nabla\phi = -z_i F_c \nabla\phi \tag{2.47}$$

where z_i is the charge number of species i, $e = 1.602 \times 10^{-19}$ coulombs is the elementary charge, and $N_A = 6.022 \times 10^{23}$ is Avogadro's number, $F_c = N_A e$ is Faraday's constant. The molar flux of the ith species, j_i^*, is

$$\begin{aligned} j_i^* &= -\upsilon_i z_i F_c c_i \nabla\phi \\ &= -\upsilon_i z_i F_c c_i E \end{aligned} \tag{2.48}$$

Similarly, for mass concentration, the corresponding mass flux of the ith species, j_i, is

$$\begin{aligned} j_i &= -\upsilon_i z_i F_c \rho_i \nabla\phi \\ &= -\upsilon_i z_i F_c \rho_i E \end{aligned} \tag{2.49}$$

υ_i is the *mobility*, a transport property similar to conductivity and diffusivity, measuring how mobile the charged species is. The mobility is related to diffusivity by $D_i = RT\upsilon_i$, where R is the gas constant and T is the temperature. The molar concentration equation 2.48 is the more frequently used version of these relations in electrochemical studies.

Combining the electric field and diffusion contributions to flux we arrive at.

$$\begin{aligned} j_i^* &= -\upsilon_i z_i F_c c_i \nabla\phi - D_i \nabla c_i + c_i \mathbf{u} \\ j_i &= -\upsilon_i z_i F_c \rho_i \nabla\phi - D_i \nabla \rho_i + \rho_i \mathbf{u} \end{aligned} \tag{2.50}$$

This equation is known as the Nernst-Planck equation.

2.2.8 Thermal Conductivity and Heat Transport

Heat transfer may occur due to conduction, convection, diffusion or radiation. Heat transport through convection, while contributing to energy transport, does not give rise to any new material transport properties. Similarly, heat can be transferred through interdiffusion of various species in multicomponent fluid mixtures, but this does not present a new transport property. However, if a temperature gradient is maintained in a fluid between two points, there will be flow of heat from the region of high temperature to the region of low temperature. There will be a linear relation between the heat flux and the temperature gradient according to the Fourier's law of heat conduction. If

considering temperature varying in all three directional dimensions, Fourier's law may be written as

$$\mathbf{q} = -\kappa \nabla T \tag{2.51}$$

where $\mathbf{q}$ is the 3-component vector rate of heat flow per unit area, κ is the thermal conductivity and T is the temperature. In the most common case, fluids are isotropic (having direction independent properties) so the coefficient κ has no directional characteristics (note that this is not the case for some solids). The thermal diffusivity α is defined as:

$$\alpha = \frac{\kappa}{\rho c_p} \tag{2.52}$$

where κ is the thermal conductivity coefficient seen in equation 2.51 and c_p is the specific heat at constant pressure. For incompressible material, the specific heat at constant pressure is equal to the specific heat at constant volume, $c_p = c_v = c$. the quantity in the denominator, ρc_p is the volumetric heat capacity.

As with viscosity, the thermal conductivity of gases increases with increasing temperature, whereas for most liquids, it decreases with increasing temperature. Polar liquids such as water are an exception, exhibiting a maximum in thermal conductivity along the thermal conductivity vs temperature curve.

2.3 Hydrodynamics of Particles and Macromolecules

Many microfluidic hydrodynamics problems deal with macromolecules within a solution having molar mass of greater than 10^5, and particles of sizes between 0.1 and 10 μm. Through performing experiments on colloidal particles, it is possible to create a model for their behaviour with solutions and separation of the particles may be accomplished by hydrodynamic means.

Batchelor [8] described the flow systems in these scales to be "microhydrodynamics" because it has several distinctive features from conventional bulk flow hydrodynamics

1. Inertial forces are small compared to viscous forces, therefore equations of motion for fluids is described by linear Stokes equation.

2. The free particle displacements due to Brownian motion within characteristic time intervals are significant.

3. Colloidal particles smaller than a micrometer settle slowly under gravity so they may be considered as "suspended" in the flow.

4. Interfacial surface forces between particles and the surrounding fluid are proportional to the square of the particle's characteristic size. Body forces are proportional to the cube of the characteristic particle size.

5. Electrokinetic effects are significant because particles acquire a charge in aqueous solutions (to be elaborated upon later)

Happel and Brenner describe how these particles behave at the low Reynolds number criteria (flow dominated by viscous flow in the laminar regime) [3]. Their work was expanded upon by Kim and Karrila [13] and Leal [7].

If body forces and inertial forces are neglected, the Navier-Stokes equation 2.37 reduces to:

$$\nabla\rho = \mu\nabla^2\mathbf{u} \tag{2.53}$$

which, together with the continuity equation for incompressible flow (Equation 2.12), defines the system flow. Due to the low Reynolds number condition, the equation system is linear and solutions are superposable.

An important result from this treatment of approximations is an equation of force that acts on spherical particles. A particle under translational motion of a velocity U experiences a resultant force F, which for a rigid sphere of radius, a, moving through a viscous fluid can be written as:

$$F = -6\pi\mu aU \tag{2.54}$$

This equation is called classical "Stokes drag law" and it is useful for approximating the electroosmotic force upon proteins, DNA and peptides which tend to conform to pseudo-spherical shapes with a radius of a. U is the flow velocity relative to the particle. Some molecules cannot be modelled as spheres but instead must be approximated as ellipsoidal. For the behaviour of prolate and oblate spheroids, we refer to Perrin's work [14] and subsequent corrections by Koenig [15].

2.3.1 Brownian Motion

In the absence of any external forces, any suspended particle will experience the same translational kinetic energy in the form of random thermal motion. The average translational kinetic energy for a particle regardless of its size is $\frac{1}{2}kT$ for each degree of freedom. So in 3 dimensional problems, the total kinetic energy is $\frac{3}{2}kT$ Given the definition of kinetic energy, we can write:

$$\frac{1}{2}m\left\langle U^2\right\rangle = \frac{3}{2}kT \tag{2.55}$$

$$\left\langle U^2\right\rangle = \frac{3kT}{m} \tag{2.56}$$

where $\langle U^2\rangle$ is the "time-averaged" mean square velocity , m is the particle mass, and T is the temperature of the medium. The velocities typically observed in equation 2.56, are much greater than the velocities which can be observed under a microscope, i.e., the typical value for the root mean square velocity $\langle U^2\rangle^{-2}$ is about 2 mm/s for a 1 μm radius particle at room temperature. The directions of these particles varies millions of times per second so the actual observable movement resolvable with a microscope is a diffusive flux that is due to Brownian motion over greater spans of time. Einstein's study of Brownian motion arrived at a simple formulation for the diffusion coefficient of spherical particles [16] by balancing the hydrodynamic forces on the particle with a steady thermodynamic force acting on each particle. For spherical particles, the translational diffusion coefficient is

$$D = \frac{kT}{6\pi\mu a} \tag{2.57}$$

which is commonly known as the Stokes-Einstein equation. The rotational diffusion coefficient is

$$D_{rot} = \frac{kT}{8\pi\mu a} \tag{2.58}$$

In a fluid at rest, a macromolecule will continuously change its configuration due to forces of Brownian motion. This is important to note that geometric properties such as the radius of gyration will fluctuate rapidly with time. The time-average values of free-particle Brownian motion and gyration may have some effect on the flow hydrodynamic behaviour and may be important to consider in microfluidic flows.

Fick's second law predicts how diffusion causes the concentration to change with

time.

$$\frac{\partial c}{\partial t} = D\frac{\partial^2 c}{\partial x^2} \tag{2.59}$$

where c is the concentration of particles in the solution, and x is the displacement. As a consequence of equation 2.59, we arrive at a useful evaluation of the mean-square distance diffused in time t to the diffusion coefficient. In one dimension:

$$\left\langle x^2 \right\rangle = 2Dt \tag{2.60}$$

In three dimensions

$$\left\langle r^2 \right\rangle = 6Dt \tag{2.61}$$

The dependence of average distance travelled on the square root of the time suggests that diffusion is an reasonable way for particles to traverse short distances, such as through membrane thicknesses or the interior of a small cell, but this motion is very inefficient for traversing longer distances.

2.4 Characteristic Parameters

It is possible to simplify the equations of change if we consider transport and physical properties to be constant and if we limit our attention to dilute, incompressible flow without species production and without heat sources. For electrolyte solutions we consider electrically neutral binary solutions or highly conducting solutions wherein electric fields are small so the convective diffusion equations for neutral species apply and energy equations are applicable. Under these conditions, we can summarize the overall continuity, momentum, convective diffusion and energy equations as follows

Mass Continuity	$\nabla \cdot \mathbf{u} = 0$	(2.62)
Momentum Continuity	$\rho\frac{D\mathbf{u}}{Dt} = -\nabla p + \mu\nabla^2\mathbf{u} + \rho g$	(2.63)
Convective Diffusion	$\frac{Dc}{Dt} = D_i\nabla^2 c_i$	(2.64)
Energy Diffusion	$\frac{DT}{Dt} = \alpha\nabla^2 T$	(2.65)

Table 2.2: Characteristic Parameter Equations.

Strouhal number	$\mathrm{St} = \dfrac{L}{\tau U}$	or	$\dfrac{L/U}{\tau} = \dfrac{\text{flow time scale}}{\text{unsteady time scale}}$
Froude number	$\mathrm{Fr} = \dfrac{U^2/gL}{\rho g}$	or	$\dfrac{\rho U^2/L}{\rho g} = \dfrac{\text{inertial force}}{\text{gravitational force}}$
Reynolds number	$\mathrm{Re} = \dfrac{UL\rho}{\mu}$	or	$\dfrac{\rho U^2/L}{\mu U/L^2} = \dfrac{\text{inertial force}}{\text{viscous force}}$
Peclet no. (therm.)	$\mathrm{Pe}_T = \dfrac{UL}{\alpha}$	or	$\dfrac{\rho c_p U(T_0 - T_w)/L)}{\kappa(T_0 - T_w)/L^2} = \dfrac{\text{heat convection}}{\text{heat conduction}}$
Peclet no. (diff.)	$\mathrm{Pe}_D = \dfrac{UL}{D}$	or	$\dfrac{U(c_0 - c_w)/L)}{D(c_0 - c_w)/L^2} = \dfrac{\text{mass convection}}{\text{mass diffusion}}$

α is the thermal diffusivity and D_i is the ith species diffusion coefficient or the electrolytic diffusion coefficient (written to include the i to differentiate it from the material derivative notation. Recall that $\frac{D}{Dt}$ is the material derivative that accounts for a moving reference frame. c_i is the concentration of the ith species. The energy diffusion equation 2.65 is often called the heat conduction equation. Heat flux occurs due to inter-diffusion and viscous dissipation is considered negligibly small in this equation.

There are several dimensionless parameters that can give a good idea of how fluids will behave during flow and we can see some of these in Table 2.2. In order to envision this behaviour, we make a choice of characteristic scales that are, to some extent, arbitrary but give an idea of the relative time scales, length scales, etc, for the given problem. L, U, τ are the characteristic length, characteristic speed and characteristic time where each of these values are related to the original values by a constant dimensionless variable denoted by an asterisk.

$$x = Lx^* \qquad u = Uu^* \qquad t = \tau t^* \tag{2.66}$$

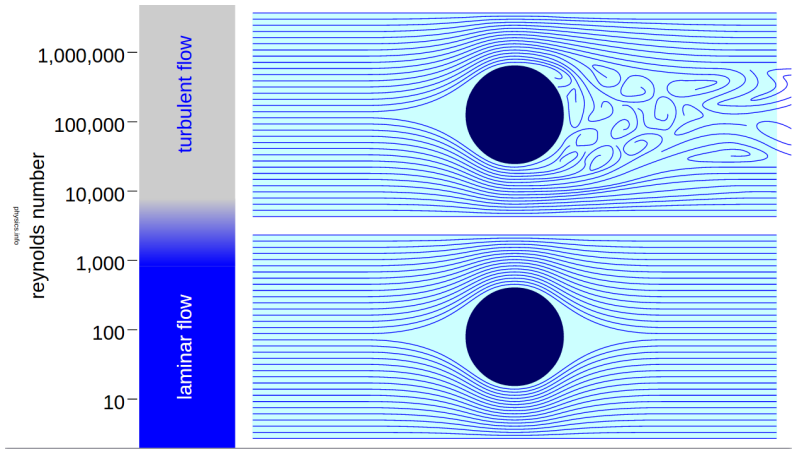

FIGURE 2.4-6: Illustration of laminar and turbulent regimes associated with Reynolds numbers (source: http://physics.info/turbulence [18])

The Strouhal number (St) is a measure of "unsteadiness" of the motion which is useful to describe oscillating flow mechanisms. The Froude number (Fr) is a value that describes the ratio of flow inertia to any external field (usually gravity). Usually, external fields are negligible and the Froude number is high but it is important in free surface flow computation [17] where it can be interpreted as analogous to wave "steepness".

The Reynolds number (Re) predicts flow patterns by quantifying the relative dominance of inertial forces versus viscous forces for a given flow condition. This value is particularly useful when scaling fluid dynamics problems to the micro or nano regime. There are two flow regimes that can be characterized by the Reynolds number. *Laminar flow* occurs at low Reynolds numbers where viscous forces are dominant. This flow is characterized by smooth and constant fluid motion. *Turbulent flow* occurs at high Reynolds numbers where inertial forces dominate and tend to generate vortices, eddies and flow instabilities.

Laminar flow	$\mathrm{Re} < 2300$
Transient flow	$2300 < \mathrm{Re} < 4000$
Turbulent flow	$4000 < \mathrm{Re}$

The Peclet number (Pe) is the ratio of convection rate to diffusion rate of some physical quantity (either mass or heat) driven by a gradient. The Peclet number is related to the Reynolds number because of their shared involvement with momentum transport. As such, the Peclet number may be written as a function of the Reynolds number.

$$\mathrm{Pe}_T = \frac{UL}{\nu}\frac{\nu}{\alpha} = \mathrm{Re}\,\mathrm{Pr} \qquad \text{Where Pr} = \frac{\nu}{\alpha} = \text{Prandtl number} \tag{2.67}$$

$$\mathrm{Pe}_D = \frac{UL}{\nu}\frac{\nu}{D} = \mathrm{Re}\,\mathrm{Sc} \qquad \text{Where Sc} = \frac{\nu}{D} = \text{Shmidt number} \tag{2.68}$$

Where $\nu = \mu/\rho$ is the kinetic viscosity and α is the thermal diffusivity. The Prandtl and Schmidt numbers are significant because they can be interpreted as intrinsic properties of the fluid whereas the Reynolds number is a property of the flow under specific conditions. Together, these numbers can act in concert to give an idea of the flow behaviour. A large Schmidt number in liquids, indicates that convection dominates over diffusion at moderate and even somewhat low Reynolds numbers. High Prandtl numbers in viscous fluids indicate that heat transfer by convection dominates over heat conduction so long as Reynolds numbers are not small.

For dilute solutions, the Schmidt number is very large so the Peclet number is generally large even if the Reynolds numbers are moderate. This means that in a bulk flow, over a solid surface, convection dominates over diffusion.

The Peclet number is also useful for qualitatively assessing the dispersion of an analyte within a solvent along a capillary tube. If we consider characteristic radial and axial dimensions, a and L respectively, within a capillary tube, the diffusion Peclet number can be used as a criterion to neglect radial diffusion if

$$\mathrm{Pe}_D \gg \frac{L}{a} \qquad \text{pure convection, neglect radial diffusion} \tag{2.69}$$

$$\mathrm{Pe}_D \gg \frac{a}{L} \qquad \text{pure convection, neglect axial diffusion} \tag{2.70}$$

These inequalities may be interpreted as indicating that the diffusion length ($\sqrt{D\tau}$) is small with respect to the characteristic lengths a and L.

2.5 Microfluidic Surfaces

For both hydrophilic and hydrophobic surfaces, it is important to have valid models for (1) inter-facial charge formation and (2) diffuse and condensed ion distributions. For hydrophobic surfaces, the origins of surface charge are less well understood and electrokinetic potentials observed due to experiments may be overestimated due to hydrodynamic slip (as will be discussed later in this chapter) [19][20]. Although hydrophobic

microfluidic systems are complex, measurements of material properties inferred from electrokinetic experiments in various systems are reproducible.

2.5.1 Surface Charges

Most substances acquire a surface electric charge when brought into contact with an aqueous (polar) medium. A separation of charge at solid-liquid interfaces occurs and this is central to electrokinetic flow discussed later in this chapter. There are several mechanisms by which a surface may acquire a net non-zero charge.

1. **Ionization or dissociation** – Chemical groups on a surface such as hydroxyl, carboxylic, and sulphate groups dissociate within an electrolytic solution thus tending to add a fixed surface charge at the interface of the electrolyte and the surface. Typically, microfluidic devices made from glass or fused-silica capillaries have silanol groups deprotonate in contact with the electrolyte (Equation 2.71). The extent to which this deprotonation occurs depends on the local electrolyte ion concentration and the pH.

$$SiOH \overset{K_a}{\longleftrightarrow} SiOH^- + H^+ \tag{2.71}$$

   For glass/silica devices – as used in this project – the pK_a for this reaction is approximately 4.9. This determines the degree of charge separation along the surface and therefore the electrokinetic properties.

2. **Lattice ion adsorption** – Suspended particles tend to have different absorption affinities between the crystalline and aqueous phases when in electrolyte solutions. Interstitial ions can adsorb onto crystalline lattice surface sites and thus provide a net charge. There is a dynamic equilibrium between interstitial ions and ions at lattice positions.

3. **Preferential adsorption** – High surface affinity can overcome electrostatic repulsion of surface charges or adsorbed ions. Ionic surfactants can preferentially adsorb onto a surface.

   In a special case when referring to Nernstian surfaces, both preferential adsorption and lattice ion adsorption mechanisms above above can be described as a function of salt concentration.

$$\phi_0 = \frac{k_B T}{z\ell} \ln \frac{[A^+]}{[A^+]_{pzc}} \tag{2.72}$$

ϕ_0 is the surface potential, k_B is Boltzmann's constant, T is the temperature, z, is the valence of the ion, ℓ is the elementary charge, and pzc indicates the point of zero charge. However, Nernstian materials are rarely used in microfluidics so this is a unique situation where the potential boundary can be defined simply.

4. **Isomorphous substitution** – Ions trapped within a lattice where substitution of one ion for another of the same size but different valency can take place. This can result in a charged surface.

2.5.2 The Electric Double Layer

The electric double layer (also referred to as inter-facial potential, or surface potential, or the Debye layer) is an important phenomenon in the study of microfluidic transport mechanisms that was first realized by Hermann von Helmholtz [21]. When surface charges are formed by the mechanisms mentioned earlier, an electric field is created which attracts ions of opposite charge (counterions) within the solution toward the surface while repelling ions of similar charge (co-ions). The resulting layers of positive and negative charge regions are called the electric double layer (EDL). The fluid adjacent to the surface that contains the free charges can be manipulated by external electric fields to induce flow.

A polarization effect is created due to the presence of the Debye layer. The counterions concentrated near the surface effectively shield the bulk solution from the surface charge. The resultant distribution is seen in Figure 2.5-7. λ_D is defined as the Debye screening length. The Debye length is the thickness of the region surrounding a surface that screens the electroneutral bulk from the effects of charges on the surface. That is, the concentration of co-ions (C_-) in the bulk region remains the same as the concentration of the counterions (C_+).

Because these ions have a finite temperature, they experience thermal motion and the ions at the edge of the double layer cloud of ions where the electric field is weak, they may escape the potential well if they posses sufficient thermal energy. The edge of the double layer defined to be at the position where the potential energy is approximately equal to the thermal energy of the counterions, which is approximately $RT/2$ per mole for each degree of freedom (dimension of motion available). Recall that R is the molar gas constant used for convenience, $RT = kT \cdot N_A$ where N_A is Avagadro constant.

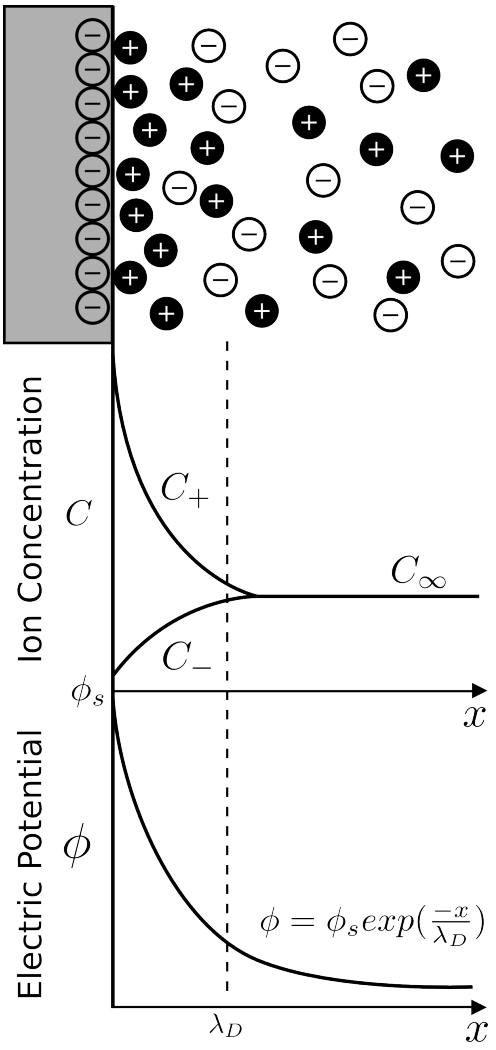

FIGURE 2.5-7: Illustration of the Debye layer charge distribution on a surface..

Debye Sheilding Distance

The Poisson equation in Laplacian form for a charge density of ρ_e in an electrolyte solution with a permitivity ε, is

$$\nabla^2\phi = \frac{-\rho_e}{\varepsilon} \tag{2.73}$$

Recall the Lorentz relations for force on a charged particle:

$$\mathbf{f}_e = \rho_e \mathbf{E} \tag{2.74}$$

$\mathbf{f}_e$ is the electric body force per unit volume and charge density can be defined in

relation to electrolyte concentration as:

$$\rho_e = F_c \Sigma z_i c_i \tag{2.75}$$

where $F_c = e \cdot N_A = 9.65 \times 10^4$ C mol^{-1} is the Faraday constant for a singly ionized species. $e = 1.602 \times 10^{-19}$ coulombs is the elementary charge, z_i is the valence of the i-th ionic species, and c_i is the concentration of the charge species, i.

We can write equation 2.73 as

$$\frac{d^2\phi}{dx^2} = \frac{F_c z c}{\varepsilon} \tag{2.76}$$

where c is taken to be the average molar counter-ion concentration. The electrical potential energy per mole of an ion is

$$W = F_c z \phi \tag{2.77}$$

Note that "electrical potential energy" W (also known as *work*) is distinct from *electrical potential*, ϕ. Integrating equation 2.76 to find the change in W across a planar layer of width x we get

$$\Delta W = \frac{F_c^2 z^2 c x^2}{2\varepsilon} \tag{2.78}$$

which applies if the electric field is zero on one side of the plane. Under only translational motion, the value of x for which the value of ΔW equals RT gives the Debye length or "Debye shielding distance"

$$x = \lambda_D = \sqrt{\frac{\varepsilon RT}{2F_c^2 z^2 c}} \tag{2.79}$$

If the electrolyte is symmetrical ($c_+ = c_-$) at 25°, λ_D can be simplified to

$$\lambda_D = \frac{9.61 \times 10^{-9}}{\sqrt{z^2 c}} \tag{2.80}$$

In this case, λ_D is units of meters and c is in mol/m^3. It is clear that the Debye Length decreases inversely with the square root of the average molar concentration, c. Higher concentrations result in shorter Debye lengths.

Typical Debye lengths for concentrations of 10^2 mol m^{-3} and 1 mol m^{-3} are 1 nm and 10 nm respectively. If the dimensions of the system (L) is much larger than λ_D, then all local charge concentrations are shielded out of a short distance compared with

L. This leaves the bulk fluid free of large electric potentials. However, in the case of very small microscopic capillaries, the double layer is central to calculation of ion fluxes and fluid flow.

Double Layer Charge Distribution

To visualize the profile of ion concentration within the double layer we recognize that the ions within the layer follow the Boltzmann distribution

$$c_{\pm} = c_0 exp\left(\frac{\mp z F_c \phi}{RT}\right) \tag{2.81}$$

As the concentration far from the surface approaches c_0, the potential approaches zero ($\phi \to 0$). By applying the above equation to equation 2.75, and simplify, we can show the density, ρ_e becomes

$$\rho_e = -2F_c z c_0 \sinh\left(\frac{z F_c \phi}{RT}\right) \tag{2.82}$$

Plugging this back into equation 2.73, we have

$$\frac{d^2\phi}{dx^2} = \frac{2 z F_c c_0}{\varepsilon} \sinh\left(\frac{z F_c \phi}{RT}\right) \tag{2.83}$$

For small potentials $zF_c\phi \ll RT$, the $\sinh(zF_c/RT)$ can be expanded to give the "Debye-Huckel approximation"

$$\frac{d^2\phi}{dx^2} = \frac{\phi}{\lambda_D^2} \tag{2.84}$$

Integrating equation 2.84, under the conditions that $\phi = \phi_s$ at the surface (where $x = 0$), and also considering that both ϕ and $d\phi/dx$ are zero as $x \to 0$, we have

$$\phi = \phi_s exp\left(-\frac{x}{\lambda_D}\right) \tag{2.85}$$

Equation 2.85 shows how the Debye length is the $1/e$ decay distance from the surface (at low potentials). Close to the surface, the potential is higher and the Debye-Huckel approximation is not quite accurate. The actual potential decreases faster than the exponential fall off suggests.

The limitation of the diffuse double layer treatment is the assumption that ions in the electrolyte are point charges, when in reality they are of finite size. This means that the center of an ion can only approach the surface to within the hydrated radius before becoming specifically adsorbed. To account for this, a segment called the "Stern layer"

[22][23] is defined as part of the double layer that starts approximately one hydrated ion radius from the surface. J. O'M. Bockris, M. A. V. Devanthan and K. Alex Muller [24] expanded on the Stern model by proposing that the double layer included the action of solvent in the interface. They suggested that molecules of water or some solvent would have a fixed alignment to the surface. The first layer of solvent molecules would be strongly oriented to the electric field from the surface. The inner Helmholtz plane (IHP) passes through the centers of specifically adsorbed ions that are directly adjacent to the surface and the outer Helmholtz plane (OHP) passes through the centers of solvated ions just outside the adsorbed ions on the surface (a scheme previously introduced by D.C. Grahame [25]). The diffuse layer is beyond the OHP. This model is illustrated in 2.5-8 with a negative surface charge and water solvation symbolized with arrows inside the H_2O molecule.

The potential of the Stern plane is close to the electrokinetic potential or "zeta" potential (ζ). Zeta potential is used to describe the potential at the shear surface between the charge surface and the electrolyte solution. This is somewhat arbitrary but it is typically characterized as the plane at which mobile portion of the diffuse layer can "slip" or flow past the charged surface.

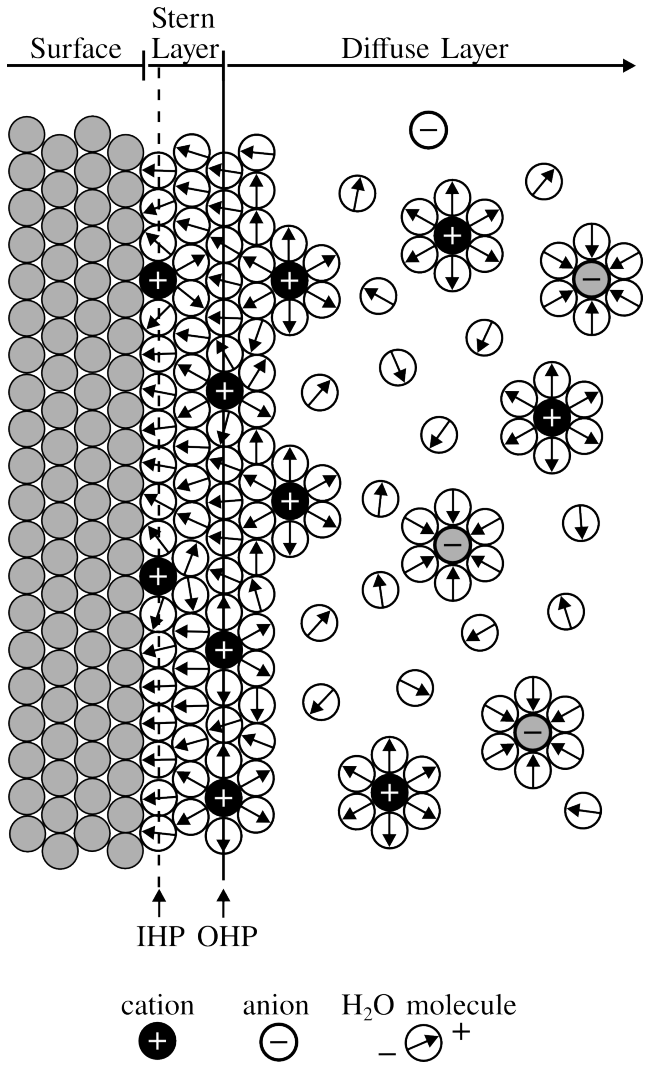

FIGURE 2.5-8: Electric double layer structure showing the Stern layer and Helmholtz planes. IHP refers to the "inner Helmholtz plane" and OHP refers to the "outer Helmholtz plane".

2.6 Electrokinetics

There are four main electrokinetic phenomena as described by Duncan Shaw [26]:

1. Electrophoresis – a charged object (surface) dissolved or suspended in a medium and moving with respect to that liquid due to an applied electric field.

2. Electroosmosis – The movement of a liquid relative to a charged surface due to an applied electric field.

3. Streaming potential – the electric field created when liquid is made to flow along

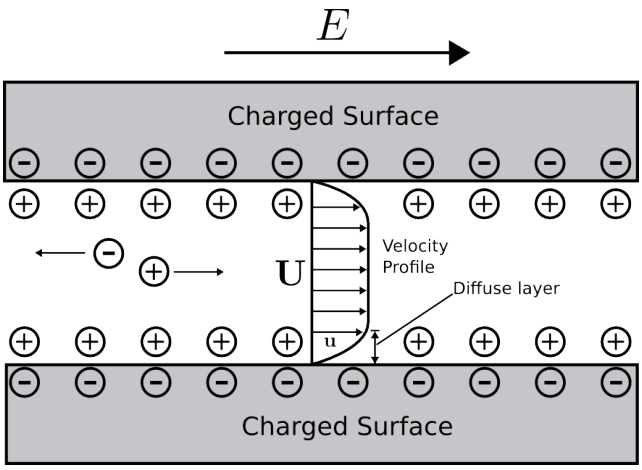

FIGURE 2.6-9: Cross-sectional illustration of electroosmotic flow of water through a fluidic channel.

a stationary charged surface. (reverse of electroosmosis).

4. Sedimentation potential – the electric field created when charged particles move relative to stationary liquid (opposite of electrophoresis).

2.6.1 Electroosmosis

To estimate electroosmotic velocity in a capillary by a uniform electric field applied along the axis as shown in Figure 2.6-9, we assume the electric body force per unit volume to be given by $f_e = \rho_e \mathbf{E}$. The momentum equation shown earlier (equation 2.37, can be written as:

$$\rho \frac{D\mathbf{u}}{Dt} = -\nabla p + \mu \nabla^2 \mathbf{u} + \rho g + \rho_e \mathbf{E} \tag{2.86}$$

If we assume inertia free flow with no pressure gradient and negligible gravitational forces, this reduces to simply:

$$\mu \nabla^2 \mathbf{u} = -\rho_e \mathbf{E} \tag{2.87}$$

Assuming E runs in the positive x direction, we know that all derivatives of u with respect to x are zero. If λ_D is small compared to the transverse dimensions of the channel, then we can simplify into a one dimensional form that is suitable for infinite

plane channels.

$$\mu\frac{\partial^2 u}{\partial y^2} = -\rho_e E_x = \epsilon\frac{\partial^2 \phi}{\partial y^2}E_x \tag{2.88}$$

The ρ_E term was eliminated with poissons equation $\nabla^2\phi = -\rho/\epsilon$. Integrating both sides:

$$\mu\frac{\partial u}{\partial y} = -\rho_e E_x = \epsilon\frac{\partial \phi}{\partial y}E_x \tag{2.89}$$

Setting $\partial u/\partial y = \partial\phi/\partial y = 0$ at $y \to \infty$ at the edge of diffuse layer. We can integrate once more with $\phi = \zeta$ (the zeta potential point) at $u = 0$ we have:

$$U = \frac{\epsilon\zeta E_x}{\mu} \tag{2.90}$$

This equation is the helmholtz-Smoluchowski equation for electroosmotic velocity past a plane charged surface. If the double layer thickness is very small compared with the channel dimensions ($a/\lambda_D \ll 100$ where a is the channel radius), the fluid moves in a plug flow. Velocity is at a "slip" condition with the wall and so the velocity profile goes from U to zero discontinuously. For a finite thickness diffuse layer, the flow profile looks like that of Figure 2.6-9. The electroosmotic velocity (U) represents the velocity at the edge of the diffuse layer extending into the bulk flow.

2.6.2 Liquid Slip

Slip refers to any situation in fluid dynamics where the value of the tangential component of velocity appears to be different from that of the solid surface immediately in contact with it. In other words, a non-zero velocity of liquid molecules at the channel wall is called liquid slip. "No slip" describes a condition where the liquid in the first molecular layer is stationary and all other molecules are sheared past the first molecular layer. Conversely, "slip" describes a condition where the first molecular layer DOES flow but with high friction with the wall. Figure 2.6-10 shows three illustrative examples of slip states, quantifying the degree of slip with a quantity called "slip length" (λ_S) as described by Lauga et al [27]. Highly hydrophobic walls lower the friction with the wall and less force is required for a given flow velocity. Therefore, the slip condition is an important consideration in nanofluidics since it may drastically reduce the required pressure to induce flow in pressure driven flow systems. A review of low friction flows

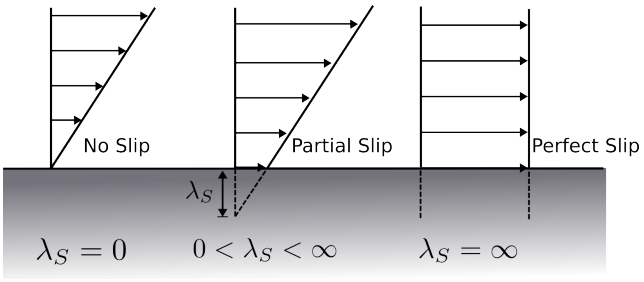

FIGURE 2.6-10: Three possible cases of slip flow past a surface. Slip length is λ_S [27].

and their applications in carbon nanotubes was done by Whitby and Quirke [28].

2.6.3 Wall and Adsorption Effects

The effects of lateral diffusion are much more pronounced in nanofluidic channels than in microfluidic channels. The rate at which molecules will come in contact with the nanochannel walls by means of diffusion is greatly increased since this rate is determined by the inverse square of the lateral width of the channel. With an increased frequency of molecule-wall interactions, the frequency of adsorption events increases as well [29]. The tendency for molecules to adsorb on the channel wall can lead to a significant decrease in transport rate [30][31].

Surface roughness can have an effect on transport properties as well. Simulations show that a rough surface can cause up to 50 percent decrease in velocity (Qiao et al. [32]).

2.6.4 Electrophoresis

It can be shown that spherical charged particles submerged in a fluid possesses a double electric layer much like a solid channel surface in contact with a fluid. The potential at the edge of the diffuse layer is called the zeta potential ζ similarly to the charged surface case [2]. For a negatively charged particle, we have

$$\zeta = \frac{q}{4\pi\epsilon a} - \frac{q}{4\pi\epsilon(a + \lambda_D)} \tag{2.91}$$

The zeta potential is effectively found from the superposition of two potentials: one arising directly from a total charge q on the surface of the particle at radius a and

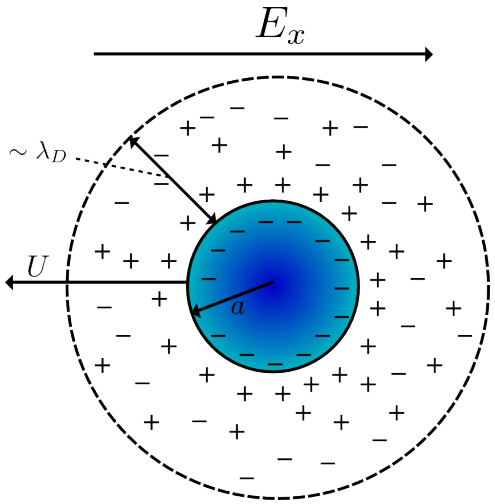

FIGURE 2.6-11: Spherical partical motion due to electrophoretic force.

the other arising from a counteracting charge $-q$ filling the sphere of radius $a + \lambda_D$ representing the edge of the debye layer (Figure 2.6-11).

It is possible to begin assuming a large Debye length ($\lambda_D > a$) such that the particle may be treated like a point charge in an unperturbed electric field E_x. The coulomb force is then

$$F_{EP} = qE_x \tag{2.92}$$

where q is the net charge between the charged sphere surface and the diffuse charge in the debye layer sphere surrounding it. The velocity with respect to the surrounding fluid can then be found through the familiar Stokes' Drag Law.

$$qE_x = 6\pi\mu U a \tag{2.93}$$

We can then use the zeta potential relation in equation 2.91 with the above equation to find the electrophoretic velocity.

$$U = \frac{2}{3}\frac{\zeta\epsilon(1 + a/\lambda_D)E_x}{\mu} \approx \frac{2}{3}\frac{\zeta\epsilon E_x}{\mu} \tag{2.94}$$

The approximation on the right hand side of equation 2.94, neglecting the a/λ_D term is the Huckel equation. It is applicable only to mediums of low conductivity. For a particle with $\lambda_D = 10$ nm, and a particle radius of 1 nm, the λ_D/a term would be

10. Therefore, there is need to consider a case for smaller Debye length scenarios.

Henry (1930) [33] accounted for the effects of electrophoretic retardation, which results from the fact that ions in the double layer will have a net movement in the opposite direction to that of the particle. Henry's treatment [33], although a lengthy derivation, resulted in a more accurate relation than the Huckel equation.

$$U = \frac{2}{3}\frac{\zeta \epsilon E_x}{\mu} f(\alpha) \tag{2.95}$$

where

$$\begin{aligned} f(\alpha) = 1 + \frac{1}{16}\alpha^2 - \frac{5}{48}\alpha^3 - \frac{1}{96}\alpha^4 + \frac{1}{96}\alpha^5 \\ + \frac{1}{8}\alpha^4 e^{\alpha}\left(1 - \frac{\alpha^2}{12}\right)\int_{\infty}^{\alpha}\frac{e^{-t}}{t}dt \end{aligned} \tag{2.96}$$

where $\alpha = a/\lambda_D$. This is known as the Henry equation and it is applicable under the following assumptions.

- The double layer is undistorted by the movement of the ions within the double layer.
- The Debye-Huckel approximation is applicable (the surface potential on the particle is low)
- The resulting viscous flow is inertia free

Equation 2.95 does not accounted for surface conductance or the fact of the particles becoming polarized at the surface from the movement of charge. Also, since the double layer is undistorted, it does not account for "relaxation" which distorts the sphericity of the debye layer into an asymmetric shape so the center of the double layer lags behind the center of the particle. Figure 2.6-12) shows how as the particle moves to the left, the counterions are left behind. Restoring the symmetrical double layer from the counterions in the new region of liquid entered by the particle requires time, hence the term "relaxation" effect. Therefore, during movement, the double layer is not truly concentric with the particle and the displacement of charge sets up a slight electric field that reduces the electrophoretic velocity.

To properly account for the relaxation effect requires calculating the total electric potential with the charge density by solving the Nernst-Planck equations and Navier-Stokes equation. Even for spherical cases, analytical solutions are complex. However, numerical solutions have been computed by Wierseme et al. [34].

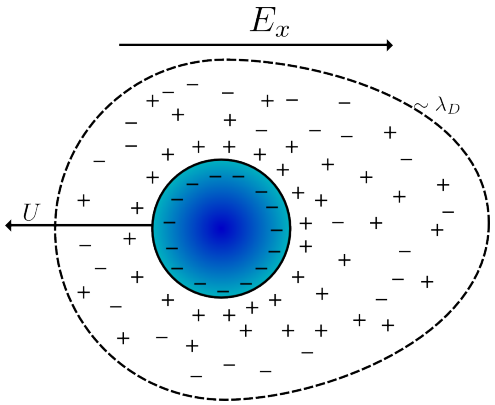

FIGURE 2.6-12: Distortion of the double layer due to electrophoretic effects.

2.7 Conclusion

We have described some of the basic theory pertinent to the study of nanofluidics and particularly those of relevance to the nanofluidic device investigated in this manuscript. We conclude that liquid flow and electrokinetics in nanochannels concerning aqueous electrolytes can be modelled using continuum theory equations of Navier-Stokes for liquid flow problems and Nernst-Planck equations for electrokinetic problems. These have been found to be applicable for channel dimensions down to 10 nm.

Nanofluidic applications of greatest potential are those which exploit the large surface to volume ratio within nanochannels. At high surface to volume ratios, interactions of solutions and molecules with the walls of the channel become increasingly important, presenting enhanced effects of electroosmosis and wall adsorption. Nanofluidics exhibits some superiority over microfluidics, particularly in the case where the double layer overlaps within the channel ($\lambda_D > a$), because greater transport control of individual charged molecules becomes possible. Furthermore, at nanofluidic length scales, the Peclet number is very low, meaning that mass diffusion rates dominate mass convection. Particles can travel between the nanofluidic surfaces so quickly, averaging out all frustrated flow caused by the comparatively slow convective mass flow, reducing a 3 dimensional flow problem to an approximated 1-dimensional axial flow problem which permits stable electrokinetic trapping, a phenomenon fundamental to this thesis project.

References

[1] Hsueh-Chia Chang and Leslie Y. Yeo. *Electrokinetically Driven Microfluidics and Nanofluidics*. Cambridge University Press, 2010. 17

[2] Ronald F. Probstein. *Physicochemical Hydrodynamics: An Introduction*. Wiley, 2nd edition edition, 2003. 17, 51

[3] J Happel and H Brenner. *Low Reynolds Number Hydrodynamics: With Special Applications to Particulates*. Springer Science & Business Media, 1983. 17, 36

[4] Nam-Trung Nguyen and Steven T. Wereley. *Fundamentals and Applications of Microfluidics*. Artech House, 2002. 17

[5] T. Zlatanovski. Axisymmetric creeping flow past a porous prolate spheroidal particle using the brinkman model. *The Quarterly Journal of Mechanics and Applied Mathematics*, 52(1):111–126, 1997. 18

[6] Christopher Stover. Reynolds transport theorem. http://mathworld.wolfram.com/ReynoldsTransportTheorem.html. 20

[7] Gary Leal. *Advanced Transport Phenomena: Fluid Mechanics and Convective Transport Processes*. New York: Cambridge University Press, 1999. 20, 36

[8] G.K Batchelor. *An Introduction to Fluid Dynamics*. Cambridge University Press, 2000. 26, 35

[9] Marc J. Madou. *Solid-State Physics, Fluidics, and Analytical Techniques in Micro- and Nanotechnology*. CRC Press, 2011. 31

[10] W. Loose and S. Hess. Rheology of dense model fluids via nonequilibrium molecular dynamics: Shear thinning and ordering transition. *Rheologica Acta*, 28(2):91–101, 1989. 31

[11] R. Qiao and N. R. Aluru. Ion concentrations and velocity profiles in nanochannel electroosmotic flows. *The Journal of Chemical Physics*, 118(10):4692–4701, 2003. 32

[12] D.R. Lide. Crc handbook of chemistry and physics, online version, http://www.hbcpnetbase.com, crc press, boca, fl, 2015. 32

[13] Sangtae Kim and Seppo Karrila. *Microhydrodynamics: Principles and Selected Applications*. Dover Publications, unabridged edition edition, June 2005. 36

[14] Perrin. Mouvement brownien d'un ellipsoide. *Journeal de physique et Le Radium*, 7(7):1–11, 1934. 36

[15] Seymour H. Koenig. Brownian motion of an ellipsoid. a correction to perrin's results. *Biopolymers*, 14(11):2421–2423, 1975. 36

[16] Albert Einstein. *Investigations on the Theory of the Brownian Movement*. Courier Corporation, 1956. 37

[17] Hubert Chanson. *Hydraulics of Open Channel Flow*. Butterworth-Heinemann, 2004. 40

[18] Glenn Elert. The physics hypertextbook. http://physics.info/turbulence/; accessed: January, 2015. xv, 40

[19] H. A. Stone, A. D. Stroock, and Armand Ajdari. Engineering flows in small devices: Microfluidics toward a lab-on-a-chip. *Annual Review of Fluid Mechanics*, 36(1):381 – 411, 2004. 41

[20] JC McDonald, DC Duffy, JR Anderson, DT Chiu, H Wu, OJ Schueller, and GM Whitesides. Fabrication of microfluidic systems in poly(dimethylsiloxane). *Electrophoresis*, 21(1):27–40, January 2000. 41

[21] Hermann von Helmholtz. Ueber einige gesetze der vertheilung elektrischer strme in krperlichen leitern mit anwendung auf die thierisch-elektrischen versuche. *Annalen der Physik und Chemie*, 165(6):211–233, 1853. 43

[22] O. Z. Stern. On the theory of electrolytic bilayer. *Electrochemistry*, 30(508), 1924. 47

[23] Rangadhar Pradhan Analava Mitra Soumen Das. Extended stern model. *Journal of Applied Solution Chemistry and Modeling*, 1:74–78, 2012. 47

[24] J. O'M. Bockris, M. A. V Devanthan, and K. Mueller. *Proceedings of the Royal Society of London, Series A*, 274(55), 1963. 47

[25] D.C. Grahame. The electrical double layer and the theory of electrocapillarity. *Chemistry Review*, 41(3):441–501, 1947. 47

[26] Duncan J. Shaw. *Introduction to Colloid and Surface Chemistry (Fourth Edition)*. Butterworth-Heinemann, Oxford, fourth edition edition, 1992. 48

[27] Eric Lauga, Michael P. Brenner, and Haoward A. Stone. *Handbook of Experimental Fluid Dynamics*, chapter Microfluidics: The No-Slip Boundary Condition. YSpringer, New York, 2005. xv, 50, 51

[28] M. Whitby and N. Quirke. Fluid flow in carbon nanotubes and nanopipes. *Nature Nanotechnology*, 2(2):87–94, 2007. 51

[29] H. Poppe. Some reflections on speed and efficiency of modern chromatographic methods. *Journal of Chromatography A*, 778(1-2):p. 3–21, 1997. 51

[30] Y. Y. Kievsky, B. Carey, S. Naik, N. Mangan, D. ben Avraham, and I. Sokolov. Dynamics of molecular diffusion of rhodamine 6g in silica nanochannels. *The Journal of Chemical Physics*, 128(15):–, 2008. 51

[31] N.F.Y. Durand, Arnaud Bertsch, Mina Todorova, and Philippe Renaud. Direct measurement of effective diffusion coefficients in nanochannels using steady-state dispersion effects. *Applied Physics Letters*, 91(20), 2007. 51

[32] R. Qiao. Effects of molecular level surface roughness on electroosmotic flow. *Microfluidics and Nanofluidics*, 3(1):33–38, 2007. 51

[33] D. C Henry. The cataphoresis of suspended particles. part i. the equation of cataphoresis. *Proceedings of the Royal Society of London A*, 133:106129, 1931. 53

[34] P.H. Wiersema, A.L. Loeb, and J.T.G. Overbeek. Calculation of the electrophoretic mobility of a spherical colloid particle. *Journal of Colloid and Interface Science*, 22:7899, 1966. 53

This chapter has been adapted from a published work in analytical chemistry: "Nanochannel pH gradient Electrofocusing of Proteins", Michael A. Startsev, David W. Inglis, Mark S. Baker, And Ewa M. Goldys; Anal. Chem., 2013, 85,(15), pp 7133-7138.

3

Nanochannel pH Gradient Electrofocusing of Proteins

Abstract. We demonstrate matrix-free pH gradient electrofocusing of proteins within an 85-nm deep nanochannel. In contrast to conventional isoelectric focusing where the fluid does not move, this pH gradient method traps protein molecules flowing through a channel by balancing electric forces due to pH-dependent protein charge and viscous drag forces caused by electroosmosis. The nanoscale depth of the device and the low voltage used limit convection relative to diffusion, thus producing a stable focused band of protein. R-phycoerythrin (RPE) and Dylight labeled streptavidin (Dyl-Strep) were focused within a nanochannel using applied voltages between 0.4 and 1.6 V. Concentration enhancement factors of over 380 have been achieved within 5 minutes. Varying the buffer pH (between 2.7 and 7.2) at the boundaries of the nanochannel affected the shape of the focused bands. For RPE, a pH span of 4.5 (pH 2.7 to 7.2) yielded the narrowest peak while a span of 2.4 (pH 2.7 to 5.1) produced a significantly wider peak. Such matrix-free nanofluidic devices with pH gradient electrofocusing may enable on-chip integration of orthogonal separation techniques with mass spectrometry offering labour savings and enhanced performance.

3.1 Introduction

Analytical chemistry techniques such as capillary zone electrophoresis (CZE) [1], 2D gel electrophoresis [2], high-performance liquid chromatography (HPLC) [3][4], ELISA [5] and mass spectrometry (MS) [6] are fundamental to proteomic research. A range of counter flow gradient methods have been developed for focusing and separating molecules, and some of these have been used with mass spectrometry in so called orthogonal separations. Isotachophoresis (ITP) [7][8] and gradient elution moving boundary electrophoresis (GEMBE) [9][10] are two examples of methods of electrokinetic protein focusing and separation involving moving focus bands while methods such as capillary isoelectric focusing (cIEF) [11] produce constant focus positions. Our approach is a counter flow gradient method as it employs bulk flow to counteract a gradient in analyte velocity to produce a stationary equilibrium focus position. Ion concentration polarization (ICP) [12][13][14] has been observed in devices similar to the device used in this work and yielded high preconcentration enhancement factors near the entrances of the micro-nanochannels junctions. However, preconcentration using this technique is limited as its capacity for separation has not been demonstrated. Common types of counter-flow gradient methods are conductivity gradients [15], chromatographic velocity gradients (counteracting chromatographic electrophoresis or (CACE) [16][17], current gradients (electric field gradient focusing (EFGF) [18][19], the electrode array technique [20], temperature gradient focusing [21][22], and finally – the method of interest in this work – pH gradients. Early attempts at protein focusing based on pH gradient principles involved containing acidic and alkaline solutions, respectively, at the anode and cathode of a fluid channel device and inducing a voltage difference at the electrodes [23]. A major drawback of this technique was that the pH gradients formed by the buffers were impossible to stabilize over the time required for focusing and the ongoing migration of buffer and titrant ions was responsible for the destruction of electrophoretic focus [24]. The problems with stability of the pH gradients were largely overcome by the introduction of immobilized pH gradient polyacrylamide gels and ampholytes used within a dispersion medium which are able to maintain a stationary pH gradation under the influence of an electric field. This stability enabled current isoelectric focusing techniques which are consistent and accurate enough for commercial applications and later enabled the development of the 2D electrophoresis [2]. However isoelectric focusing and pH gradient techniques are not routinely coupled directly to mass spectrometry in part because the carrier ampholytes which establish the pH gradient negatively affect MS performance. Selective downstream analysis has

been demonstrated before by Chingin et al. [25], this method involved multiple buffer and electrode junctions to trap and release focus bands with a high degree of control. In this study, we demonstrate matrix-free pH gradient focusing, a novel approach to protein focusing that also presents a promising potential application for on-chip protein separations. A pH gradient exists along a nanofluidic channel connecting two reservoirs of different pH. An electric field applied across the channel exploits the inherent pH-dependent charge properties of proteins in concert with counteracting electro-osmotic (EO) flow such that the proteins become immobilized at an equilibrium position along the channel. We investigate this phenomenon using a naturally fluorescent protein, R-phycoerythrin (RPE) and fluorescently labeled streptavidin (Dyl-Strep). Unlike most other electrophoretic concentration enhancement methods [26][27], this approach works with a continual supply of protein sample and buffer, so that it may be possible to eventually trap a detectable amount of low abundance molecules. This is in contrast to conventional techniques such as capillary electrophoresis that use a single sample injection at the start of the experiment. Such methods are limited to focusing only the quantity of molecules within the initial injection volume [28] which may be insufficient for the detection of low abundance molecules.

3.2 Explanation of the Concentration Mechanism

The electrokinetic forces that govern flow within a nanofluidic channel result from the inherent charge separation phenomena at solid-liquid interfaces. The silanol groups [29] bound to the fused-silica surface of the channel in contact with an aqueous solution experience a pH-dependent deprotonation which results in a bound surface charge. This, in turn, produces the electric double layer (EDL) [30], a mobile ion distribution near the silica surface. When an electric field is applied along the walls of this channel, the mobile ions in the EDL experience an electric force and move, resulting in EO flow. In conditions where the Debye length is small compared with the diameter of the channel, the Helmholtz-Smoluchowski equation predicts a plug-like velocity profile of the EO flow with the velocity V_{HS} [30] given by

$$V_{HS} = \frac{\varepsilon_r \varepsilon_o \zeta E}{\mu} \tag{3.1}$$

Here, E is the local electric field, μ is the viscosity of the buffer solution, ε_r is the permittivity of the medium, ε_o is the permittivity of free space, and ζ is the zeta potential of the channel surface. In our case, q changes along the length of the channel

due to the pH gradient applied. However the total fluid flow at the input and output must be the same since the aqueous solution is an incompressible fluid. This results in frustrated flow within the channel [30], a condition where the fluid velocity vector at a certain position along the depth of the channel can be oriented opposite to the bulk flow. Due to the pH variation along the channel, silanol groups will deprotonate at different rates along the channel resulting in a lower surface charge along the channel near the low pH end and a higher surface charge along the surface near the high pH end. If this effect is significant enough, the flow profile through the depth of the channel may appear as in Figure 3.2-1[31].

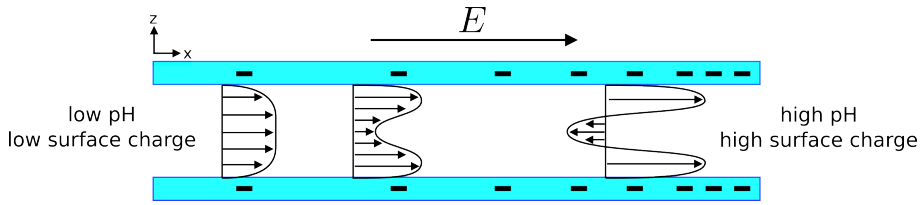

FIGURE 3.2-1: Illustration of frustrated flow due to local surface charge variation along the channel.

The significance of the frustrated flow relative to the diffusion is captured by the Peclet number (Pe_L)[32]:

$$Pe_L = \frac{LU}{D} \tag{3.2}$$

where U is the particle transport speed, L is the characteristic length (85 nm) and the D is the diffusion coefficient. For the low voltages used here, we observe transport speeds along the length of the channel of less than 50 μm/s, giving a Pe_L number of less than 0.2. This implies that the protein molecules diffuse quickly across the channel depth compared with the EO fluid velocity, averaging the flow profile and allowing us to use a one dimensional approach where we assume that the EO fluid velocity and force on the protein molecules are independent of the position within the channel. This EO flow exerts a force on the protein. In the case of proteins with a quasi-spherical conformation, in which a represents the effective radius of the spherical protein molecule, this force can be approximated as follows [33]:

$$F_{EO} = 6\pi\mu a V_{HS} \tag{3.3}$$

The second significant force on the protein is the electrophoretic (EP) force which can

be similarly approximated as a Coulomb force on a point charge:

$$F_{EP} = qE \tag{3.4}$$

where q is the effective charge of the protein at the pH it experiences in the channel. In this study, q is the parameter that varies with pH along the channel. At a certain position within the channel the protein acquires a value of charge q so that the EP and EO forces balance. In this case the net drift velocity of the protein becomes zero and thus a protein focus band will form at that position. In this simplified 1D case, focusing takes place when the total force, $F = 6\pi\mu a V_{HS}$, is zero. Additionally, to achieve a stable focus, the derivative of the force at the focus point must be negative. i.e. the EO and EP forces on either side of the net zero velocity point must be oriented toward the focus point. Figure 3.2-2(a) illustrates the effect of combined electrokinetic forces on a protein. In this example, an electric field applied axially along the length of the channel induces an EO force on the sheath of positive charges along the walls of the channel in the direction of the electric field. Simultaneously, the electric field also applies a counteracting EP force on the protein (blue sphere) proportional to the instantaneous negative charge of the protein. As suggested by Figure 3.2-2(b), the protein charge decreases as pH increases. Within the channel, the protein reaches a position where the protein charge-dependent EP force is equivalent to the counteracting EO force as shown by the intersection of red and blue lines in Figure 3.2-2(c). At this position, the protein becomes immobilized. If the protein moves away from the focus position by means of diffusion, the charge of the protein will change again (due to altered pH) and the net electrokinetic force will become nonzero in the direction toward the focus point. The protein is thus "trapped" at the electrokinetic focus point, which, unlike in standard isoelectric focusing, is not a zero charge point of the protein under consideration but the point where EO and EP forces balance.

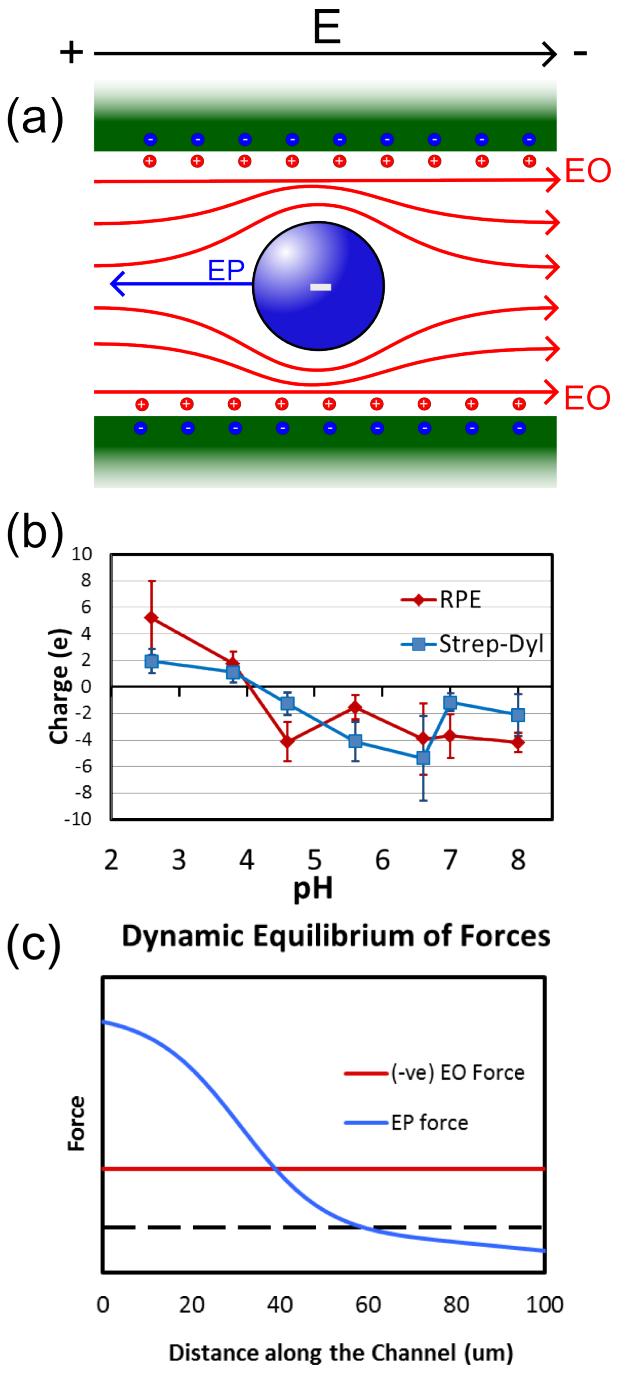

FIGURE 3.2-2: (a) Illustration of the trapping mechanism. Negative fixed charge is blue; positive free charge is red. (b) Zetasizer measurements of the relationship between the protein charge vs pH. The pH and conductivity of the buffers were as follows: pH 2.6 & 1.05 mS/cm; 3.8 & 1.75; 4.6 & 2.51; 5.6 & 3.59; 6.6 & 4.58; 7.0 & 4.87 (c) Illustration of the variation of electro-osmotic (EO) and electrophoretic (EP) forces on an RPE protein along the nanochannel. The electrophoretic force varies with distance along the channel due to the inherent charge-pH relationship of RPE. Focusing occurs at a point along the channel where the sum of EO and EP forces is zero, which is not at the standard PI point.

3.3 Methodology

3.3.1 Fabrication

The nanochannel device shown by the top-view schematic in Figure 3.3-3 was fabricated using standard techniques. The microchannels were photolithographically patterned using SU-8 photoresist and etched by deep reactive ion etching at the Australian National Fabrication Facility at the University of South Australia to a depth of 12.5 ± 0.5 μm. The SU-8 was removed by baking in air at 900 ^{o}C for 5 hrs. A variety of tapered and rectangular nanochannels connecting the microchannels were patterned by a second round of photolithography using AZ-1518 photoresist (Microchem, MA, USA). Note that only the rectangular nanochannels are studied here. Nanochannels were etched in a CF_4 plasma (9% of 250 sccm CF_4, 2% of 100 sccm O_2, 150W) in a March PX-250 plasma asher for a total of 12 min to a depth D = 85 ± 5 nm. The nanochannels were patterned to have a length L = 100 μm and a width W = 20 μm. After the etch process, through-holes were created at the ends of the microchannels using a dental sandblaster ("PrepStart Kit Air Abrasion Cavity Prep unit" and "Micro-Cab Plus Self Contained Dust Cabinet" Danville Materials, California, USA)[34][35]. After cleaning, the wafer was bonded to a blank fused silica wafer using a reverse RCA [15] procedure and annealed for 12 hrs at 1050 ^{o}C in air. Wafers were then cut into 7.5 mm wide chips that fit inside a custom made microscope adapter providing fluid and electrical connections during fluorescence microscopy. The inset in Figure 3.3-3 also illustrates a close up of the nanochannels with a cross-sectional vertical cut made perpendicular to the microchannels for clarity.

3.3.2 Experimental Conditions

Measurements of protein mobility vs pH were made using a Zetasizer (Malvern Instruments). Citric acid buffers of pH values between 2.6 to 7.0 were prepared with the conductivities between 1 - 4.87 mS/cm (details in the description of Figure 1b). It has been shown by Salgin et al. [36] that the variation in conductivity may affect the results of the zeta potential test, but our conductivity span is relatively small and should not affect the general trend of the plot. The buffers were prepared by mixing specific volumes of 0.1 M citric acid solution with 0.2 M disodium orthophosphate (Na_2HPO_4). RPE or Dyl-Strep was added into a buffer at 1.5 mg/ml and measured repeatedly (3 or 4 times). The protein was recovered and re-suspended in successive buffers using a

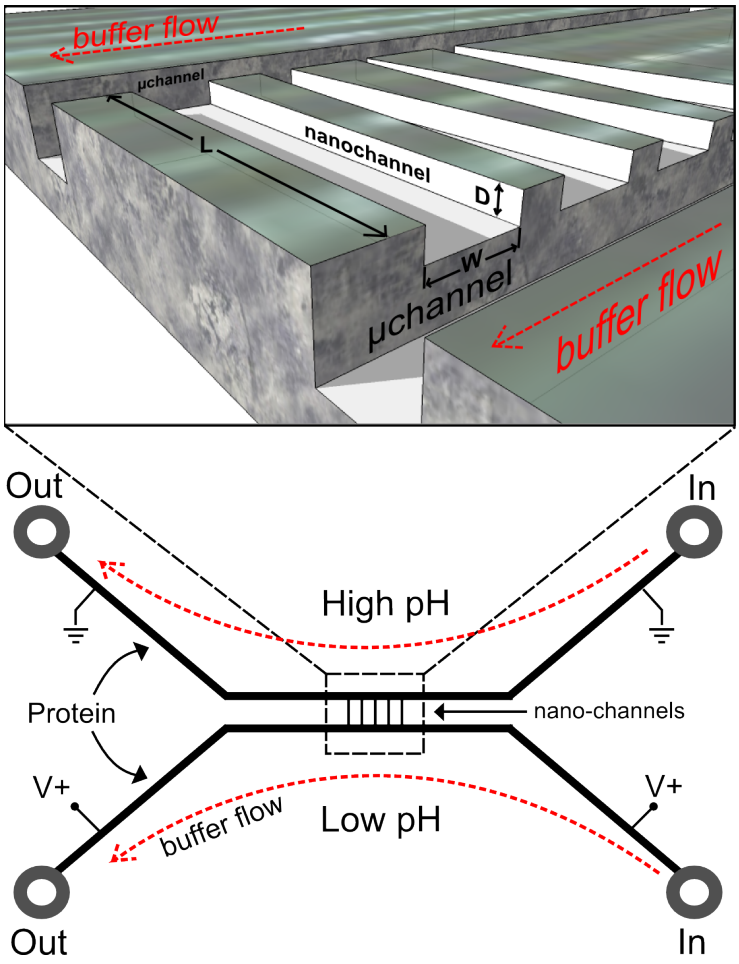

FIGURE 3.3-3: Schematic of the nanochannel device indicating the fluid flow direction (red dotted line) within each microchannel. The Inset shows the nanochannels with the top silica layer removed and a vertical slice taken to more clearly illustrate the geometry of the channels. Depth of microchannels is 12.5 ± 0.5 μm. Nanochannels are W = 20 μm wide, L = 100 μm long and D = 85 ± 5 nm deep.

10 kDa cut-off centrifugal. For on-chip focusing, new buffers were created in a similar manner (pH 2.6, 2.7, 3.6, 5.1, 5.8, 6.4, 7.2); however, in order to achieve matching conductivity required to eliminate conductivity gradients along the channel, de-ionized water and sodium chloride was added until each pH buffer reached 4.60 ± 0.02 mS/cm. Since protein is stored in a high salt buffer, even a small amount of it added to one buffer could raise the conductivity of one side, producing a conductivity gradient within the nanochannel. Therefore, an equal amount of concentrated protein (RPE or Dyl-Strep) was then added to buffers for both sides of the nanochannel. The final protein concentration of the RPE was 18 μg/ml. The final protein concentration of Dyl-Strep was 50 μg/ml. During the focusing experiments, each microchannel was continuously

supplied with a protein/buffer mixture of different pH values at 1000 nL/min using a Fluigent Fluiwell (France). A regulated power supply was connected to all four fluid ports. Positive electrodes were connected to both ends of the low pH channel and negative electrodes were connected to both ends of the high pH microchannel. An applied voltage of 0.4 V typically produced currents of 9.2 ± 0.8 nA. Between experiments channels were rinsed thoroughly with water and then each reservoir was rinsed with a buffer having a pH and conductivity matching that of the next experiment. Chips were occasionally cleaned by baking in air at 900 ^{o}C overnight. Fluorescence microscopy was used to quantify the focusing of the proteins. A mercury lamp with a standard filter set was used to excite RPE (peak absorption 565 nm, peak emission 573 nm) and Dyl-Strep (peak absorption 488 nm, peak emission 535 nm) within the nanochannel. A Nikon DS-U2 USB camera was used to capture the resulting fluorescence images. As the focus band intensified, the exposure time for the image was decreased to avoid detector saturation. This was later compensated for by using a multiplicative exposure factor during the analyses. The concentration enhancement (CE) factor (to be used henceforth to quantify the protein focusing) is defined as the nanochannel band intensity (I_{FOCUS}) divided by the high pH microchannel intensity (I_{Micro}) times the microchannel depth (D_{Micro}) divided by the nanochannel depth (D_{Nano}).

$$CE = \frac{I_{FOCUS}}{I_{Micro}} \frac{D_{Micro}}{D_{Nano}} \tag{3.5}$$

3.4 Results and Discussion

Figure 3.4-4b shows the results of Zetasizer measurements of protein charge vs pH. The general trend of the plot confirms that as pH of the buffer increases, the charge of both RPE and Dyl-Strep decreases. Figure 3.4-4(a) shows the concentration of RPE in the nanochannel by pH gradient electrofocusing with a 0.4 V bias applied across the electrodes, positive at the 2.6 pH buffer (left side) and negative at 6.4 pH buffer (right side). A bright focused band of RPE was observed which intensified and maintained a stable position for up to 10 min. Figure 3.4-5(a) and 3.4-5(b) show concentration enhancement and band width of RPE and Dyl-Strep using a pH span of 4.2 and a voltage of 0.4 V. RPE reaches an average CE of 385 (Figure 3.4-4) which corresponds to a concentration of 0.028 mM (6.8 mg/ml) at the focus band. Similarly, Dyl-Strep reaches a saturation CE of 107 which corresponds to 0.089mM (4.8 mg/ml) at the focus. Note that both reach a similar concentration in mg/ml, and so we tentatively attribute the lower intensity of Dyl-Strep to saturation of focusing due to protein

precipitation at high concentration focus bands which is common in cIEF [11]. The nonlinear saturation effect observed for the concentration enhancement of both RPE and Dyl-Strep may also be due to photon induced chemical damage (photo-bleaching) due to the exposure periods required for taking micrographs (<4 s), as well as self-quenching when fluorescent proteins are found in high concentrations. Finally we note that the observed values of CE for both proteins likely underestimate their true value since the proteins fluoresce less at acidic pH. This pH dependence has not been accounted for in the CE calculations.

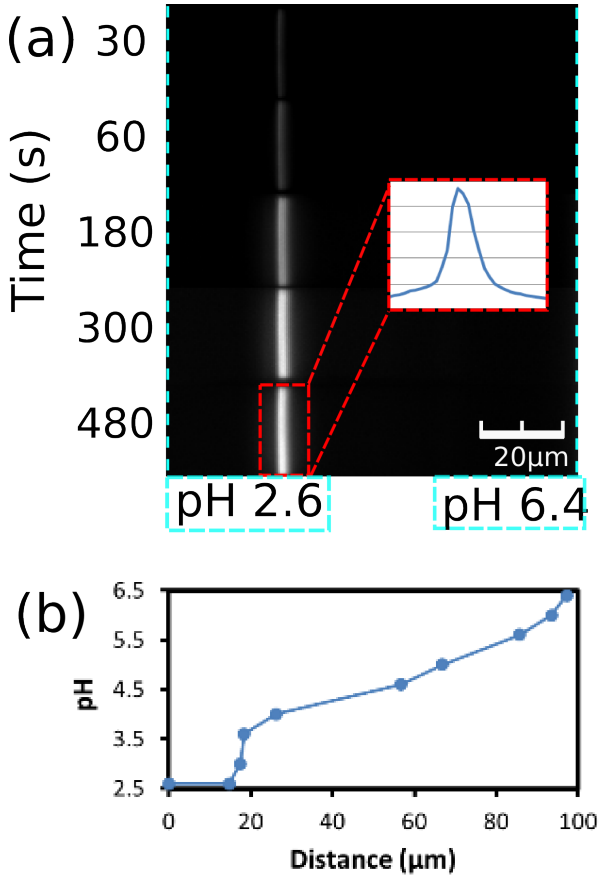

FIGURE 3.4-4: (a) Microscope image time series shows stable and increasing concentration enhancement (CE) of RPE bands. (b) pH gradient profile of the nanochannels at zero voltage bias found by fluorescein pH dependent fluorescence.

The gradient of the channel was tested within the nanochannel using Fluorescein at 0 volt bias. Fluorescene was carried through the nanochannel at a 1.5 mM concentration within citric acid buffer in the same manner to how the RPE and Dyl-Strep were delivered. Parameters of pressure and flow rate were kept as similar as possible in

order to match the conditions of protein focussing. However, voltage was not applied because fluorescein would exhibit focusing behaviour as well. Regardless, even limited to zero voltage bias, we get an impression of what the pH gradient within the channel may be prior to voltage applied.

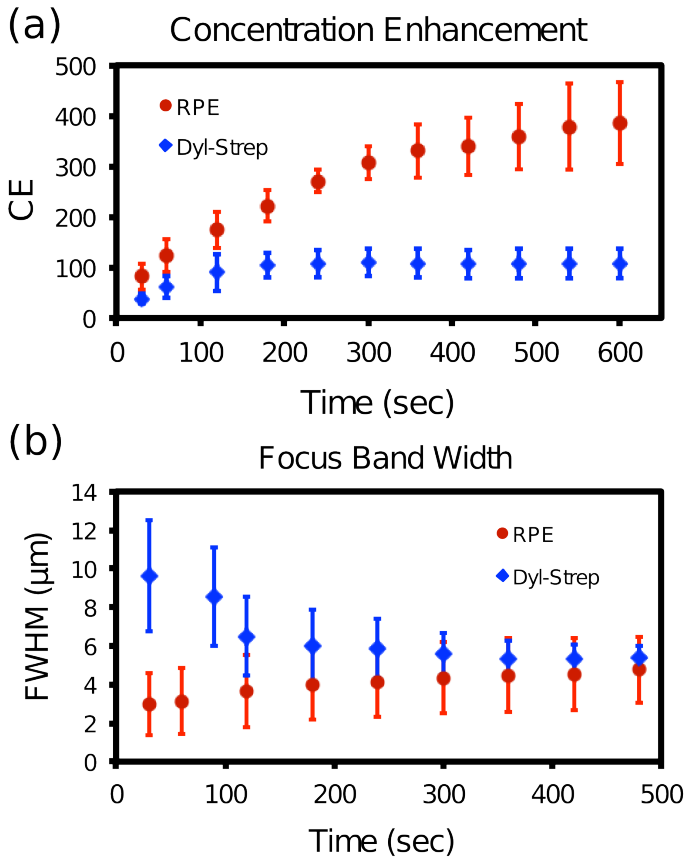

Figure 3.4-5: (a) CE versus time of RPE (red dots) and Dyl-Strep (blue diamonds) in separate experiments. (b) Full-width-half maximum measurement (averaged over 3 trials) approaches approximately 5 μm for both proteins.

Figure 3.4-5 shows that RPE and Dyl-Strep bands behaved differently. Dyl-Strep band widths decreased initially while RPE band increased initially, but both approached approximately 5 μm FWHM, which is relatively narrow compared to previously reported experiments with conductivity gradient electrofocusing [15]. Since the concentration of RPE, even in the peak, is still approximately 1000 times lower than the background electrolyte concentration (~30 mM), we do not expect the initial

RPE band broadening to be the result of ion substitution by the protein, as in plateau-mode isotachophoresis [7][8]. pH variations across the depth of the nanochannel as described by Bottenus [37] may contribute to the width of the band.

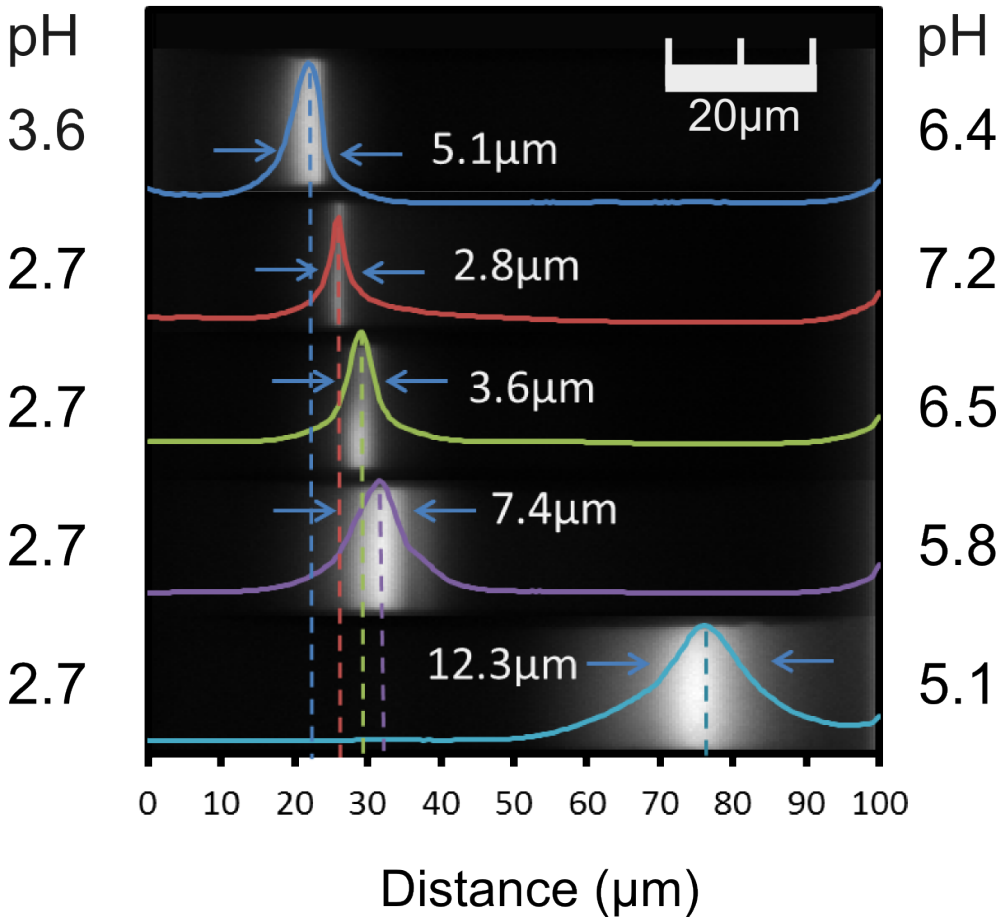

FIGURE 3.4-6: Fluorescence microscopy of RPE focusing using various pH values under 0.4 V bias for 300 sec. Note that peak intensities have been normalized. The superimposed line shapes of the focus bands indicate the respective peak widths and position dependence on pH buffer selection. The sharpness measured by the FWHM shows the narrowest band of 2.8 μm results from the widest pH span: 4.2 (pH 2.7 to 7.2). The width of the peaks steadily increases as the pH span is decreased. At the smallest pH span of 2.4 (pH 2.7 to 5.1) the FWHM is 12.3 μm. Note that when similar buffers were used (close to same pH buffer), no focusing could be observed at all.

Figure 3.4-6 shows that the RPE band depends on the buffer pH present in the reservoirs. The boundaries are kept constant by the continuous flow of buffers running in the microchannels. It is clear that focusing is sharpest when a large pH difference is used. This is indicated by the second band from the top of Figure 3.4-6 which spans 4.5 pH intervals (pH 2.7 to 7.2) and yields a focus band with a FWHM of 2.8 μm.

It is also evident that the focus band is broadest when the pH span is smallest, the bottom image of Figure 3.4-6 which shows a channel spanning only 2.4 intervals of pH (pH 2.7 to 5.1) yields a focus band FWHM of 12.3 m. The collection of superimposed plots in Figure 3.4-6 suggests that the RPE focuses at a similar pH point regardless of the selected pH boundaries. As pH boundaries are shifted, the focus point moves in a predictable way to where we would expect the focus pH to be located within the new pH gradient

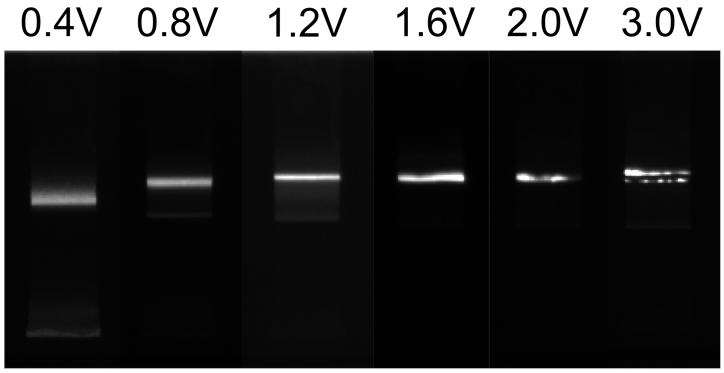

Figure 3.4-7: Fluorescence images showing quality of focusing at various bias voltages after 300 seconds of focusing. RPE focuses into a uniform band at lower voltages below 1.6V, but at higher voltages, the band becomes distorted and non-uniform. At 3.0V the band becomes discontinuous.

Figure 3.4-7 demonstrates that protein focusing also depended on the voltage applied at the electrodes. Increasing the voltage to 1.2 V generally resulted in a narrower band and faster focusing. The focus band biased at 1.6 V loses some of its uniformity and above 2 V the band began to break up. While the intensity continued to increase with voltage, the fluorescent band began to form localized high-intensity points. In addition, the band tended to split apart into multiple bands making the focusing quality inferior. This breakup may be a result of possible precipitation effects due to high concentration of proteins at a sharp focus. Another possible cause of the band break-up is the increasing Peclet number. Higher voltages drive faster convection, which may overcome the ability of the protein to diffusively average the frustrated flow profile leading to leaks in an otherwise stable electrokinetic trap. We also considered the possibility of Joule heating interfering with the focusing, but since we observed currents of only about 100 μA, the 3 V bias could only result in power dissipation of 300 μW. This relatively small amount of heat would be rapidly conducted away by the thermally conductive single crystal silicon substrate (150 W/K/m thermal conductivity). The

temperature rise attributable to Joule heating would be limited to less than a 1/100th of a °K, an insignificant factor compared to the other possible causes of band break-up mentioned earlier.

Figure 3.4-8 shows the effect of varying the voltage bias on the CE increase rate of RPE. It is clear from the plot that the higher the voltage, the quicker the rate with which the the concentration enhancement increases. However, from Figure 3.4-8, it is not clear from whether the CE plateau will be approaching the same value for each voltage. 1.6 V bias exhibits the fastest CE growth rate, matching that of 2.0V. Voltages beneath 1.6 exhibit predictably slower CE growth.

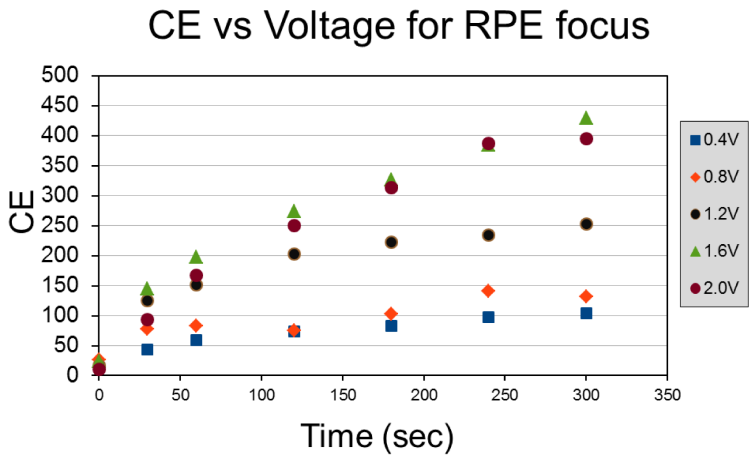

FIGURE 3.4-8: Plot of concentration enhancement of R-phycoerythrin using a series of bias voltages

We believe that the nanoscale height of the channel is the critical, enabling feature of our method. The small channel depth (85 ± 5 nm) allows protein molecules to diffuse rapidly from top to bottom surfaces, giving a Peclet number of less than unity, effectively averaging the three-dimensional fluid flow velocity and electric field vectors into one dimension where stability is much easier to achieve. Finally, we reiterate that the observed trapping is attributed to pH gradient focusing and unlikely to be the result of electric field gradient trapping due to either nanochannel ion concentration polarization (ICP) or differences in bulk buffer conductivity. The ICP mechanism relies on the selective transport of ions through a nanochannel using identical buffers and produces trapping adjacent to micro-nano-interfaces. In this work we have not observed any trapping in our microchannels or very near the nanochannel ends, nor do we observe any focusing when the two buffers in the microchannels are identical

(or very similar). We also emphasize that our buffers had matched bulk conductivity and that trapping is not observed without a significant pH gradient. Further work, especially substantial modelling is required to more fully understand the interaction of chemical, electrical and fluid effects that result in this protein focusing phenomena.

3.5 Conclusion

In this work, pH gradient electrofocusing along a nanochannel has been demonstrated for the first time. As an example, RPE and Dyl-Strep were focused using a range of citric acid pH buffers as boundaries of the nanochannel. The optimal quality focus was achieved using a pH span of 2.7-7.2 and a bias voltage of 0.4 V. RPE and Dyl-Strep both approached focus bands widths of around 5 μm with concentration enhancement (CE) factors of 385 and 107 respectively. The technique may be, in principle, capable of achieving multiple protein separation and concentration simultaneously.

3.6 Acknowledgement

This work was supported by the Australian Research Council (DP110102207). Microchannel etching was performed at the University of South Australia node of the Australian National Fabrication Facility, established under the NCRIS scheme.

References

[1] Donald J. Rose and James W. Jorgenson. Fraction collector for capillary zone electrophoresis. *Journal of Chromatography A*, 438(0):23–34, 1988. 60

[2] P.H. O'Farrell. High resolution two-dimensional electrophoresis of proteins. *Journal of Biological Chemistry*, 250(10):4007–4021, 1975. 60

[3] Fred E. Regnier. *Contemporary Topics in Analytical and Clinical Chemistry*. Springer US, 1977. 60

[4] Thomas L. Chester. Recent developments in high-performance liquid chromatography stationary phases. *Analytical chemistry*, 85(2):579–589, 2012. 60

[5] P. Grosso, S. Carrara, C. Stagni, and L. Benini. A low-cost point-of-care system for parallel elisa essays. In *Biomedical Circuits and Systems Conference, 2009. BioCAS 2009. IEEE*, pages 269–272, 2009. 60

[6] Anas El-Aneed, Aljandro Cohen, and Joseph Banoub. Mass spectrometry, review of the basics: Electrospray, maldi, and commonly used mass analyzers. *Applied Spectroscopy Reviews*, 44(3):210–230, 2009. 60

[7] Alexandre Persat, Lewis A. Marshall, and Juan G. Santiago. Purification of nucleic acids from whole blood using isotachophoresis. *Analytical chemistry*, 81(22):9507–9511, 2009. 60, 70

[8] G. Garcia-Schwarz, A. Rogacs, S. S. Bahga, and J. G. Santiago. On-chip isotachophoresis for separation of ions and purification of nucleic acids. *Journal of Visualized Experiments*, 61:e3890, 2012. 60, 70

[9] E. A. Strychalski, A. C. Henry, and D. Ross. Microfluidic analysis of complex samples with minimal sample preparation using gradient elution moving boundary electrophoresis. *Analytical chemistry*, 81(24):10201–7, 2009. 60

[10] David Ross. Step width, spacing, and resolution in gradient elution moving boundary electrophoresis. part 1. theory and comparison with zone electrophoresis. *Electrophoresis*, 31(22):3650–3657, 2010. 60

[11] Thomas J. Pritchett. Capillary isoelectric focusing of proteins. *Electrophoresis*, 17(7):1195–1201, 1996. 60, 68

[12] Sung Jae Kim, Yong-Ak Song, and Jongyoon Han. Nanofluidic concentration devices for biomolecules utilizing ion concentration polarization: theory, fabrication, and applications. *Chemical Society Reviews*, 39(3):912–922, 2010. 60

[13] Ying-Chih Wang, Anna L. Stevens, and Jongyoon Han. Million-fold preconcentration of proteins and peptides by nanofluidic filter. *Analytical chemistry*, 77(14):4293–4299, 2005. 60

[14] Thomas A. Zangle, Ali Mani, and Juan G. Santiago. Theory and experiments of concentration polarization and ion focusing at microchannel and nanochannel interfaces. *Chemical Society Reviews*, 39(3):1014–1035, 2010. 60

[15] David W. Inglis, Ewa M. Goldys, and Nils P. Calander. Simultaneous concentration and separation of proteins in a nanochannel. *Angewandte Chemie International Edition*, 50(33):7546–7550, 2011. 60, 65, 69

[16] P.H. O'Farrell. Separation techniques based on the opposition of two counteracting forces to produce a dynamic equilibrium. *Science*, 227(4694):1586–1589, 1985. 60

[17] CB Raj. Protein purification by counteracting chromatographic electrophoresis: quantitative focusing limits and protein selection at the interface. *Journal of Biochemistry and Biophysics Methods*, 28(3):161–172, 1994. 60

[18] Wendy S. Koegler and Cornelius F. Ivory. Focusing proteins in an electric field gradient. *Journal of Chromatography A*, 726(1-2):229–236, 1996. 60

[19] Dzmitry Hlushkou, Robbyn K. Perdue, Rahul Dhopeshwarkar, Richard M. Crooks, and Ulrich Tallarek. Electric field gradient focusing in microchannels with embedded bipolar electrode. *Lab on a Chip*, 9(13):1903–1913, 2009. 60

[20] Z. Huang and C. F. Ivory. Digitally controlled electrophoretic focusing. *Analytical chemistry*, 71(8):1628–1632, 1999. 60

[21] David Ross and Laurie E. Locascio. Microfluidic temperature gradient focusing. *Analytical chemistry*, 74(11):2556–2564, 2002. 60

[22] G Tang and C Yang. *Temperature Gradient Focusing*. Springer-Verlag Berlin Heidelberg, 2008. 60

[23] A. Kolin. Separation and concentration of proteins in a ph field combined with an electric field. *The Journal of Chemical Physics*, 22(9):1628–1629, 1954. 60

[24] P.G. Righetti. *Immobilized pH gradients: theory and methodology*. Elsevier Science Publishers B.V. (Biomedical Division), Amsterdam, 1990. 60

[25] Konstantin Chingin, Juan Astorga-Wells, Mohammad Pirmoradian Najafabadi, Thorleif Lavold, and Roman A. Zubarev. Separation of polypeptides by isoelectric point focusing in electrospray-friendly solution using a multiple-junction capillary fractionator. *Analytical chemistry*, 84(15):6856–6862, 2012. 61

[26] Renato Millioni, Serena Tolin, Lucia Puricelli, Stefano Sbrignadello, Gian Paolo Fadini, Paolo Tessari, and Giorgio Arrigoni. High abundance proteins depletion vs low abundance proteins enrichment: Comparison of methods to reduce the plasma proteome complexity. *PLoS ONE*, 6(5):e19603, 2011. 61

[27] Veronika Polaskova, Amit Kapur, Alamgir Khan, Mark P. Molloy, and Mark S. Baker. High-abundance protein depletion: Comparison of methods for human plasma biomarker discovery. *Electrophoresis*, 31(3):471–482, 2010. 61

[28] M. Vazquez, G. McKinley, L. Mitnik, S. Desmarais, P. Matsudaira, and D. Ehrlich. Electrophoretic injection within microdevices. *Analytical chemistry*, 74(9):1952–61, 2002. 61

[29] Vishal Tandon, Sharath K. Bhagavatula, Wyatt C. Nelson, and Brian J. Kirby. Zeta potential and electroosmotic mobility in microfluidic devices fabricated from hydrophobic polymers: 1. the origins of charge. *Electrophoresis*, 29(5):1092–1101, 2008. 61

[30] H-C Chang and LY Yeo. *Electrokinetically Driven Microfluidics and Nanofluidics*. Cambridge University Press, New York, 2010. 61, 62

[31] Wei-Lun Hsu, David W. Inglis, Michael A. Startsev, Ewa M. Goldys, Malcolm R. Davidson, and Dalton J.E. Harvie. Isoelectric focusing in a silica nanofluidic channel: Effects of electromigration and electroosmosis. *Analytical Chemistry*, 86(17):8711–8718, 2014. PMID: 25098739. 62

[32] Jean Berthier and Pascal Silberzan. *Microfluidics for Biotechnology*. Artech House, Norwood, M.A., 2006. 62

[33] H.C. Berg. *Random Walks in Biology*. Princeton University Press, Chichester, 1993. 62

[34] H. Wensink. *Fabrication of microstructures by powder blasting*. PhD thesis, University of Twente, Enschede, February 2002. 65

[35] H. Wensink, H. V. Jansen, J. W. Berenschot, and M. C. Elwenspoek. Mask materials for powder blasting. *Journal of micromechanics and microengineering*, 10(2):175–180, June 2000. 65

[36] Sema Salgin, Ugur Salgin, and Seda Bahadir. Zeta potentials and isoelectric points of biomolecules: The effects of ion types and ionic strengths. *International Journal of Electrochemical Science*, 7:12415–12431, 2012. 65

[37] Danny Bottenus, Youn-Jin Oh, Sang M. Han, and Cornelius F. Ivory. Experimentally and theoretically observed native ph shifts in a nanochannel array. *Lab on a Chip*, 9(2):219–231, 2009. 70

4

Nanochannel Conductivity Gradient Electrofocusing

Abstract. Conductivity gradient electrophoresis was used to trap 150 bp Bacillus cereus DNA within a nanochannel device. The trapping concentration and band integrity/sharpness was characterized at various microchannel supply concentrations and bias voltages over a span of 300 seconds. Bias voltage variation indicated that higher voltages resulted in faster DNA accumulation within the trap. The simultaneous separation and concentration of DNA and protein was demonstrated by introducing Bacillus cereus DNA and protein R-phycoerythrin (RPE) together into the device. Separation and concentration was observed yielding band widths of 22.6 μm and 4.5 μm for DNA and RPE respectively. The peak separation between DNA and RPE was 15.0 μm. The peak separation resolution quality was quantified as $R_s = 1.1$ with slight overlap, but with distinct observable peaks.

4.1 Introduction

Nanochannel electrofocusing has the potential to improve the state of the art of DNA separation and sequencing, and offers applications in biotechnology and medicine[1].

Most conventional methods of DNA electrophoresis require either the use of a gel or a concentrated solution of hydrophilic polymers as a medium for separation in which DNA molecules migrate due to the force from an electric field.

Fractionation of DNA is an essential technique in molecular biology for measuring size and mobility distributions of DNA (as well as protein-DNA interactions) often as a precursor to further experiments. There are limitations to conventional techniques such as standard gel electrophoresis, wherein separation is typically possible for DNA molecules up to around 40 kbases (larger DNA molecules experience mobility independent of size due to stretching of DNA). Separating larger DNA such as chromosomes takes days to weeks using pulsed-field gel electrophoresis [2]. Capillary electrophoresis (CE) has been known to separate million-base-pair sized DNA within 10 minutes [3]. However, CE usually involves high applied voltage (100 V - 30 KV) which causes an inevitable Joule heating effect, creating temperature gradients in the transverse and longitudinal directions inside the capillaries [4]. Higher voltages result in greatest efficiency in terms of separation time, but excess Joule heating can cause bubble formation, denaturation of analytes, and breakdown of devices [5]. Also, within capillaries, DNA aggregation may occur due to electrohydrodynamic instabilities [6]. Nanofluidic devices are often created with "obstacle course" geometries as an analogue to gel-capillaries to impede motion of large molecules within the nanodevice. Other DNA separation techniques were investigated and assessed by Lin et al. [7]. Methods of entropic trapping of DNA were demonstrated by Turner [8] and Han [9], which enables the trapping and separation of large DNA molecules (5000-160,000 base pairs) according to their lengths. Hammond [10] demonstrated a Brownian ratcheting mechanism for DNA fractionation within an interdigitated nanofluidic electrode array. Huang [11] demonstrated a microfluidic DNA sorting mechanism analogous to pulsed-field gel electrophoresis using asymmetric pulsed fields applied to a continuous-flow of analyte which then separated according to the DNA molecular masses much like a prism deflects light of varying wavelengths. These mechanisms rely on steric interactions for separation. However, at the nanoscale, it is possible to leverage the electrostatic coupling within double layer length scales in addition to these steric effects. Current data acquired for electrophoresis of 1-100 base-pair Oligonucleotides in depths of 40 nm, 100 nm [12] suggests that DNA undergoing electrophoresis experiences a complex interplay between steric interactions, ionic screening of analytes, ionic strength of the bulk electrolyte, the EDL wall effects and the applied electric field. In the realm of nanofluidic electrofocusing and separation, there is still much to be explored. The work presented in the previous chapter examined the trapping of proteins as a result

of the interplay between the counteracting electroosmotic and electrophoretic forces that were generated by an induced pH gradient within the nanochannel device. In this chapter, we create a trapping condition by inducing a conductivity gradient within the nanochannel as demonstrated by Inglis et al. [13] in order to separate genomic DNA from proteins simultaneously within the nanochannel device.

4.2 Methodology

4.2.1 Device Fabrication

A silicon wafer with a 50 nm thick oxide grown on the active surface was used as a substrates to fabricate the devices. 6 on-chip devices were fabricated per silicon wafer using a two phase photolithography procedure. The first phase of photolithography exposures patterned the microchannels and the second phase patterned the nanochannels. After developing and etching, the mask needed only to be rotated 180 degrees in order to expose the second pattern over top of the first. The detailed procedure can be found in Appendix A.1 - A.3.4.

4.2.2 DNA Shearing

Long strands of DNA can cause problems within the nanofluidic device. The DNA can cause clogging and may simply not fit inside the nanofluidic channels if it is agglomerated together.

Bacillus cereus DNA was fragmented via hydrodynamic shearing using a Covaris E220 ultrasonicator. Appendix A.4.1 shows the parameters of the shearing procedure. The DNA samples were aliquoted into 130 μl volumes and set inside the device for a 600s interval (instead of the 430 seconds stated in the default Covaris protocol) targeting a final length of 150 base pairs. The size was confirmed via Agilent Bioanalyzer 2100 to be a distribution spanning between 50 - 250 bp and peaking at 150 bp (Appendix A.4.1).

4.2.3 Experimental Conditions

During the focusing experiments, each microchannel was continuously supplied with a DNA/buffer or protein/buffer mixture having dissimilar salt concentrations (conductivity) at 1000 nL/min through a pressured capillary delivery system (Fluigent Fluiwell pressure controller)(Figure 4.2-1). A regulated power supply was connected to all four

fluid ports. Positive electrodes were connected to both ends of the high conductivity channel and negative (ground) electrodes were connected to both ends of the low conductivity channel microchannel. An applied voltage of 0.4 V typically produced currents of 7 ± 2 nA. Between experiments, channels were rinsed thoroughly with deionized water and then each reservoir was rinsed with a phosphate buffer having a conductivity matching that of the next experiment. When chips began clogging, they were thoroughly cleaned by running deionized water through the fluid ports for 30 minutes, followed by 1 M NaOH for 30 minutes to remove any protein or DNA agglomerated to the surfaces and then again with deionized water for 30 minutes to refresh the silanol surface groups within the channel. Some of the residual clogging could be cleaned off by baking in air at 900 ^{o}C overnight. Over night and between experiments, the chips were stored in individual vials containing deionized water in order to avoid drying, and particulate contamination. Eventually, after 2 or 3 weeks of daily use, the chips would begin to fail despite the cleaning efforts and a new chip would have to be used instead.

4.2.4 Fluorescence Imaging

A Leica DM IRB inverted fluorescence microscope was used to quantify the trapping of DNA. A mercury lamp with a standard filter set was used to excite DNA labelled with SYBR Green (peak excitation 497 nm, peak emission 520 nm) and RPE (peak excitation 565 nm, peak emission 578 nm) within the nanochannel. A Nikon DS-U2 USB camera was used to capture the resulting fluorescence images. Between images, the shutters were closed to minimize photo-bleaching effects. As in Chapter 3, the exposure time of for the image was decreased as the band focus intensity increased to avoid detector saturation. Since image brightness intensity increased linearly with increasing exposure time, our fluorescence intensity analysis incorporated a multiplicative factor that accounts for the varying exposure times so that a relative measure of fluorescence intensity (which we called the concentration enhancement (CE)) could be calculated. The concentration enhancement (CE) factor was used to quantify the DNA and RPE focusing and is defined as the nanochannel band intensity (I_{FOCUS}) divided by the DNA or protein containing microchannel intensity (I_{Micro}) times the microchannel depth (D_{Micro}) divided by the nanochannel depth (D_{Nano}).

$$CE = \frac{I_{FOCUS}}{I_{Micro}} \frac{D_{Micro}}{D_{Nano}} \tag{4.1}$$

4.2.5 The Device

Figure 4.2-1 shows the device geometry from the top view, indicating the buffer flow in dotted red arrows, the location of the nanochannels perpendicular to the microchannels which carry the supply buffers which fix the conductivity values at the ends of the nanochannels and a close-up inset showing an isometric view of the nanochannel geometry. The length of the rectangular nanochannels used in this study was 100 μm, the width was 20 μm and the depth was 85 $\pm$ 5 nm. Since the silicon substrate carries a negative surface charge, the electro osmosis force (EO) acts to push the bulk flow within the nanochannels from the high conductivity end to the low conductivity end. Since DNA and RPE are negatively charged, the electrophoresis (EP) force tends to push the molecules from the low conductivity end towards the high conductivity end.

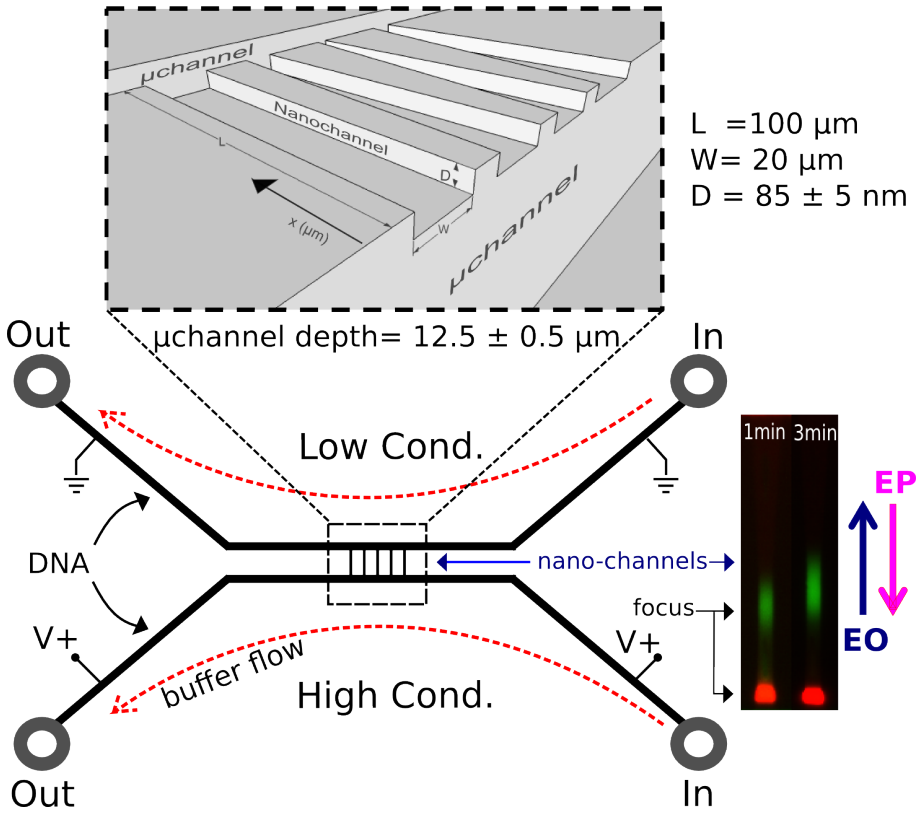

Figure 4.2-1: Schematic of the conductivity gradient nanochannel focusing on silicon chip device. The length of the nanochannels is L = 100 μm, the width is W = 20 μm and the depth is D = 85 $\pm$ 5 nm. The microchannel depth is 12.5 $\pm$ 0.5 μm. Electroosmosis (EO) force acts from the high conductivity buffer with the positive electrodes toward the low conductivity buffer end with the ground electrode. Electrophoresis (EP) force acts from the low conductivity buffer end towards the high conductivity buffer end of the nanochannel.

4.2.6 Inducing the Conductivity Gradient

The conductivity gradient method of molecular trapping used in this chapter differs slightly from the pH gradient method described in chapter 3. In chapter 3 we took great care to eliminate any conductivity gradient by measuring and adjusting the conductivity values by adding appropriate amounts of NaCl such that citric acid buffer at either side of the nanochannel had an equivalent conductivity. In this chapter, standard phosphate buffered saline solution at pH 7.0 was used at both ends of the of the nanochannel and the conductivity was varied. For the high conductivity end, salt was added to a 1x phosphate buffer to result in a total of 241 mM NaCl (with a conductivity of 42.2 mS/cm). For the low conductivity end, a 1x phosphate buffer was diluted to a 0.1x concentration to yield a 12 mM NaCl (with a conductivity of 2.4 mS/cm). This 20 fold difference in conductivity at either end of the channel resulted in a gradient throughout the channel that resulted in molecular traps at the position where counteracting electroosmosis and electrophoresis forces on a molecule were equal. The conductivity at the 12 mM NaCl anode end should not be made significantly lower since buffer pH would be difficult to control and the properties of proteins and DNA may become altered at exceedingly low salt concentrations.

Figure 4.2-2 illustrates the relationship between the counteracting EO and EP forces. The cyan line in 4.2-2(a) shows the EP force variation along the length of the channel, starting high in the low salt concentration microchannel (high resistance, high electric field) and decreasing as a negatively charged particle travels toward the the high salt concentration end of the nanochannel until it reaches the high salt concentration microchannel (low resistance, low electric field). At some position along the channel, the EP line crosses the blue EO line which is approximated to be constant along the nanochannel. It should be noted that if EO dominates EP, the conductivity gradient will become very steep and be located at the very end of the nanochannel. Under such a condition, both focus bands will be compressed together near that edge. It is therefore advantageous to tune the conductivites of either side of the channel such that EO and EP are optimal for focus band separation. Also, minor adjustments to the location of the focus bands can be induced using a gentle pressure counterflow. Figure 4.2-2(b) illustrates how the bulk Stokes flow caused by the motion of the sheath of ions within the double layer changes along the channel. Since the local electric field tends to force the positive ions in the double layer at higher velocity closer to the low salt concentration end, we might expect the EO to change similarly to EP, but due to mass conservation, the bulk fluid motion at any part of the nanochannel must be equal

to any other part of the nanochannel. At the high electric field end of the nanochannel, the electroosmosis is higher, but the bulk flow in the center of the channel depth experiences a counter flow. The 4.2-2 is exaggerated to illustrate this concept, but in reality, these flows are less significant and do not greatly contribute to band broadening since the diffusion of particles between the walls of the nanochannel is faster than the convection flow as indicated by the low Peclet number[14] (see discussion in chapter 3).

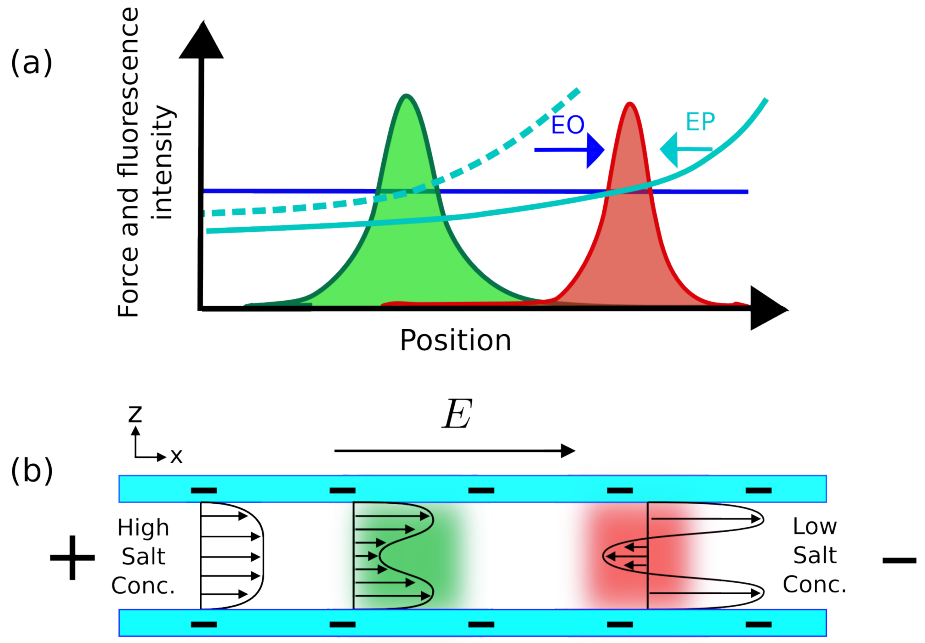

Figure 4.2-2: (a) illustration of the counteracting electroosmotic force (EO - blue) and electrophoretic force (EP - cyan) along the length of the nanochannel. EO is approximated as constant due to the conservation of mass condition, EP changes according to the local electric field which is dependent on the local salt concentration. (b) Illustration of EO force through the depth of the nanochannel (side view). The local electric field will cause the sheath of positive ions within the double layer along the wall to experience more EO force, but the bulk flow through out the length of the channel must remain constant so the central vectors compensate by producing a slight counter flow. The significance of this is exagerated in the image, but serves to explain the approximation of constant electroosmotic flow.

4.3 Discussion

4.3.1 DNA Concentration

In order to quantify the performance of 150 bp Bacillus cereus DNA alone within a conductivity gradient focusing scheme, DNA labeled with SYBR green was introduced to the low conductivity phosphate buffer microchannel at concentrations of 100 ng/ml, 200 ng/ml, 300 ng/ml, 600 ng/ml, 900 ng/ml, and 1200 ng/ml. A 4 V bias voltage was applied for 300 seconds while fluorescence images were captured at 60 second intervals.

Figure 4.3-3(a) shows sheared Bacillus cereus DNA concentration enhancement (CE) factors for various DNA injection concentrations over time. 100 ng/ml and 200 ng/ml DNA concentrations resulted in CE values at around 2300-2800, 600 ng/ml DNA concentration resulted in a slower increase in CE over time appearing to plateau at around 250s at a CE = 5500. 300 ng/ml proved to have a CE = 9000 peaking at 250s, which was higher than the 600 ng/ml concentration trial which came to a steady peak at CE = 5500 at 250s. 900 ng/ml performed similarly to the 300 ng/ml trial, but appeared to be increasing beyond 250s. The plateauing effect occurring at concentrations greater than 300 ng/ml might be due to electrostatic repulsion of the negatively charged DNA molecules when highly concentrated. This assumption is supported by the band width measurement in Figure 4.3-3(d) showing the full width half max band measurements over time during focusing. 100 ng/ml concentrations achieved relatively stable FWHM values of as little as 4 μm, while 900 ng/ml had a width steadily increasing to upwards of 12 um within the channel. 300 ng/ml also increased from 8 - 11 μm. Since CE measure the peak intensity values at the trapping location, it does not measure the total DNA in the band attributed to widening of the band. Therefore, the plateauing effect should not be mistaken as a cessation of DNA accumulation, but rather considered as the moment in the focusing progress where band fluorescence *peak* intensity plateaus. Another possible contribution for the apparent peak saturation is fluorescence photo-bleaching [15]. Since the act of taking a fluorescence image requires that the filter be open for a duration of 5-10 seconds, this could cause noticeable attenuation in the signal.

The peak DNA concentration at the trap can be calculated by applying the CE factor back on the original injection concentration as shown in Figure 4.3-3(b). It elucidates some of the unpredictable CE performance curves in (a) and verifies that despite the apparently anomalously high CE value for 300 ng/ml injection, the concentrations at the peak are still predictably increasing with increased injection concentrations. Figure 4.3-3(f) is a vertical slice of the data in (b) at 300s, showing that the DNA trap

concentration tends to steadily increase with the increasing injection concentration. The microchannel containing the injected DNA concentrations was also measured in brightness to confirm that the injection concentration values indeed correlated with brightness (figure 4.3-3(e)). A linear relationship was expected. Figure 4.3-3(c) shows the peak positions of the DNA band. With the exception of the 100 ng/ml trial, all trials tended to approach a focus peak at about 84 μm along the nanochannel (away from the high salt end).

Figure 4.3-4(a) shows the CE vs time progression for Bacillus cereus DNA supplied from the microchannels at 300 ng/ml. The rate of CE increase tends to be faster with higher voltage bias settings. An applied electric potential of 1 V achieves a CE = 580 within 300 seconds, 2 V achieves a CE = 2200, 3 V achieves a CE = 4300, 4 V achieves a CE = 5800, 6 V achieves a CE = 15400, and 8 V achieves a CE = 19500. Figure 4.3-4(b) plots the 300s data of CE vs bias voltage showing a nearly linear increase in CE up to 4 V bias values and then increasing at a faster rate at voltages of 6 V and 8 V. Figure 4.3-4(c) shows the band widths at 300 seconds. The band width of DNA seems to get slightly sharper at higher voltages, achieving the lowest width of 5.9 μm at 4 V and increasing slightly to 6.9 μm at 6 V and 8 V Figure 4.3-4(d) shows the position of the DNA band peak at 300 seconds for each voltage bias setting. Peak position tends to be centred around 85 μm regardless of the voltage bias.

4.3.2 RPE and DNA Separation

The conductivity gradient technique was used to demonstrate simultaneous concentration and separation of DNA and R-phycoerythrin (RPE). Bacillus cereus DNA was introduced to the low conductivity phosphate buffer microchannel at a concentration of 30 μg/ml. RPE was introduced to the high conductivity phosphate buffer microchannel at a concentration of 18 μg/ml. The DNA and RPE were introduced at opposite channels in order to limit the increase of conductivity in the low conductivity buffer and also to allow accurate measurement of the microchannel fluorescence level which is needed in order to quantify the concentration enhancement. The flow was set through the microchannels at 1000 nL/minute in order to ensure a constantly refreshed supply of analytes and buffer. In order to capture fluorescence emissions of SYBR GREEN labeled DNA (520 nm wavelength) and RPE (578 nm wavelength), the fluorescence microscope filtration cube was alternated to pass the appropriate wavelength such that

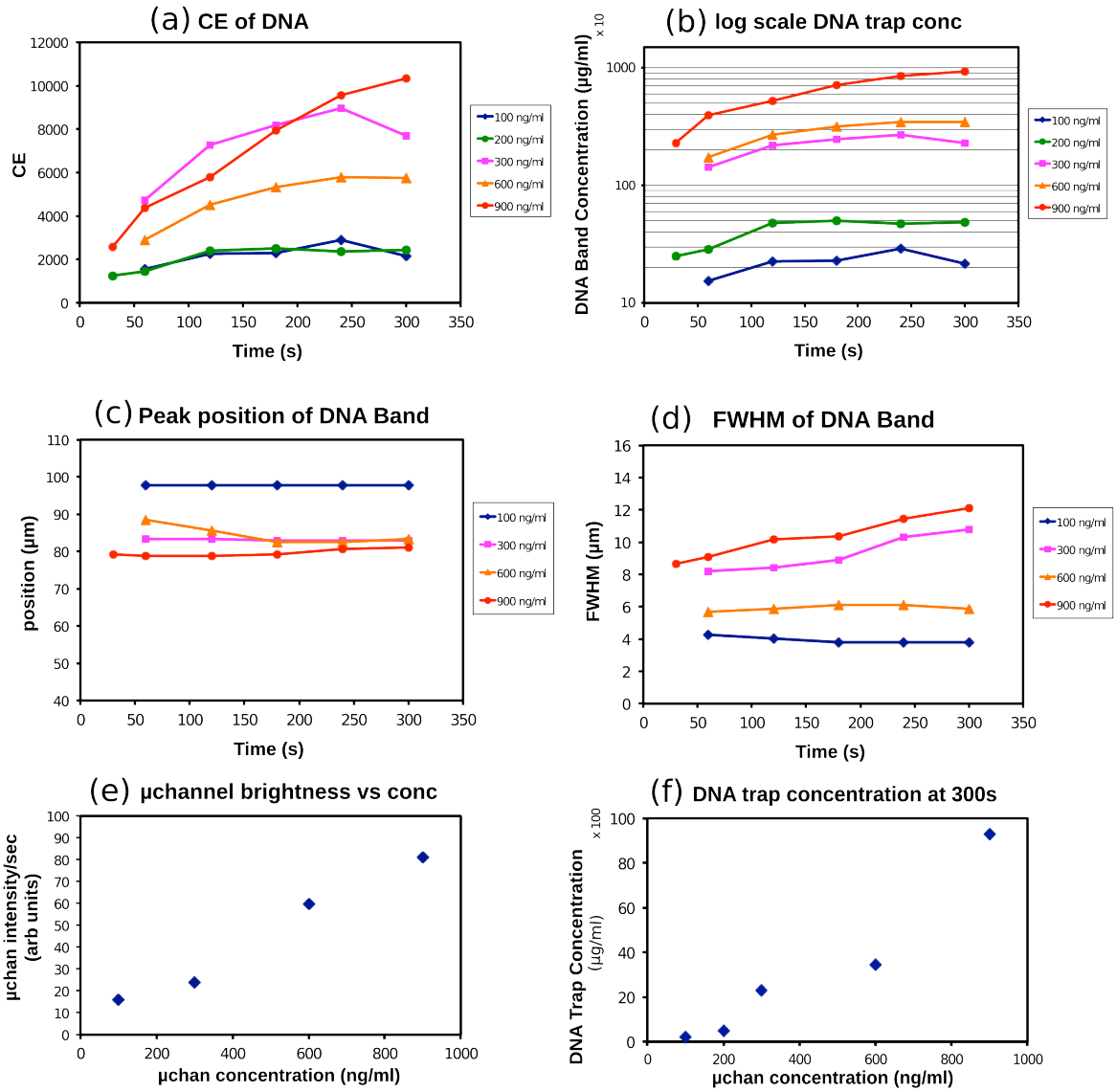

FIGURE 4.3-3: (a) Concentration enhancement over time for various microchannel (bulk) concentrations. (b) logarithmic scale of total DNA concentration at the focus band position of DNA within the nanochannel. (c) Band positions for various microchannel concentrations over time. (d) Width of bands (FWHM) for various microchannel DNA concentrations. (e) Brightness of microchannel when flowing different concentrations of DNA (per second of exposure). (f) Nanochannel DNA trap concentrations at 300 seconds for different microchannel concentrations.

the fluorescence of DNA and RPE can be captured independently. Appendix A.8 describes the filters used in the DM-IRB inverted microscope. The images were taken 30 seconds apart, allowing time to switch the filters and for the camera to capture the

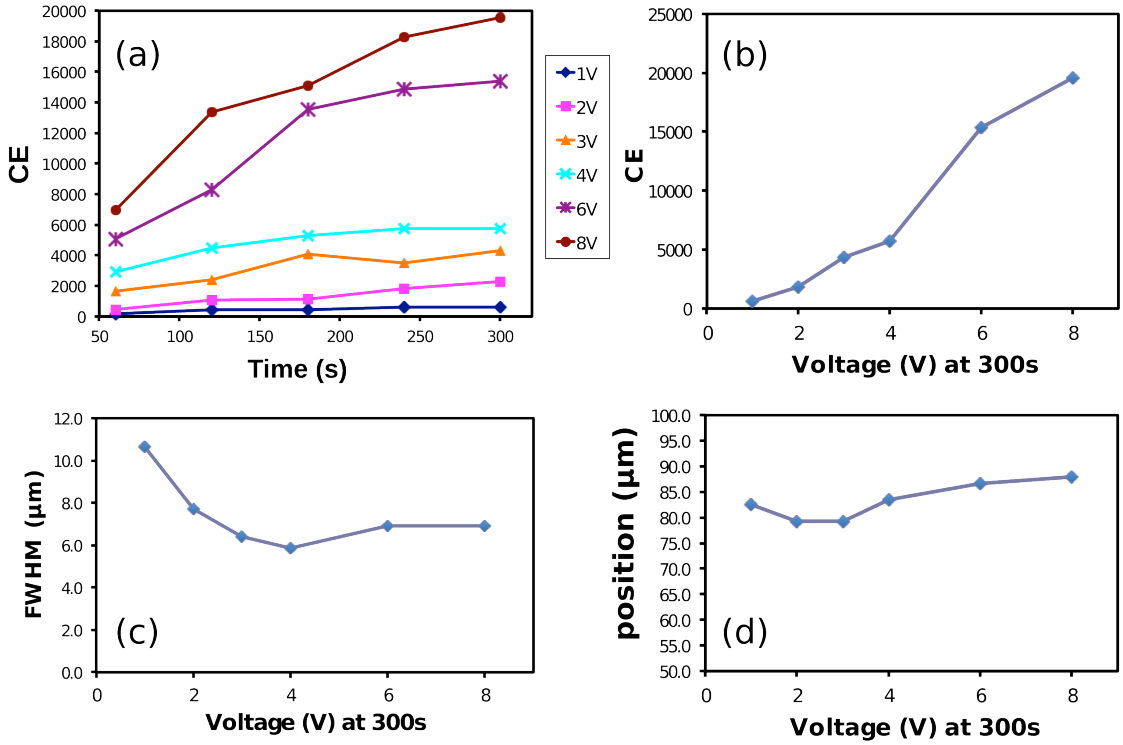

Figure 4.3-4: (a) DNA concentration enhancement (CE) over time of different voltage biases. The microchannel injection concentration was 300 ng/ml. (b) CE of DNA vs voltage bias at 300s. (c) The width of the DNA focus band at 300s for different voltage biases. (d) Peak position of DNA band at various bias voltages.

image. Figure 4.3-5(a) shows the concentration enhancement of Bacillus cereus DNA labelled with SYBR green and RPE. The DNA reached an apparent fluorescence peak intensity plateau at CE = 2800 within 225 seconds. RPE reached a plateau at CE = 1060 within 210 seconds. Figure 4.3-5(b) shows that both DNA and RPE are trapped at stable locations in the nanochannel. DNA focussed at 78 μm and RPE focused at 93 μm. It is notable that DNA was introduced at the low salt microchannel (at 100 μm) and has focused at the other side of RPE, which was introduced at the high salt buffer (at 0 μm). Figure 4.3-5(c) shows the band widths of RPE and DNA over time. The RPE band tended to narrow over time to 4.2 μm FWHM at 270 seconds and DNA broadened to 22.6 μm FWHM at 240 seconds. Figure 4.3-5(d) shows the superimposed fluorescence images of DNA and RPE, offset by 30 seconds. The time for the DNA image is listed at the left as 60s, 120s, 180s, and 240s; so the RPE image times were 90s, 150s, 210s, 270s. Two distinct peaks are visually discernible, green

for DNA and red for RPE. Below the images is a normalized intensity profile of the 240s time interval overlap image. The separation between the peaks was approximately 15 μm so the peak separation resolution quality was calculated to be $R_s = 1.1$ using the equation in the figure with W_{RPE} being the FWHM of the RPE peak and W_{DNA} being the FWHM of the DNA peak. The resolution value attained here appears to be sufficient, but for high performance liquid chromatography (HPLC), it is typically recommended to reach an $R_s > 1.7$ for reasonable separation. From the data found in earlier figures 4.3-3 and 4.3-4, a higher resolution might be achievable by increasing the voltage bias and by decreasing the concentration of DNA in order to sharpen the DNA focus band (W_{DNA}), thus minimizing peak overlap.

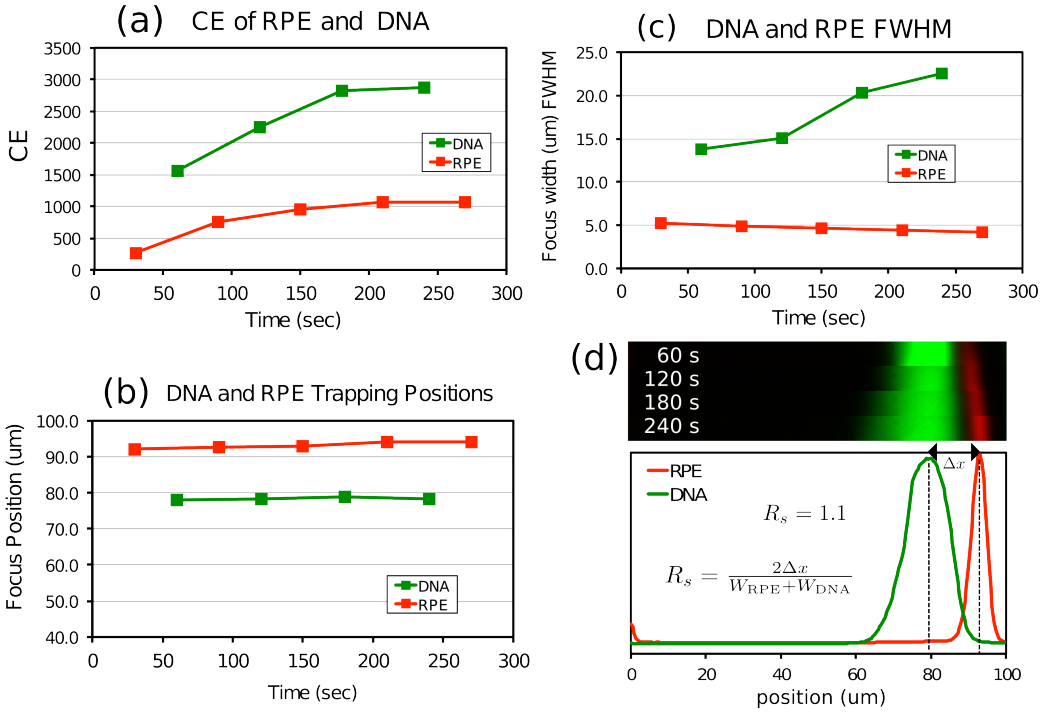

FIGURE 4.3-5: Bacillus cereus DNA and R- phycoerythrin (RPE) separation within the nanodevice under a conductivity gradient. (a) Concentration enhancement of RPE (red) and DNA (green) (b) Trapping position for RPE (red) and DNA (green). (c) Full width half maxiximum band width measurement for RPE and DNA. (d) Images of superimposed fluorescence of RPE and DNA over time. The plot beneath shows a normalized profile of DNA and RPE focusing and separating together at 240 seconds.

4.4 Conclusion

Nanochannel methods such as the gradient electrofocusing techniques presented here, offer a potential to improve the state of the art of DNA separation and sequencing, reducing costs across a wide range of applications such as diagnostics, forensics, and front-line research. This chapter was dedicated to characterising the device and finding the optimal operating parameters for focusing Bacillus cereus DNA as well as separating DNA and R-phycoerythrin (RPE) simultaneously within the nanochannel. It was observed that higher concentrations of DNA at the microchannel resulted in faster focusing of DNA at the trapping location. However, this also resulted in wider focus bands. A higher voltage bias was found to sharpen the DNA focus band and increase the rate of concentration enhancement at the trapping location. Separation of DNA and RPE successfully resulted in two observable bands within the nanochannel with a resolution quality of $R_s = 1.1$.

References

[1] Eugene Y. Chan. Advances in sequencing technology. *Mutation Research/Fundamental and Molecular Mechanisms of Mutagenesis*, 573(1-2):13 – 40, 2005. Single Nucleotide Polymorphisms (SNPs): Detection, Interpretation, and Applications. 77

[2] E. C. Cox, C. D. Vocke, S. Walter, K. Y. Gregg, and E. S. Bain. Electrophoretic karyotype for dictyostelium discoideum. *Proceedings of the National Academy of Sciences of the United States of America*, 87(21):82478251, 1990. 78

[3] Y. Kim and M.D. Morris. Rapid pulsed field capillary electrophoretic separation of megabase nucleic acids. *Analytic Chemistry*, 67(5):784–786, 1995. 78

[4] Barbaros Cetin and Dongqing Li. Effect of joule heating on electrokinetic transport. *Electrophoresis*, 29(5):994–1005, 2008. 78

[5] Xiangchun Xuan and Dongqing Li. Joule heating in electrokinetic flow: Theoretical models. In Dongqing Li, editor, *Encyclopedia of Microfluidics and Nanofluidics*, pages 896–905. Springer US, 2008. 78

[6] L. Mitnik, C. Heller, J. Prost, and J. L. Viovy. Segregation in dna solutions induced by electric fields. *Science*, 267(5195):219–222, 1995. 78

[7] Yang-Wei Lin, Ming-Feng Huang, and Huan-Tsung Chang. Nanomaterials and chip-based nanostructures for capillary electrophoretic separations of dna. *Electrophoresis*, 26(2):320–330, 2005. 78

[8] S. W. P. Turner, M. Cabodi, and H. G. Craighead. Confinement-induced entropic recoil of single dna molecules in a nanofluidic structure. *Phys. Rev. Lett.*, 88:128103, Mar 2002. 78

[9] J. Han and H.G. Craighead. Separation of long dna molecules in a microfabricated entropic trap array. *Science*, 288(5468):1026–1029, 2000. 78

[10] Richard W. Hammond, Joel S. Bader, Steven A. Henck, Michael W. Deem, Gregory A. McDermott, James M. Bustillo, and Jonathan M. Rothberg. Differential transport of dna by a rectified brownian motion device. *Electrophoresis*, 21(1):74–80, 2000. 78

[11] Lotien R. Huang, Jonas O. Tegenfeldt, Jessica J. Kraeft, James C. Sturm, Robert H. Austin, and Edward C. Cox. A dna prism for high-speed continuous fractionation of large dna molecules. *Nature Biotechnology*, 20:1048–1051, 2002. 78

[12] S. Pennathur, F. Baldessari, M. Kattah, P. J. Utz, and J. G. Santiago. Electrophoresis in nanochannels. *July 17-20 2006; Miami, FL. . ASME Joint US - European Fluids Engineering Summer Meeting; July 17-20, 2006; Miami, FL.*, 2006. 78

[13] David W. Inglis, Ewa M. Goldys, and Nils P. Calander. Simultaneous concentration and separation of proteins in a nanochannel. *Angewandte Chemie International Edition*, 50(33):7546–7550, 2011. 79

[14] Wei-Lun Hsu, Dalton J. E. Harvie, Malcolm R. Davidson, Helen Jeong, Ewa M. Goldys, and David W. Inglis. Concentration gradient focusing and separation in a silica nanofluidic channel with a non-uniform electroosmotic flow. *Lab Chip*, 14:3539–3549, 2014. 83

[15] Takeshi Suzuki, Keiko Fujikura, Tetsuya Higashiyama, and Kuniaki Takata. Dna staining for fluorescence and laser confocal microscopy. *Journal of Histochemistry and Cytochemistry*, 45(1):49–53, 1997. 84

5

PNA:DNA Hybridization and Electrofocusing

Abstract. Conductivity gradient electrofocusing was performed within nanofluidic channels to demonstrate a nanofluidics approach to detect hybridization between peptide nucleic acids (PNA) and DNA. Alexa Fluor 555 labelled PNA (18 bp) designed to be complementary with a sequence of fluorescein 488 labelled oligonucleotides were focused within a conductivity gradient and characterized. As controls, conventional agarose gel electrophoresis and polyacrylamide gel electrophoresis were compared with the proposed nanofluidic gradient electrofocusing method. While DNA:PNA hybridization could not be confirmed by any of the techniques, PNA:oligonucleotide hybridization was detected within polyacrylamide gel and the nanofluidic conductivity gradient approach using multiple frequency detection to spot the DNA:oligonucleotide overlap. However, agarose gel lacked the spatial resolution to discern hybrids from homogeneous PNA samples. Compared to the gels used in these trials, the conductivity gradient approach proved superior in resolving distinct molecular trap positions between the hybridized analytes vs unhybridized PNA or oligonucleotides strands alone. Moreover, the nanofluidic electrofocusing method was capable of achieving a focus within 300 seconds while gel electrophoresis methods required 50 minutes. The conductivity gradient

approach was also used to examine the degree of hybridization achieved when there exists a G-G base-pair mismatch between otherwise complementary oligonucleotide and PNA strands. It was found that a high degree of fluorescence overlap (approximately 90%) was achieved for properly matched PNA:oligonucleotide hybrids but approximately 83% overlap was observed for hybrids having a single base-pair mismatch.

5.1 Introduction

Molecules designed to recognize specific positions and sequences within DNA have become an essential tool in research areas of molecular biology, supramolecular chemistry and nanotechnology. Nucleic acids bind to a large number of naturally occurring and synthetic ligands. Triplex forming oligonucleotides [1][2] and pyrrole-imidazole polyamides have been designed to bind to the major and minor grooves of DNA structures.

Intercalating agents can insert their aromatic rings between two adjacent base pairs of double stranded DNA [3] and minor groove binding ligands [4] have also been known to alter biological processes involving DNA structure. However, until relatively recently, the only ligands available with the high degree of selectivity required to recognize a single sequence in ds-DNA nucleic acids were DNA strands themselves. Specially designed oligonucleotides were known to provide the highest specificity of recognition since they bind directly to the Watson-Crick hydrogen bonding sites of a complementary single-stranded sequence. They are also capable of recognizing the major groove of double helical DNA at specific sequences by forming Hoogsteen or reverse Hoogsteen hydrogen bonds with purine bases of the Watson-Crick base pairs, creating a triple helix, which is also a sequence-specific interaction involving primary homopurine homopyrimidine sequences in the double-helical target.

5.1.1 Peptide Nucleic Acid

Peptide Nucleic acid (PNA) has been found to be a powerful biomolecular tool that mimics the behaviour of DNA, binding to nucleic acids in a complementary sequence-specific fashion through a common Watson-Crick base pairing scheme between the PNA strand and DNA strand but also through Hoogsteen pair bonds. Using PNA as a molecular probe instead of oligonucleotides has several advantages as described by Nielsen et al [5]. PNA consists of N-(2-aminoethyl)-glycene units linked by a neutral peptide backbone. Unlike in DNA, the PNA backbone contains no phosphate groups,

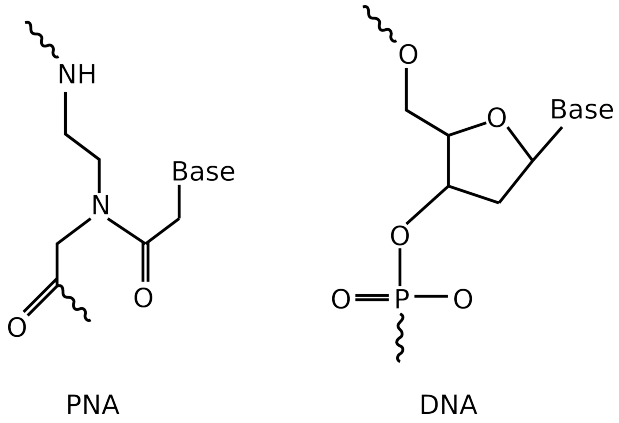

Figure 5.1-1: The structure of PNA monomer compared to DNA nucleotide

which accounts for the neutral charge of PNA (figure 5.1-1). As a result, due to the lack of electrostatic repulsion between PNA:DNA, the bond between the PNA:DNA is stronger than that of a DNA:DNA bond at low to medium ionic strength solutions [6]. In addition, PNA's nonnatural polyamide backbone is resistant to degradation by nucleases and proteases [7]. Compared to DNA:DNA duplexes, the stability of PNA:DNA duplexes is strongly affected by imperfect sequence matching. For 15-mer PNA/DNA, the ΔT of single mismatch was found to be 15°C compared to 11°C for a DNA/DNA duplex [8]. Jensen et al. [9] performed a systematic study on the thermal stability (T_m) of PNA:DNA hybrids as well as PNA:RNA hybrids, finding that PNA:RNA hybrids are even more robust than PNA:DNA hybrids. The high chemical and biological stability of PNA makes PNA one of the best performers among hundreds of DNA mimics [10].

5.1.2 PNA Applications

The many remarkable hybridization properties of PNA offer just as many applications [8]. PNA's high sequence selectivity has been found to be advantageous in therapeutic and diagnostic applications involving hybridization between complementary nucleic acid strands such as in fluorescence in situ hybridization (FISH) [11], DNA/RNA microarrays [12], and single nucleotide polymorphism (SNP) assays [13]. Zhang et al. [10] described how PNA could offer a superior method to detect the human immunodeficiency virus(HIV). The current method for nucleic acid detection of HIV infection rely on enzymes and nucleic acid probes, which all have limited shelf lives and poor stability [14]. While they are highly sensitive and accurate virus identification methods, they rely on signal amplification methods such as polymerase chain reaction (PCR)

and other non-PCR enzyme-based methods. All of these methods require some degree of care during storage or deployment. PNA, on the other hand, is a synthetic, non-degradable molecule that could even survive without refrigeration while still maintaining excellent sensitivity and accuracy [10]. PNA is also extremely stable in acidic environments where DNA would experience depurination (the β-N-glycosidic bond is hydrolytically cleaved releasing a nucleic base).

PNA is also highly tunable to specific analytical applications. Pokoroski et al [15] replaced the ethylenediamine portion of the aminoethylglycine peptide nucleic acids with a (S,S)-trans-cyclopentane diamine unit and significantly increased binding affinity and sequence specificity to DNA, thus making PNA ideal for use as nucleic acid probes. PNA can also have its backbone altered so that it bears either negative or positive charges [16] which could be useful for electrophoresis separation applications.

Pseudo-complementary PNA (pc-PNA) has been found to be particularly promising for gene targeting since they exhibit fewer sequence limitations than any other ds-DNA-binding ligands. Also, pc-PNA induces site-selective bending in DNA duplexes [17]. pc-PNA differs from conventional PNA by a few structural nucleobase substitutions. Along with two of the standard nucleobases, guanine (G) and cytosine (C), pc-PNA carries modified set of nucleobases: 2,6-diaminopurine (D) and 2-thiouracil (U^S), in place of adenine (A) and thymine (T), respectively. Complementary pc-PNA strands experience a steric clash that repels D and U from each other, hence significantly obstructing the complementary interactions between modified PNA nucleobases. However, this does not prevent pc-PNA from binding to the corresponding sequences in DNA carrying the standard nucleobases [18][19] (Figure 5.1-2). In this way, it is possible to achieve double duplex invasion PNA:DNA hybrids.

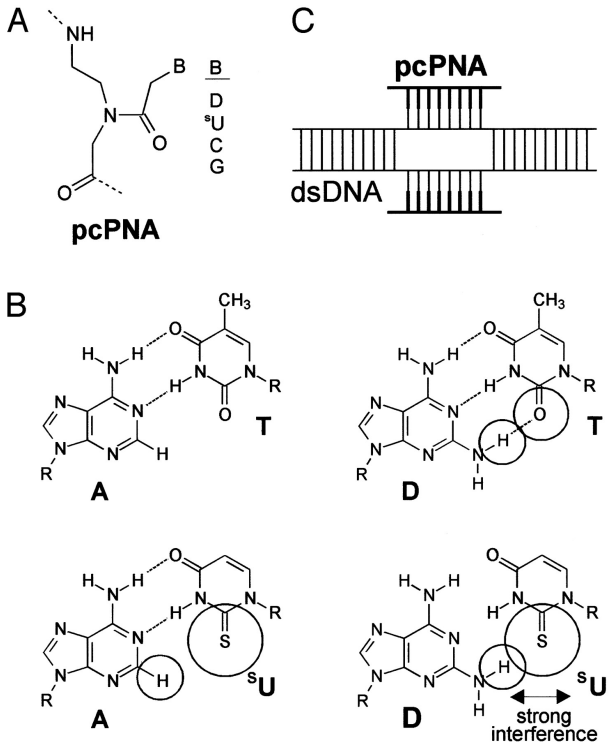

Figure 5.1-2: Source: PNAS 2004 [19]. (A) structure of pseudocomplementary PNA. (B) Schematic drawing of adenine:thymine (A:T), diaminopurin:thymine (D:T), diaminopurine:thiouracil (D:^{S}U), and adenine:thiouracil (A:^{S}U) base pairs. Diaminopurine (D) can form an extra hydrogen bond with thymine (T), but a steric clash occures between diaminopurine (D) and thiouracil (^{S}U). By this mechanism, pc-PNA binds favorably with DNA but not with its own complement (C) Illustration of pc-PNA binding with DNA through double Duplex invasion.

5.2 Background

5.2.1 Watson-Crick Base Pairing

Watson and Crick [20] described the basic structure of DNA and the phenomenon through which base pairs bind together to form the double helical structure. Specific hydrogen bonding patterns permitting complementary binding between guanine-cytosine (G-C) and adenine-thymine (A-T) base pairs. By this mechanism, specific base pair sequences of single stranded nucleotide sequences will hybridize favourably with a complementary nucleotide sequence. Chemical analogues of nucleotides and intercalators may take the place of standard nucleotides due to their isoteric chemistry and establish a non-canonical base pairing. While these insertions can cause errors during DNA replication, if these non-canonical binding are exploited intentionally, it

is possible to selectively target and identify sequences within DNA and RNA strands.

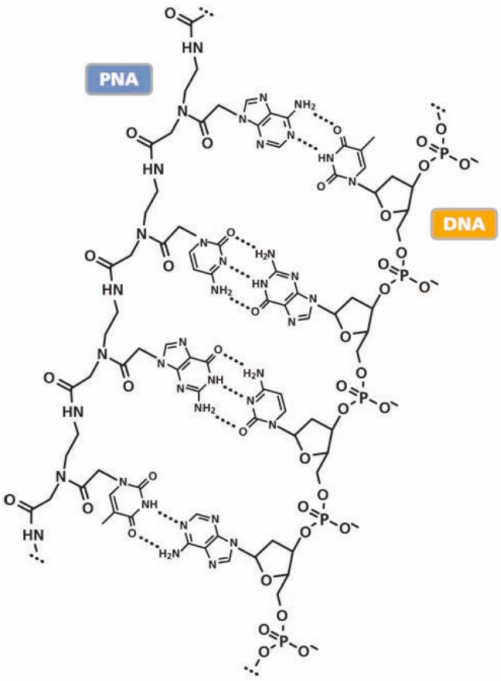

Figure 5.2-3: Watson-Crick pairing of PNA and DNA.

5.2.2 Hoogsteen Base Pairing

Karst Hoogsteen [21] described the crystal structure of a complex in which analogues of A - T and G - C base pairs can be formed with a different geometry than that described by Watson and Crick. Hoogsteen pairs result in a double helix of a significantly different shape than Watson-Crick helix, but these pairs are rarely observed in the wild. The most interesting aspect of Hoogsteen pairing is that it permits the formation of triple-stranded helices, and quadruplex structures. DNA triplex formations occurring in nature (sometimes referred to as H-DNA) are a rare form of DNA that is found in vitro or sometimes during recombination and DNA repair [22]. They form by the pairing and intertwining of 3 strands of single stranded DNA (ss-DNA). Usually, two of the three strands contain pyrimidines and a third contains purines. Triplexes occur when pyrimidine or purine bases occupy the major groove of the DNA double Helix forming Hoogsteen pairs with purines of the Watson-Crick basepairs. DNA triplexes can be formed between triplex forming oligonucleotides (TFO) and target sequences on

duplex DNA. Figure 5.2-4 illustrates the molecular arrangement in which both Watson-Crick and Hoogsteen pairs can occur simultaneously to form triplex pairings. Figure 5.2-5 shows several possible modes of PNA hybridization considering the options of forming Watson-Crick bonds and Hoogsteen bonds simultaneously.

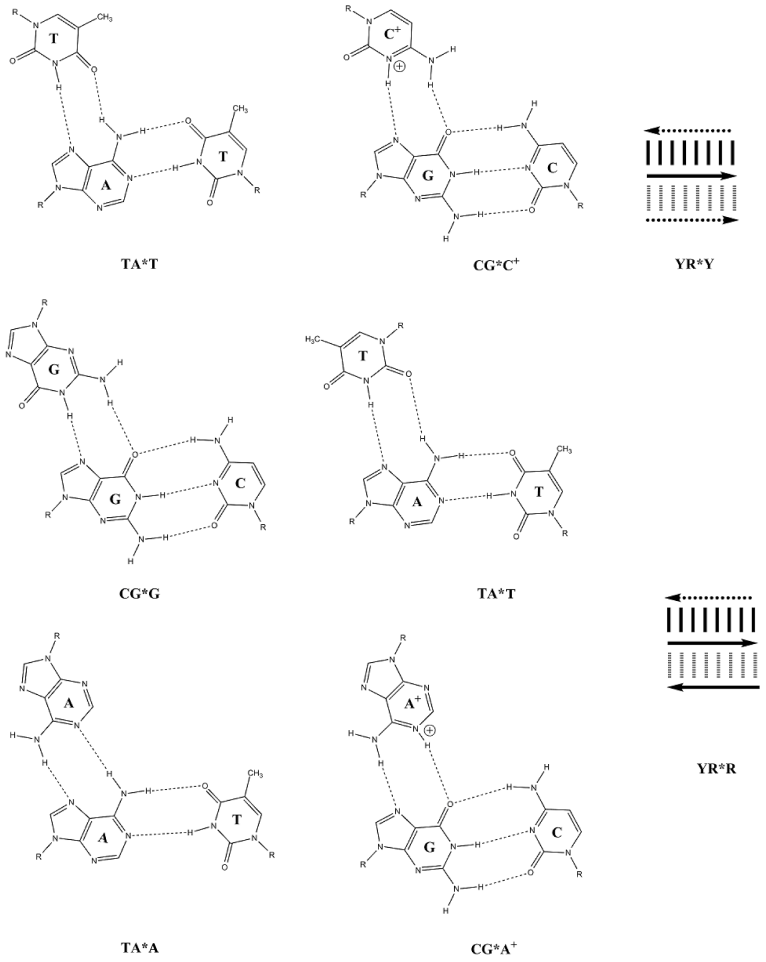

Figure 5.2-4: Base triads in a DNA triplex helix structure. In each triplet, the base shown on the top left forms hydrogen bonds with the base in the middle. Y indicates a pyrimidine (thymine or cytosine) and R indicates a purine (adenine or guanine). The arrows on the right indicate the direction and types of strands forming YR*Y and YR*R triplexes. Thick vertical lines indicate Watson-Crick base pairs, dashed vertical lines indicate Hoogsteen hydrogen base pairs. Solid arrows indicate purine strands, dashed arrows indicate pyrimidine strands. (Wikimedia Commons [23])

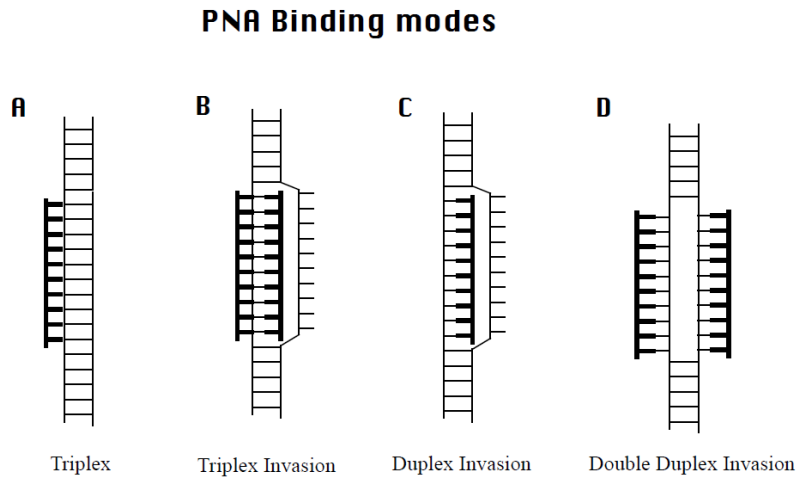

Figure 5.2-5: Possible modes of PNA binding. (A) shows hogsteen triplex binding. (B) shows a triplex invasion with one PNA strand forming Hoogsteen pairs and one invading PNA strand displacing DNA and forming Watson-Crick pairs. (C) shows duplex invasion of a PNA sequence displacing DNA and froming Watson-Crick pairs. (D) shows a double duplex invasion structure wherein two PNA sequences invade either side of the DNA duplex forming Watson-Crick pairs.

5.2.3 Proposed Scheme for Detecting Hybridization

Typically, DNA is found in a double stranded form (ds-DNA), wherein conjugate base pairs combine in anti-parallel orientation and coil in a helix formation. However, ds-DNA may be separated (denatured) under heat into single stranded DNA (ss-DNA) in which form it may bind with another chain of base-pairs that match the DNA sequence during an annealing process (renaturation). In this study, PNA was used to invade a duplex DNA structure of ds-DNA to form hybrid with one of the DNA strands, leaving the other strand of DNA un-conjugated. The PNA strand essentially replaces a DNA strand within the target sequence location so it becomes possible to investigate some property of the targeted DNA. In addition, the hybridization may cause changes to the molecule's mobility, i.e., charge to mass ratio. Figure 5.2-6 shows how mobility changes within a DNA molecule can be exploited in order to make hybridization detectable within the nanochannel conductivity gradient scheme. DNA's electrophoretic mobility within an electric field, μ_{DNA} is proportional to its charge q_{DNA} and inversely proportional to its mass m_{DNA}. DNA carries a negative charge along with each phosphate group along its backbone so it has a charge to mass ratio independent of DNA length. PNA, on the other hand, does not carry a charge in its backbone (unless modified to carry a positive or negative charge [16]) so it has a mobility μ_{PNA} which depends

on the PNA mass and acquired charge. These differences in mobility result in PNA and DNA being trapped in a different locations along the channel. If DNA hybridizes with PNA, then PNA will modify the charge to mass ratio of DNA:PNA complex by contributing a mass component or changing the mass of the molecule. Assuming a sample is not fully hybridized, it is reasonable to expect 3 different focusing positions within the channel: one for PNA, one for DNA and one for PNA:DNA hybrid molecules. Figure 5.2-6 illustrates this. Note that this figure is just an illustrative example of the hypothesis and does not intend to suggest where PNA, DNA or the hybrid would focus. It only proposes that there would be a difference in focusing location between the species.

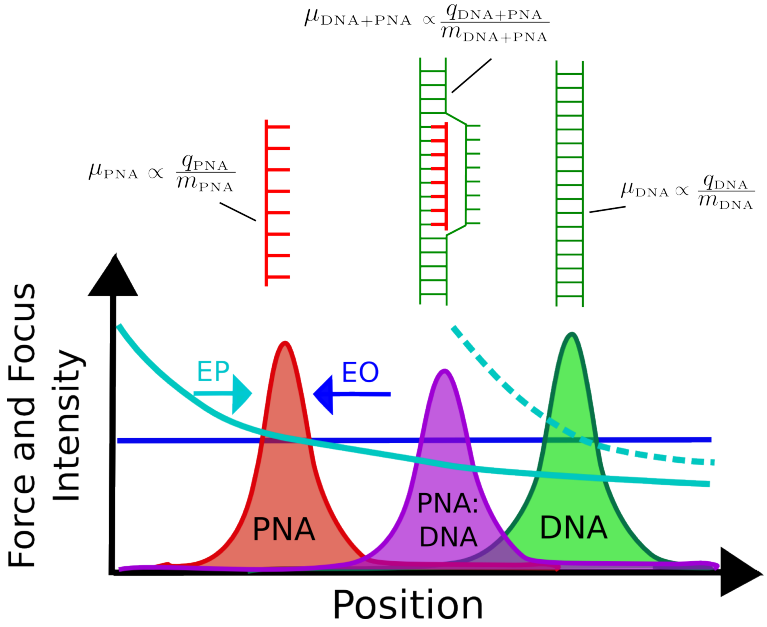

Figure 5.2-6: Illustration of proposed scheme for hybridization detection. PNA and DNA have distinct mobility μ within an electric field which is dependent on their mass and charge. If PNA and DNA are hybridized, the mass and charge of the molecule will be modified and there will be a new trap location for the PNA:DNA complex. Electrophoresis force throughout the channel acts on individual biomolecules and is augmented by the conductivity gradient along the channel and the molecular mobility. Electroosmosis (EO) force represents a bulk Stokes flow and is considered constant throughout the channel due to conservation of mass requirement for bulk flow.

The blue line in the figure indicates a constant electroosmotic (EO) force. This is because the EO acts on the biomolecules through bulk flow of the fluid which is driven by Stokes drag force from the mobile sheath of charge carriers composing the double electric layer near the surface of the channel. We treat EO as a bulk flow force because,

as discussed earlier, a 1D approximation can be made due to the low Peclet number of our system and the small channels (<100 nm). A low Peclet number means that the rate of diffusion through the depth of the nanochannels is faster than the rate of longitudinal flow through the nanochannels. Therefore, fluid at any point along the channel in the longitudinal direction can be assumed to be moving as a bulk fluid, experiencing a balance of forces from the high EO forces and EO forces on either side of the channel simultaneously. So although the electric field differs throughout the length of the channel due to the salt concentration gradient, bulk flow due to EO must be constant due to conservation of mass. Electrophoresis (EP), on the other hand, acts on individual DNA and PNA particles and is augmented throughout the length of the channel by the conductivity gradient. As a charged particle approaches nearer to the low salt end of the nanochannel, the local electric field drastically increases and the EP force begins to dominate the counteracting EO force. While the force profile shape of EP along the channel is determined by the conductivity gradient, the difference in mobility between PNA and DNA will result in different locations where the EP (cyan line) crosses the counteracting force line of EO. As illustrated in 5.2-6, the specific mobility of PNA causes the cyan colored EP line to cross the EO line at a different location than the DNA dotted cyan coloured EP line. Thusly, unique molecular trap locations are formed depending on the mobility of particular molecules which offsets the location where EO and EP forces for a specific molecule are equal and opposite.

5.3 DNA:PNA Hybridization

5.3.1 Methodology

Conductivity Gradient Electrofocussing

PNA, oligonucleotides, and PNA:oligonucleotide hybrids were focussed within the nanofluidic device described in chapter 4 and Appendix A.1 using conductivity gradient electrofocusing. The gradient was formed by introducing a constant perpendicular flow of phosphate buffer to both sides of the nanochannel to "lock" a dissimilar salt concentration at each end of the nanochannel. The top nanochannel experienced a perpendicular flow of phosphate buffer containing 241 mM NaCl while the bottom nanochannel experienced a perpendicular flow of phosphate buffer containing 24 mM NaCl. Note that the salt concentration difference was formed by dilution of the high salt buffer so the buffer strength of the bottom channel is of lower strength. However, this did not have an appreciable effect on the focusing nor did it compromise

the structure of the DNA, PNA, or DNA:PNA complexes. As a measure of stability, oligonucleotides of 18 bp lengths were calculated to have a melting point at 36.6°C at room temperature within 12 mM NaCl concentrations and 55.3°C within 241 mM NaCl concentrations [24]. Since all experiments were conducted at 20°C conditions, and PNA is known to have somewhat higher melting points than oligonucleotides, there is reasonable confidence that the hybridized analytes were intact during experiments even when stored in low salt 24 mM NaCl buffer solutions. Positive electrodes were introduced to both the inlet and outlet of the high salt flowing microchannel running perpendicular to the nanochannels and a negative (ground) electrode was applied to the inlet and outlet of the low salt microchannel running perpendicular across the opposite end of the nannochannels.

The device nanochannels were 200 μm long and were gently tapered (15 nm wide at high conductivity end to 10 nm wide at low conductivity end). The tapering could be used to accentuate the conductivity gradient to yield a greater sharper focus bands, but under this slight tapering, this was a negligible effect. The nanochannel depths were 86 $\pm$ 4 nm. The voltage bias applied for all trials was either at 2.0 volts or 3.9 volts and resultant current through the channel was measured between 0.1 - 0.2 μA. The supply buffer flow was not driven by capillary tube pressure as in previous experiments but rather by osmotic surface tension "wicking" action of the channels itself. Approximately 10μl droplets of buffer and analyte sample were pipetted to the inlets of each microchannel and permitted to flow through the microchannels. Every 10-20 minutes, the droplets were refreshed to minimize changes in salt concentration due to evaporation. Between the trials, the channels were flushed with de-ionized water and phosphate buffer solutions that matched the conductivity to be used in the upcoming trial.

The 18 base-pair PNA probes (purchased from Invitrogen - Life technolgies) were selected to compliment the 16S ribosomal RNA sequence within the Bacillus cereus genome [25]. The sequence was chosen from several appropriate candidates according to the criteria for successful PNA:DNA binding (calculated by *probeBase* [26]) The chosen sequence was found present 13 times within the Bacillus cereus strand (ATCC14579 strain) prior to DNA shearing.

Single stranded oligonucleotides were also purchased with a sequence that mimics the 16S rRNA sequence so the PNA probe could bind directly with the oligonucleotides. This simplified the hybridization process since there was no necessity to first denature a DNA duplex before hybridization. PNA that is perfectly matched to the DNA and oligonucleotide sequence will henceforth designated as "PNA-Probe-1", and PNA that

had a G-G mismatched set of base pairs with DNA and oligonucleotides will henceforth be designated as "PNA-Probe-2". The sequences of PNA-probe-1, PNA-probe-2 and oligonucleotides is displayed in table 5.1.

Name	Terminus	Sequence	Terminus
Probe 1	Alexa 555	5' - TG CGG TT**C** AAA ATG TTA T - 3'	-
Probe 2	Alexa 555	5' - TG CGG TT**G** AAA ATG TTA T - 3'	-
Oligo	-	3' - AC GCC AA**G** TTT TAC AAT A - 5'	Fluorescein 488

Table 5.1: Oligonucleotide:PNA Hybridization sequences

The fluorescent marker for PNA primers was chosen to be Alexa Fluor 555 at the 5' N terminus. Alexa 555 was selected instead because it has comparatively increased photostability, higher extinction coefficient, and a superior brightness to the alternative fluorophores like Cy3 [27]. The excitation of Alexa Fluor is at 555 nm and the emission is at the 565 nm wavelength. The oligonucleotides were labelled with fluorescein 488 which had an excitation at 480 nm and emission at 525 nm. The fluorescein-labelled oligonucleotides were imaged under a DM-IRB Leica inverted fluorescence microscope with a filter cube having a single band excitation filter passing between 475 and 497 nm and an emission filter passing only the wavelengths within the region of 520 nm. Fluorescence of Alexa Fluor-labelled PNA was imaged with the use of a filter cube having an excitation filter passing between 510 and 560 nm and a high pass emission filter, passing wavelengths greater than 560 nm. In this way, the signals from Fluorescein-labelled oligonucleotides and Alexa Fluor-labelled PNA were independent of one another.

Hybridization of PNA and Oligonucleotides was trivial due to both species being single stranded base pair chains. The process consisted of mixing PNA and Oligonucleotides at 1:1 molar ratio and heating and mixing for 10 minutes. After cooling in the fridge for 30 minutes, the hybridized analyte was taken to be used in either gel electrophoresis trials or nanochannel electrofocusing trials.

DNA Shearing

Bacillus cereus DNA was sheared on a Covaris E220 Ultrasonicator at the University of New South Wales (UNSW). The protocol for DNA shearing to our target of 150 bp

can be found in Appendix A.4.1. The resultant DNA sample was then sized with an Agilent Bioanalyzer 2100 and confirmed to be a distribution spanning between 50 - 250 bp, peaking at 150 bp (Appendix A.4.1). Shearing was necessary because long DNA strands could not be flowed through the nanochannels. Also DNA needed to be as short as possible so that there may be an observable difference of mobility between DNA and DNA:PNA hybridized molecules. If the DNA molecule is too large, the modification of an 18 bp hybridization could not make a noticeable difference in mobility, and therefore the trapping locations in electrofocusing experiments.

Agarose Gel Electrophoresis

In order to assess the PNA : oligonucleotide hybridization detection performance, PNA : oligonucleotides were also focused within conventional electrophoresis gel. Trials were performed using a standard 1% agarose gel mixture in a tris base, acetic acid and EDTA (TAE) running buffer within a standard laboratory gel electrophoresis kit. The gel was stained with GelRed so the DNA and PNA could be viewed under a UV transilluminator after the trial. A voltage of 100 V was applied for 50 minutes until the stained molecules appeared to approach the bottom edge of the gel. DNA hybridization with PNA was performed by heating a solution of 1.3 μM sheared Bacillus cereus DNA and 1.6 nM PNA to 85°C so the ds-DNA denatures, permitting PNA to invade the targeted sequences. The concentrations of PNA and DNA was calculated to approximately achieve 1:1 ratio of PNA strands to DNA target sequences within the sheared helices.

Polyacrylamide Gel Electrophoresis

While agarose gels successfully separate DNA fragments of 50-20,000 bp, polyacrylamide gels have a considerably higher resolving power for small 5-500 bp fragments of DNA and is more suitable for analyzing single-stranded DNA. However, acrylamide is a potent neurotoxin so we did not attempt to make the gel using our facilities as was the case for agarose gel. polyacrylamide pre-cast mini-PROTEAN 10% TBE electrophoresis gels were purchased from Biorad inc. Analytes were mixed into a standard electrophoresis loading buffer, composed of 60% glycerol, 10mM Tris, 60 mM EDTA and a colorant, bromophenol blue at 0.2% set to a pH of 8.3. Then the electrophoresis gel cast was inserted into a Mini-PROTEAN Tetra electrophoresis cell and a voltage of 100 V was applied for 50 minutes. An image of the focusing was then taken under an open Ultra-Lum transilluminator with a standard cell phone camera (LG Nexus 5).

DNA Fluorescence Labelling

For polyacrylamide Precast gel electrophoresis trials, gel staining was not used. Instead, DNA was labelled with a separate SYBR Green fluorophore (excitation wavelength: 497 nm; emission wavelength 520 nm) so that DNA fluorescence and PNA fluorescence could be distinguished. SYBR green was supplied in 10 000X concentration in DMSO, aliquoted into 1000x vials diluted with deionized water. Then adapting some of the prescribed labelling techniques used for PCR [28][29], Bacillus cereus DNA sample vials were pipetted with SYBR Green to achieve a 4x SYBR Green working solution. approximately 10 minutes. In this way, we were able to view DNA shows up as a green fluorescence under the transilluminator while PNA's Alex-555 label appears red. Also, the filter cubes within the DM-IRB inverted fluorescence microsocope could view SYBR green fluorescence and Alexa 555 fluorescence independently.

5.3.2 Discussion

PNA Mobility Characterization

We observed that despite the inherent zero net charge on the backbone of PNA, it could still focused within the nanochannels under an applied voltage. This phenomenon may be due to PNA molecules acquiring a negative charge within electrolyte solutions, thus forming its own debye layer then acquiring a mobility within the solution. Figure 5.3-7 shows focusing data of PNA at various concentrations when introduced at the high salt end with the phosphate buffer (with a 241mM NaCl concentration). Figure 5.3-7(a) Shows that PNA at 1.0 uM concentration yields the highest concentration enhancement factor (CE). (b) provides another perspective of concentration data by evaluating the total concentration at the focus band within the channel. The 6.66 μM concentration results in highest overall concentration even though the CE is not as high as other concentrations used. (c) Shows the stable peak positions of each of the concentrations of PNA introduced. All of the bands tend to focus at around 90 - 99 μm into the channel. (d) shows the full width half maximum measure of the focus band widths over the span of 300 seconds. The widest band was the 6.66 μM concentration. (e) is a distillation of CE found in the previous figure a but showing only the CE at 300 seconds to illustrate the trend of increasing concentration in the sample solution. CE tends to decrease as concentration increases. We can conclude that starting concentrations of greater than 1.0 μM will yield higher concentration at the focus, but yield lower CE factors over all.

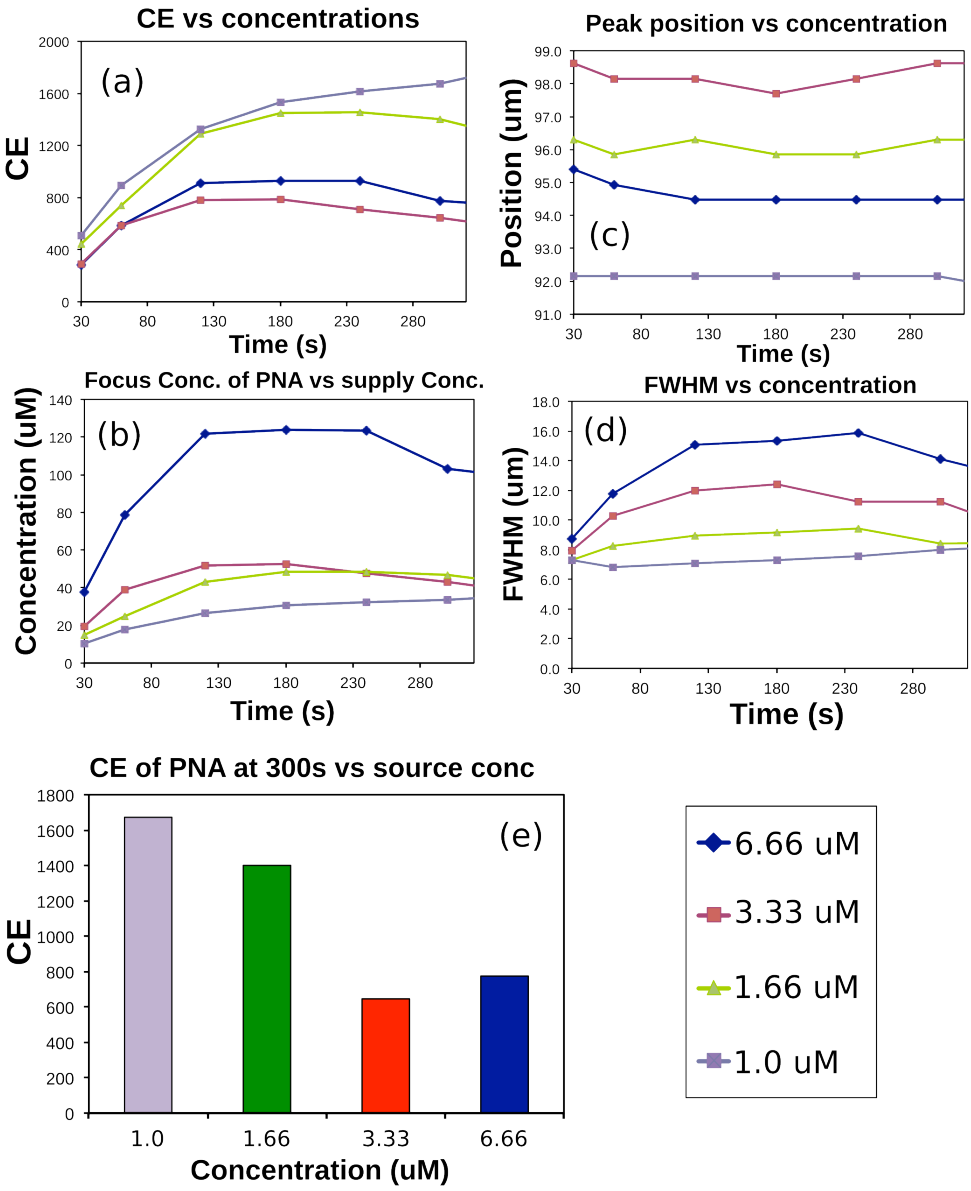

Figure 5.3-7: Characterization of PNA within the nanochannels. (a) Concentration enhancement (CE) over time for different PNA initial concentrations (source concentrations). (b) total concentration at the focus over time comparing the initial PNA source concentrations. (c) Focus peak positions over time for each concentration of PNA source concentration. (d) The width of peaks (FWHM) for each initial PNA concentration. (e) bar graph showing the relative CE at 300 seconds focusing time for each initial source concentration. The concentrations 6.66, 3.33, 1.66, 1.0 μM corresponds to 37.4, 18.7, 9.0, 5.6 μg/mL in PNA mass per volume concentration repectively.

Separation of DNA and PNA

Before attempting to hybridize DNA and PNA, simultaneous concentration and separation of sheared Bacillus cereus DNA and PNA was performed within the nanochannels.

For this trial, the same phosphate buffer arrangements were used as described in the conductivity gradient methodology section, but instead of using 200 nm tapered channels, nontapered channels of 100 μm length, 20 μm width were used. A voltage of 0.4 V was applied and a constant capillary tube pressure flow was used to supply nearly constant flow of phosphate buffer and sample. Both DNA and PNA were supplied through the high conductivity (241mM NaCl) end of the channel. During focusing, fluorescence images of Alexa Fluor 555 (bound to PNA) and SYBR Green (bound to DNA) were taken in alternating 30 second intervals at 1 second exposure.

PNA:DNA hybridization was not considered in this trial because DNA was not heated to the point of denaturing. PNA had no access to the Watson-Crick binding sites that would be exposed in single stranded DNA (ss-DNA) but not double stranded DNA (ds-DNA). Figure 5.3-8(a) shows the PNA and DNA bands are rather wide: 25 μm and 30 μm full width half max measurements for PNA and DNA respectively. Figure 5.3-8(b) shows the concentration enhancement (CE) for DNA and PNA. DNA tended to have a much higher CE factor than PNA (2000 vs 500 for DNA and PNA respectively). This difference could be attributed to a higher concentration of SYBR green compared with Alexa Fluor bound to PNA. However, it was clear that DNA and PNA focus could be separated simultaneously within the nanochannel to be concentrated at unique positions along the nanochannel.

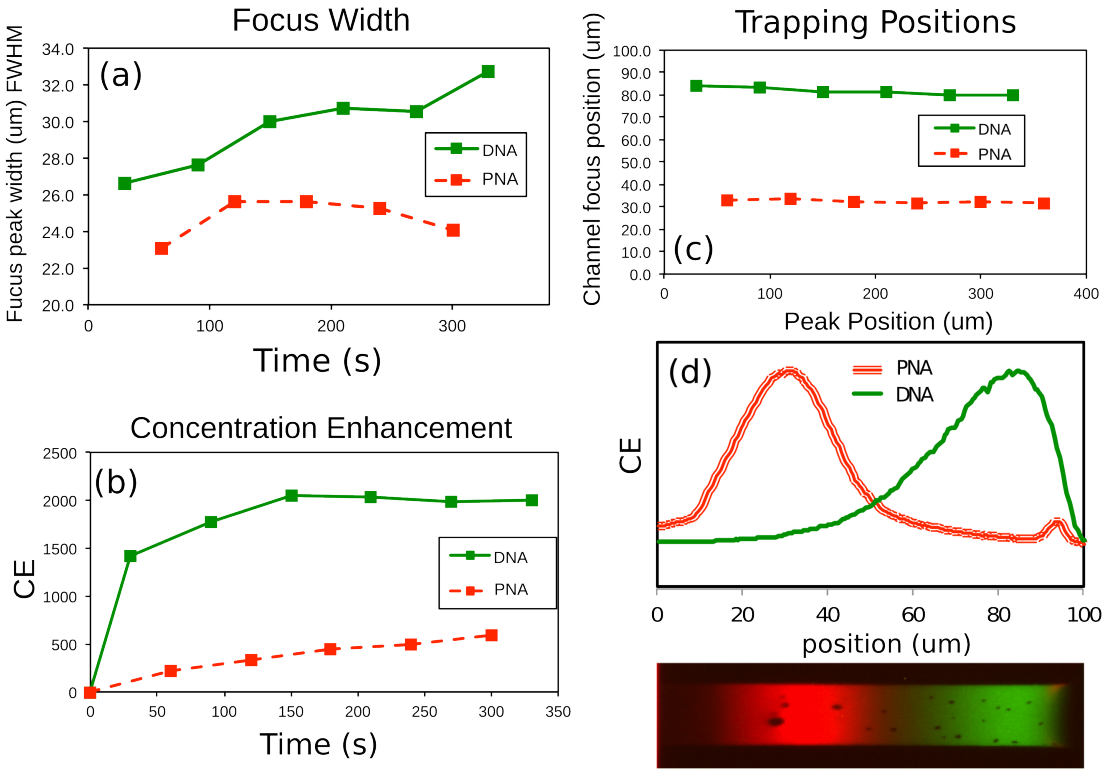

Figure 5.3-8: (a) The full width half max measure of the bands forming within the nanochannel over time. (b) The concentration enhancement factors for DNA and PNA over time. (c) the stable focus positions for DNA and PNA over time. (d) The focus profiles (normalized) for PNA and DNA in the nanochannel.

DNA Gel Electrophoresis in 1% Agarose

Figure 5.3-9 shows a preliminary trial focusing DNA and PNA and hybrids on the same agarose electrophoresis gel. Channel 1 contained standardized GeneRuler 1kbp (250 - 10,000 bp) DNA Ladder, channel 2 contained 1.6 nM PNA probe 2, channel 3 and 4 both contained 1.3 μM DNA, channel 5 contained hybridized 1.3μM:1.6nM DNA:PNA-probe-1, channel 6 contained hybridized 1.3μM:1.6nM DNA:PNA-probe-2, channel 7 contained Jena biosci 10kbp DNA ladder (100bp - 10,000 bp) for base pair sizing comparison (starting at 100bp). The DNA was sheared to approximately 150 bp lengths, so broad bands shown in channel 3 and 4 are expected. However, the 18 bp PNA-probe-2 band in channel 2 is not significantly separated from the 150 bp DNA band. Channels 5 and 6 look like a superposition of the PNA in channel 2 band and the DNA in channels 3/4, so differentiating between hybridized and non-hybridized PNA and DNA mixtures in channels 5 and 6 does not appear possible using the agarose gel

approach since the subtle changes in mobility cannot be discerned. There is little to no difference between channel 5 and channel 6 other than the brightness of the bands. But this was attributed to a nonuniform gelRed staining. It is necessary to try a gel system with a higher base-pair resolution.

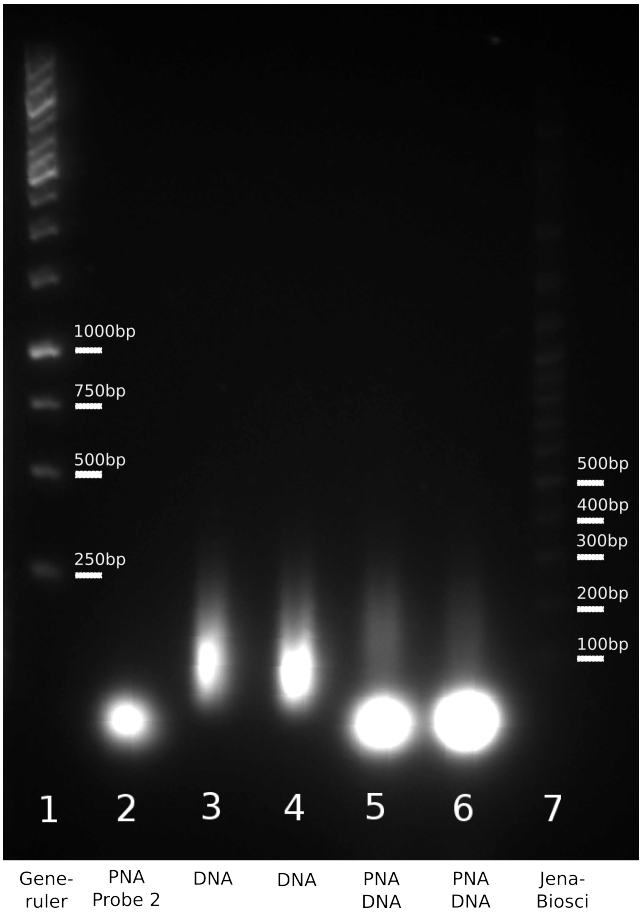

Figure 5.3-9: Gel electrophoresis spread of 1 percent Agarose in TAE buffer. Channel 1 contained standardized GeneRuler 1kbp DNA Ladder, channel 2 contained PNA probe 2, channel 3 and 4 contained DNA, channel 5 contained hybridized DNA:PNA probe 1, channel 6 contained hybridized DNA:PNA probe 2, channel 7 contained Jena biosci 10kbp DNA ladder for comparison.

DNA Gel Electrophoresis in Precast TBE Gel

Since agarose gel could not discern hybridization of PNA and DNA, a different approach was attempted with mini-PROTEAN Precast 10 percent Tris-borate-EDTA (TBE) gel purchased from Biorad. Instead of labelling all analytes with Gelred, SYBR Green was

used to label the 150 bp Bacillus cereus DNA and the Jena biosci 10kbp DNA ladder. Note that PNA was already pre-labelled with Alexa Fluor 555.

Figure 5.3-10 is an image of an electrophoresis spread through mini-PROTEAN Precast 10 percent TBE gel. The gel was loaded with 8 ul samples mixed with 1ul of loading buffer. Channel 1 contained Jena BioSci 10kbp DNA ladder as a base pair sizing reference, channel 2 contained 1 mM PNA Probe 1, channel 3 contained 1mM PNA Probe 2, channel 4 contained sheared Bacillus cereus DNA labelled with SYBR Green, channel 5 contained a DNA:PNA-probe-1 hybridization and channel 6 contained a DNA:PNA-probe-2 hybridization.

The polyacrylamide gel separation was superior to agarose gel separation in the previous section since a color difference between PNA and DNA is visible and the positions of the PNA and DNA bands were further apart. However it was still doubtful that the DNA and PNA successfully hybridize. As expected, Channel 4 contained a broad DNA band indicating the 150 bp shearing (confirmed by the alignment with the channel 1 Jena Biosci DNA ladder's lowest band representing 100 bp). However, channels 5 and 6 were expected to have two separate, superimposed bands visible: one DNA broad band, and one PNA band as well as a third hybridized band containing both green and red coloration (yellow) to indicate the degree of hybridization. However, the DNA band was not visible at all. It is suspected that the PNA may have interfered with the SYBR Green labelling of DNA. The SYBR Green may have preferentially bound to PNA.

Oligonucleotide Gel Electrophoresis

Since we could not confirm the 150 bp DNA:PNA hybridization on precast gels, we considered the possibility that 150 bp might not be short enough length to yield an appreciable mobility change for DNA:PNA compared to homogeneous DNA. Unfortunately 150 bp size was the practical limit of the ultrasonic shearing process.

This motivated us to try hybridizing PNA to an exact base-pair sequence of oligonucleotides matching the sequence of PNA-Probe-1 to more clearly demonstrate hybridization. Furthermore, Figure 5.3-11 shows that the fluorescence of both PNA and DNA clearly visible as a distinct color. The right side of Figure 5.3-11 shows a photograph close up of a region of the gel containing species of < 30 base pairs (according to a 10kbp Jena bioscience DNA ladder that was run in parallel). As could be expected, PNA probe 1 (red) was located in a similar location to the oligonucleotides (green) since both analytes are 18 bp in length. However, the PNA:oligonucleotide

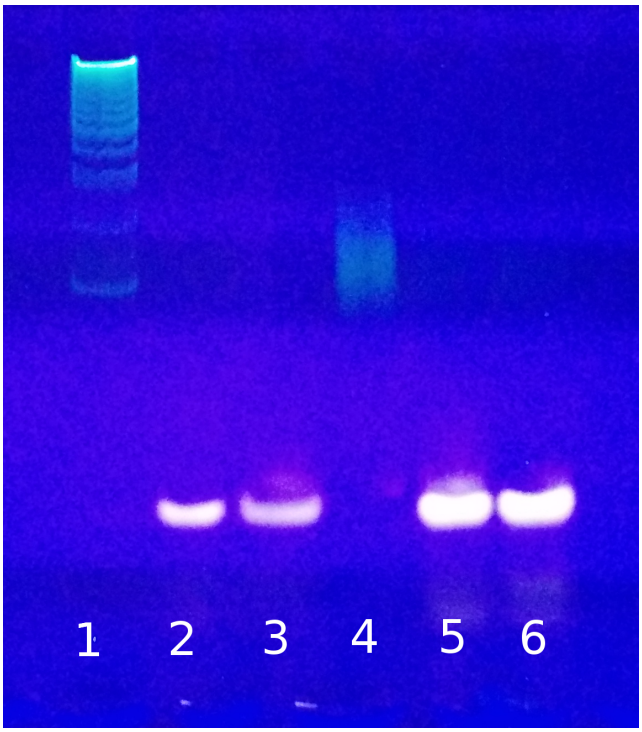

Figure 5.3-10: Electrophoresis spread through mini-PROTEAN Precast 10 percent Tris-borate-EDTA (TBE) gel. The gel was loaded with 8 ul samples mixed with 2ul of loading buffer. Channel 1 contained Jena BioSci 10kbp DNA ladder as a base pair sizing reference, channel 2 contained 1 mM PNA Probe 1, channel 3 contained 1mM PNA Probe 2, channel 4 contained sheared Bacillus cerus DNA labelled with SYBR Green (get exact quantity), channel 5 contained a DNA-PNA probe 1 hybridization and channel 6 contained a DNA-PNA probe 2 hybridization.

hybrid (yellow: red-green mix) was slightly shifted from the PNA and oligonucleotide positions. However, without the color differentiation, PNA and oligonucleotides and the hybrid would be difficult to discern because of their close proximity. In contrast, the right side of Figure 5.3-11 shows separate trials of nanochannel electrofocusing of PNA-probe-1, oligonucleotides and the hybrid under a 3.9V bias using the similar concentrations as in the gel electrophoresis trial. However, only requiring 300 seconds to achieve stable trapping. The focusing could be conceivably improved if the concentration was lowered since, as seen in the previous section, concentration enhancement factors for PNA improve at lower concentrations.

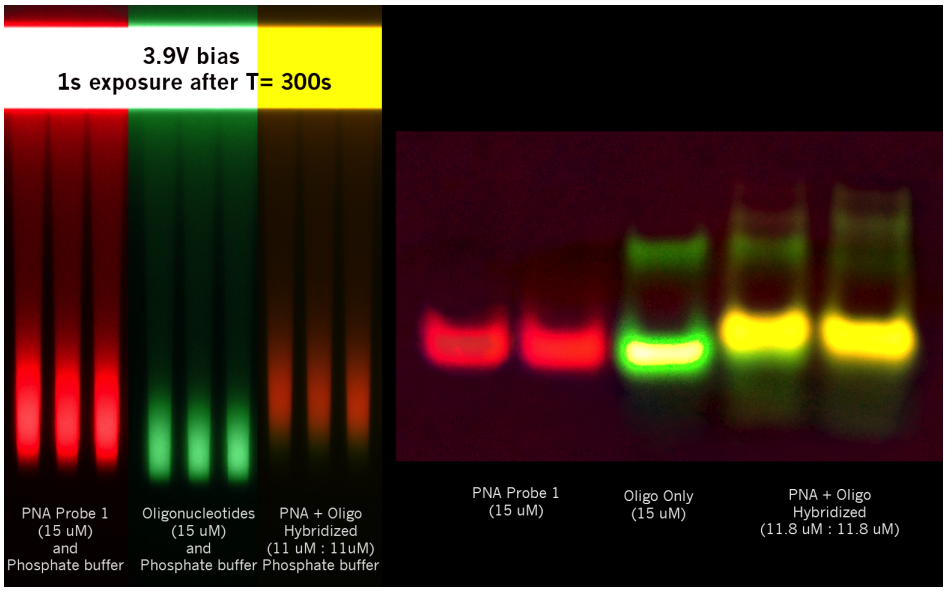

Figure 5.3-11: RIGHT: PNA probe 1, oligonucleotides and the hybrid were simultaneously focused within polyacrylamide gel. The rightmost yellow bands indicate hybridization between the red (Alexa Fluor 555 labeled PNA) and green (fluorescein 488 labelled oligonucleotides). LEFT: The same focusing experiment replicated within the nanochannel device. A slightly more pronounced focus trap position difference is visible but acheived within 300 seconds.

5.3.3 PNA:oligo Hybridization Overlap

In order to determine the quality of the PNA:oligonucleotide hybridizations, several trials were performed within the nanochannel device focusing oligo:PNA-Probe-1 hybrids and oligo:PNA-Probe-2 hybrids at 11mM:11mM concentration ratios. Images were taken with two filter cubes described earlier to isolate the fluorescein signal of the oligonucleotides from the Alexa Fluor 555 signal of PNA-probe-1 and PNA-probe-2. The 3 non-successive repetitions of the focusing data were then collected and the degree of "overlap" was calculated in order to quantify the difference made by a G-G base-pair mismatch (full sequences shown in table 5.1). The oligo:PNA-probe-1 overlap was found to be approximately 90 % while the oligo:PNA-probe-2 hybrid with the G-G base pair mismatch was found to be around 83 %. Figure 5.3-12(a) shows the average values across all trials for 30 seconds, 60 seconds and 120 seconds of focusing under a 2 volt bias. Figure 5.3-12(b) shows a superimposed profile of oligo:PNA-probe-1 focusing, and Figure 5.3-12(c) shows a superimposed profile of oligo:PNA-probe-2 focusing. The blue bar in 5.3-12(a) titled "Probe-2 Oligo (mix)" was used as a control in which the oligonucleotide PNA had minimal time to hybridize before focusing, having

experienced no heating or shaking, but rather it was just combined immediately before pipetting on to the chip. Since the degree of overlap was still rather close the Probe-2 - Oligo (hybrid) data points, we can confirm that PNA and oligonucleotides tend to hybridize spontaneously, requiring no heating or hybridization buffer.

As mentioned earlier in this chapter, Jensen et al. explored the kinetics of PNA hybridization and quantified the ΔT_m temperature of melting a hybridized complex of PNA:DNA [9]. It was found that a perfectly matched 15-mer PNA:DNA complex has a T_m of 68.5°C but a G-G mismatched pair (as is the case here) has a T_m of 53.0°C. The percent overlap evaluation used in our study could be also be considered an evaluation of stability since overlap can be interpreted as an indication of the effectiveness of PNA:oligonucletide conjugation. This can be done cheaply and easily compared to the "biacore" technique Jenson used wherein the target sequence had to be immobilized on a sensor chip. Countless types of hybridization processes could be assessed quickly and at low cost within a nanofluidic electrofocusing scheme.

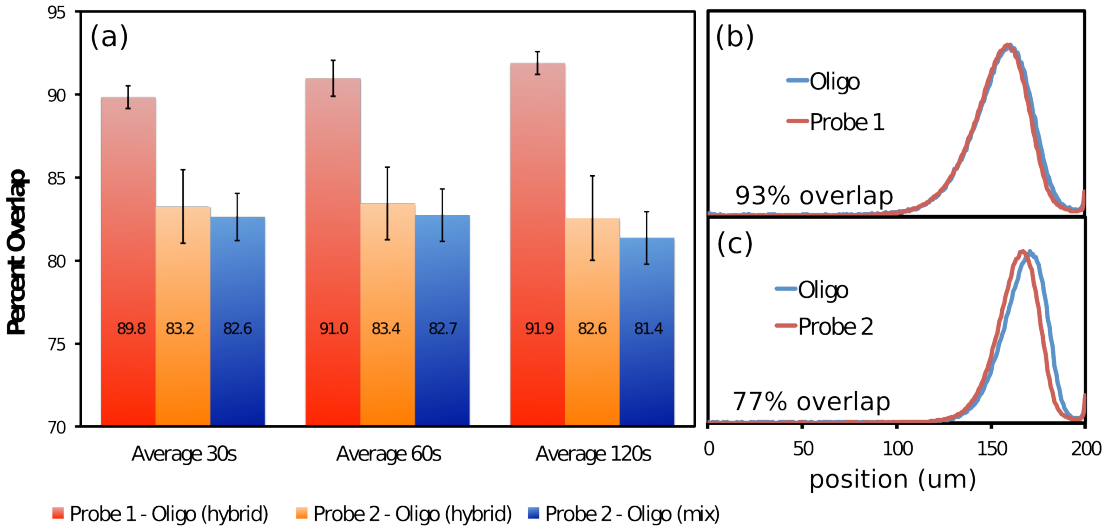

Figure 5.3-12: (a) comparison of fluorescent overlap for hybridization of matched PNA (PNA-probe-1) and oligonucleotide vs the fluorescence overlap for hybridization of single base pair unmatched PNA (PNA-Probe-2) and oligonucleotide. PNA-Probe-1 shows a consistently higher percent overlap compared to PNA-Probe-2. (b) Example of PNA probe 1 overlap (normalized). (c) Example of PNA probe 2 overlap (normalized).

5.3.4 Challenges and Future Work

We demonstrated that PNA molecules tend to bind exceptionally well with matched oligonucleotide sequences. However, PNA:ds-DNA hybridization was not as effective. Smolina and Demidov [30] reported that PNA targets located inside linear double stranded DNA (ds-DNA) is restricted to homopurin-homopyrimidine sequence motifs (limited to binding sites consisting of only purines (A and G) or only Pyrimidines (T an C)). Our PNA sequences did not consist of homopurine or homopyrimidine sequences so this may explain why the oligonucleotides successfuly hybridized but the ds-DNA did not. Smolina continues to show that by targeting ds-DNA fragments at the very termini of the DNA duplex, it is possible to alleviate the sequence restrictions. But this was not possible in our case since our DNA was sheared at random locations within an ultrasonication system. On the other hand, pseudo complementary PNA (pc-PNA) has been shown to target duplex DNA in a virtually sequence-unrestricted manner. As a result, pc-PNA can be much more readily added to the repertoire of artificial reagents that can target and invade duplex DNA without sequence limitations. Future work may involve selecting a pc-DNA sequence which can more successfully achieve duplex invasion. Furthermore, if the sequence was designed to bind in triplex formation modes, a greater mobility change could occur in the resultant DNA:PNA complex and the separation within the channel can be accentuated. Other future work can include observing PNA:DNA hybridization within the channel by introducing the strands slowly in a controlled manner such that the kinetics of hybridization can be observed. It would also be interesting to see how PNA designed to fold around the DNA to form clamps would focus within the channel.

5.4 Conclusion

This chapter explored the capability of our nanofluidic focusing scheme to detect peptide nucleic acid (PNA) hybridization with DNA. The first section was dedicated to characterizing the PNA alone in the nanochannels, ensuring that PNA can indeed be trapped within the channels. The second section showed DNA and PNA separation simultaneously within the channel. Then, to to compare the nanofluidic electrofocusing technique with conventional gel electrophoresis, PNA and DNA and hybridized PNA:oligonucleotides were analyzed through both agarose gel electrophoresis and polyacrylamide gel electrophoresis. Unfortunately, due to PNA's sequence-limitations when

binding with double stranded DNA, we could not observe PNA hybridization with double stranded Bacillus cereus DNA. However, PNA:oligonucleotide hybridization was demonstrated and the effect of a single base pair mismatch was detected by fluorescence overlap. Perfectly matched PNA:oligonucleotide hybrids formed 90% overlap while mismatched PNA:oligonucleotided hybrids formed 83% overlap.

References

[1] G. Felsenfeld, David R. Davies, and Alexander Rich. Formation of a three-stranded polynucleotide molecule. *Journal of the American Chemical Society*, 79(8):2023–2024, 1957. 92

[2] Nguyen T. Thuong and Claude Hlne. Sequence-specific recognition and modification of double-helical dna by oligonucleotides. *Angewandte Chemie International Edition in English*, 32(5):666–690, 1993. 92

[3] Stephen Neidle and Helen M. Berman. X-ray crystallographic studies of nucleic acids and nucleic acid-drug complexes. *Progress in Biophysics and Molecular Biology*, 41(0):43 – 66, 1983. 92

[4] Christoph Zimmer and Ulla Whnert. Nonintercalating dna-binding ligands: Specificity of the interaction and their use as tools in biophysical, biochemical and biological investigations of the genetic material. *Progress in Biophysics and Molecular Biology*, 47(1):31 – 112, 1986. 92

[5] P.E. Nielsen, M. Egholm, R.H. Berg, and O. Buchardt. Sequence-selective recognition of dna by strand displacement with a thymine-substituted polyamide. *Science*, 254(5037):1497–1500, 1991. 92

[6] Peter E Nielsen, Michael Egholm, et al. An introduction to peptide nucleic acid. *Current Issues in Molecular Biology*, 1(2):89–104, 1999. 93

[7] Ralph Casale, Ivar S Jensen, and Michael Egholm. Synthesis of pna oligomers by fmoc chemistry. *Peptide nucleic acids: Protocols and applications. 2nd. Wymondham: Horizon Bioscience*, pages 61–76, 2004. 93

[8] P.E. Nielsen. *Peptide Nucleic Acids: Protocols and Applications*. Horizon Bioscience. Horizon Bioscience, 2004. 93

[9] Kristine Kilsa Jensen, Henrik Orum, Peter E. Nielsen, and Bengt Norden. Kinetics for hybridization of peptide nucleic acids (pna) with dna and rna studied with the biacore technique. *Biochemistry*, 36(16):5072–5077, 1997. PMID: 9125529. 93, 112

[10] Ning Zhang and Daniel H. Apella. Advantages of peptide nucleic acids as diagnostic platforms for detection of nucleic acids in resource-limited settings. *Journal of Infectious Diseases*, 201(Supplement 1):S42–S45, 2010. 93, 94

[11] Henrik Stender, Brett Williams, and James Coull. Pna fluorescent in situ hybridization (fish) for rapid microbiology and cytogenetic analysis. In Peter E Nielsen and Daniel H. Appella, editors, *Peptide Nucleic Acids*, volume 1050 of *Methods in Molecular Biology*, pages 167–178. Humana Press, 2014. 93

[12] O. Brandt, J. Feldner, and A. Stephan et al. Pna microarrays for hybridisation of unlabelled dna samples. *Nucleic Acids Research*, 31(19):e119, 2003. 93

[13] Sheng Ye, Xingguo Liang, Yoji Yamamoto, Jing-Min Zhou, Takafumi Tomita, Hiroyuki Aburatani, and Makoto Komiyama. Simultaneous detection of multiple single nucleotide polymorphism by single-strand-specific nuclease and pna probe. *Nucleic Acids Symposium Series*, 3(1):185–186, 2003. 93

[14] Gary M Cohen. Access to diagnostics in support of hiv/aids and tuberculosis treatment in developing countries. *Aids*, 21:S81–S87, 2007. 93

[15] Jonathan K. Pokorski, Mark A. Witschi, Bethany L. Purnell, and Daniel H. Appella. (s,s)-trans-cyclopentane-constrained peptide nucleic acids. a general backbone modification that improves binding affinity and sequence specificity. *Journal of the American Chemical Society*, 126(46):15067–15073, 2004. PMID: 15548003. 94

[16] Ask Püschl, Stefano Sforza, Gerald Haaima, Otto Dahl, and Peter E Nielsen. Peptide nucleic acids (pnas) with a functional backbone. *Tetrahedron letters*, 39(26):4707–4710, 1998. 94, 98

[17] J. Lohse, O. Dahl, and P.E. Nielsen. Double duplex invasion by peptide nucleic acid: A general principle for sequence-specific targeting of double-stranded dna. *Proceedings of the National Academy of Sciences of the United States of America.*, 96(21):11804–11808, 1999. 94

[18] Konstantin I. Izvolsky, Vadim V. Demidov, Peter E. Nielsen, and Maxim D. Frank-Kamenetskii. Sequence-specific protection of duplex dna against restriction and methylation enzymes by pseudocomplementary pna. *Biochemistry*, 39(35):10908–10913, 2000. PMID: 10978178. 94

[19] Heiko Kuhn, Dmitry I. Cherny, Vadim V. Demidov, and Maxim D. Frank-Kamenetskii. Inducing and modulating anisotropic dna bends by pseudocomplementary peptide nucleic acids. *Proceedings of the National Academy of Sciences of the United States of America*, 101(20):7548–7553, 2004. xviii, 94, 95

[20] J.D. Watson and F.H. Crick. Molecular structure of nucleic acids: A structure for deoxyribose nucleic acid. *Nature*, 171:737738, 1953. 95

[21] K. Hoogsteen. The crystal and molecular structure of a hydrogen-bonded complex between 1-methylthymine and 9-methyladenine. *Acta Crystallographica*, 16(9):907–916, Sep 1963. 96

[22] Guliang Wang and Karen M. Vasquez. Naturally occurring h-dna-forming sequences are mutagenic in mammalian cells. *Proceedings of the National Academy of Sciences of the United States of America*, 101(37):13448–13453, 2004. 96

[23] via Wikimedia Commons InfoCan (Own work) [Public domain]. Hoogsteen: http://commons.wikimedia.org/wiki/fileaccessed: January 2015. xviii, 97

[24] Bob Somers, Alexey Merz, and Suzanne Kennedy. Oligo calc: Oligonucleotide properties calculator. http://www.basic. northwestern.edu/biotools/oligocalc.html#helpmw; accessed: January 2015. 101

[25] Wen-Tso Liu, Andrei D. Mirzabekov, and David A. Stahl. Optimization of an oligonucleotide microchip for microbial identification studies: a non-equilibrium dissociation approach. *Environmental Microbiology*, 3(10):619–629, 2001. 101

[26] A Loy, F Maixner, M Wagner, and M Horn. probebase - an online resource for rrna-targeted oligonucleotide probes: new features. *Nucleic Acids Res.*, 35:D800–D804, 2007. 101

[27] Invitrogen. Molecular probes, http://tools.lifetechnologies.com /content/sfs /manuals/x21422.pdf, August 2005. 102

[28] Jian Lin Yin, Nicholas A. Shackel, Amany Zekry, Peter H. McGuinness, Craig Richards, Karien Van Der Putten, Geoffrey W. McCaughan, Josette M. Eri, and

G Alex Bishop2. Real-time reverse transcriptasepolymerase chain reaction (rtpcr) for measurement of cytokine and growth factor mrna expression with fluorogenic probes or sybr green i. *Immunology and Cell Biology*, 79:213–221, 2001. 104

[29] T.B. Morison, J.J. Weis, and C.T. Wittwer. Quantification of low-copy transcripts by continuous sybr green i monitoring during amplification. *Biotechniques*, 24(6):954–958, 960, 962, 1998. 104

[30] Irina V. Smolina, Vadim V. Demidov, Viatcheslav A. Soldatenkov, Sergey G. Chasovskikh, and Maxim D. Frank-Kamenetskii. End invasion of peptide nucleic acids (pnas) with mixed-base composition into linear dna duplexes. *Nucleic Acids Research*, 33(17):e146, 2005. 113

5.5 Acknowledgement

This work was supported by the Australian Research Council (DP110102207). Microchannel etching was performed at the University of South Australia node of the Australian National Fabrication Facility, established under the NCRIS scheme.

6

Conclusions

The introductory chapter presented justification for the advancement of nanofluidic methods of biomolecular analysis as well as motivation for this thesis project. Given the benefits of working with smaller volumes of reagents, lower costs of processing and faster turnaround times, the potential applications of nanofluidics and microfluidics for biomolecular analysis, diagnostics and forensics cannot be ignored. A brief summary of the various possible forms of gradient counterflow electrofocusing methods was provided, placing the methods central to this thesis – pH gradient electrofocusing in chapter 3, and conductivity gradient electrofocussing in chapter 4 and 5 – into context with other gradient classifications such as chromatographic velocity focusing, current gradient focusing and temperature gradient focusing.

The theory chapter covered the fundamental principles pertinent to this thesis. First, the basic assumptions required for a theoretical treatment of the nanofluidic regime were explicitly formulated: fluids are assumed to be a continuum rather than discrete molecular units, fluids are assumed to be incompressible, fluids are assumed to flow in a laminar mode, the viscosity of fluids is independent of the shear rate (fluids are Newtonian), particles and macromolecules within the fluid are approximated as spherical bodies. Then the physics behind continuum hydrodynamics was

reviewed, reasserting the importance of mass conservation and momentum conservation and outlining the conventions of shear, and stress tensor relations in the derivation of the Navier-Stokes equation (for liquid flow problems) and Nernst-Plank equations (for electrokinetic problems). The characteristic parameters of flow, with emphasis on the Reynolds number and the Peclet number, were described and their usefulness in assessing nanofluidic flows were explained. The mechanisms behind surface charge accumulation were addressed, leading to the concept of the interfacial double layer of ions between glass surfaces and electrolytes. The consequence of charge separation near the surface of glass led to an exploration of the electrokinetic phenomena of electroosmosis and liquid slip. It was explained how these mechanisms are accentuated at the confined length scales of nanofluidic geometries. By the end of the chapter, it was clear that the motion is not merely explainable by the interactions of external/axial fields and the solvent, but rather as an complex coupling phenomena between the fluid, ions, and the electric double layer (EDL). The transport of analyte ions must be determined not just by the bulk ion mobility but as a function of ion valence, EDL thickness, and surface charge density.

Nanochannel geometry devices have advantages over larger scale devices particularly when they are used in applications that exploit the large surface to volume ratio unique to nanochannels. As dimensions of a device decrease, the surface to volume ratio increases, and the molecules within the solution experience much more frequent, and increasingly important interactions with the nanochannel walls. This can result in effects unique to various surfaces, and it could result in undesirable effects such as adsorption. Nanofluidics also exhibits superiority over microfluidics, particularly when the double layer of opposite walls of a nanochannel overlap, resulting in a unique level of control over individual molecules within the channel. In this thesis, the nanochannel regime was central for the electrofocusing phenomenon. Particularly, we required that the Peclet numbers of the flow are low such that the diffusion rate of molecules from one wall to another greatly exceeded the convection rate along the axial direction of the nanochannel, thus permitting – for conceptual purposes – the simplification of a complicated 3 dimensional problem into a 1 dimensional flow problem. In this 1 dimensional flow problem, the counteracting electrokinetic forces could form biomolecular traps.

In chapter 3 we demonstrated a method to focus proteins within the nanofluidic device by inducing a pH gradient along nannochannels. Counteracting electroosmosis and electrophoresis forces created a trap at unique locations for R-phycoerythrin (RPE) and Dylight labelled streptavidin (Dyl-Strep) which depended upon their respective mobilities (charge:mass ratio). While electrophoresis acted on the individual

protein molecule charge which varied along the channel depending on the local pH value, electroosmosis provided a Stokes drag flow in the opposite direction which could be approximated as constant due to the conservation of bulk flow at any point along the channel. At unique positions along the channel, the electrophoretic force on a specific protein reaches equilibrium with the counteracting electro-osmotic force and a trap is formed. By using applied voltages between 0.4 and 1.5 V, concentration enhancement factors (ratio between the focus band fluorescence intensity and the microchannel source fluorescence intensity) of over 380 were achieved within 5 minutes. By varying the buffer pH between 2.7 and 7.2 at either microchannel end, focus band shape and concentration enhancement (CE) factors could be modified. For RPE, a pH span of 4.5 (pH 2.7 to 7.2) was found to yield the narrowest band of 5.1 μm, while a span of 2.4 (pH 2.7 to 5.1) produced a wider band of 12.3 μm. The maximum CE factors achieved for RPE and Dyl-Strep were 385 and 107 respectively. In this chapter, the proteins were focused individually, each requiring separate trials, but the technique could conceivably be used to separate, and concentrate multiple proteins simultaneously by their various mobility-pH dependency relationships.

In chapter 4, the conductivity gradient electrofocusing method was used to create the trapping condition within the nanochannel. Counteracting electroosmosis and electrophoresis forces behaved in a similar manner to the forces acting in the pH gradient method except the cause of the trapping was not due to the charge-pH dependency of molecules but rather, the modulation of the local electric field along the channel due to an induced gradient in conductivity. Sheared 150 bp Bacillus cereus DNA was focused within the nanochannel device and the trapping concentration and band integrity/sharpness was characterized for various microchannel analyte supply concentrations and bias voltages. Introducing higher DNA concentrations through the microchannels resulted in higher concentrations of DNA at the trapping position and faster DNA accumulation. However, the trap focus band was found to be widen at higher initial concentrations. This was considered a potentially undesirable effect if attempting to separate multiple species within the channel simultaneously since there may be a greater band overlap with wide focusing molecules and thus poorer resolution of bands. We found that higher voltages resulted in faster DNA accumulation within the trap. The simultaneous separation and concentration of DNA and protein was demonstrated by introducing Bacillus cereus DNA and protein R-phycoerythrin (RPE) together into the device. Separation and concentration was observed yielding band widths of 22.6 μm and 4.5 μm for DNA and RPE respectively. The peak separation between DNA and RPE was 15.0 μm. The peak separation resolution quality

was quantified as $R_s = 1.1$ indicating slight overlap, but distinct observable peaks were visible. This result serves as a proof of principle for the simultaneous DNA/protein concentration and separation capability of the nanodevice. Perhaps in the future, the lysed contents of a cell nucleus can be analysed with high-fidelity non-destructive gel-free nanochannel electrofocusing methods such as those presented in this device, separating DNA, proteins and RNA simultaneously.

In chapter 5, conductivity gradient electrofocusing was applied as in chapter 4 in order to detect hybridization between 18 base pair ALEXA fluor 555 labelled peptide nucleic acid probes (PNA) and DNA. Both, sheared Bacillus cereus DNA and 18 base-pair complementary oligonucleotides (labelled with fluorescein 488) were hybridized with PNA and analyzed through gel electrophoresis. Two modes of gel electrophoresis (agarose and polyacrylamide) were assessed in comparison with conductivity gradient electrofocusing by their capability to detect hybridization. However, only the PNA:oligonucletide hybridizations could be confirmed within either, gel electrophoresis or nanochannel focusing methods. A single G-G base-pair mismatched PNA probe was hybridized with an otherwise complementary oligonucleotide and compared with fully complementary PNA:oligonucleotide hybridizations. By observing the fluorescence overlap of each hybrid, it was possible to detect the base pair mismatch within the hybridization. Fully hybridized complementary PNA:oligonucleotide hybrids resulted in a 90% overlap of fluorescence and single base-pair mismatch PNA:oligonucleotide hybrids resulted in 83% overlap. This suggested that the electrofocusing approach could potentially be a useful measure for quantifying the degree of hybridization and detecting sequence mismatches between complementary sequence pairs.

The work in this thesis project explored a specific set of phenomena unique to the nanoscale fluid transport regime. While nanochannel electrofocusing accomplishes many of the same tasks that were possible with conventional techniques such as gel electrophoresis, isoelectric focusing and capillary electrophoresis, nanofluidic electrofocusing does so without the need for gel matrices, ampholytes or high voltages. The low volumes and rapid trapping inherent to nanofluidic electrofocusing offers significant cost savings and the "continuous microchannel analyte supply flow" perpendicular to the nanochannels may permit continuous focusing of disease biomarkers that are of too low concentration to detect with other methods without selective preconcentration techniques. In future work, this nanofluidic device can be used to accelerate reaction rates by focusing the reactants within the nanochannel, or it could be used to detect molecular reactions such as the hybridization of PNA:DNA explored in chapter 5.

As a promising future outlook, the principles behind gradient electrofocusing explored here could be applied in practice as a module within a larger integrated lab-on-a-chip device and developed as part of a novel, consumer facing, rapid diagnostics tool.

A Appendix

A.1 Nanofluidic Device Fabrication

The wafers used in Chapters 4 and 5 began as clean 3-inch diameter, P/boron doped silicon substrate wafers of <100> crystallographic orientation with a 50 nm thick SiO_2 layer pre-grown on the active side. The wafers were purchased from *Micro Materials and Research Consumables* (M.M.R.C Pty. Ltd.). The wafers then underwent a two phase photolithographic process in order to fabricate the microchannels and nanochannels forming 6 nanochannel devices per wafer, which are then diced into individual devices on rectangular chips.

Note that Chapter 3 describes fused silica bonded on top of fused silica to produce the devices. In order to etch the microchannels, SU-8 was patterned on to the fused silica and sent to the Australian National Fabrication Facility at the university of South Australia to etch the microchannels to a depth of 12.5 μm. The SU-8 was removed by baking at 900 °C for 5 hours. The rest of the procedure is the same as outlined below for silicon substrate wafers, continuing from A.2.4 (step 4).

Figure A.1-1 illustrates the general steps taken create the nanofluidic devices. Note that the microchannels in the figure run out of the plane of the page so they cannot be seen clearly. It may appear as though the sandblasted holes go right through the

nanochannels, but this is only done in the image for clarity.

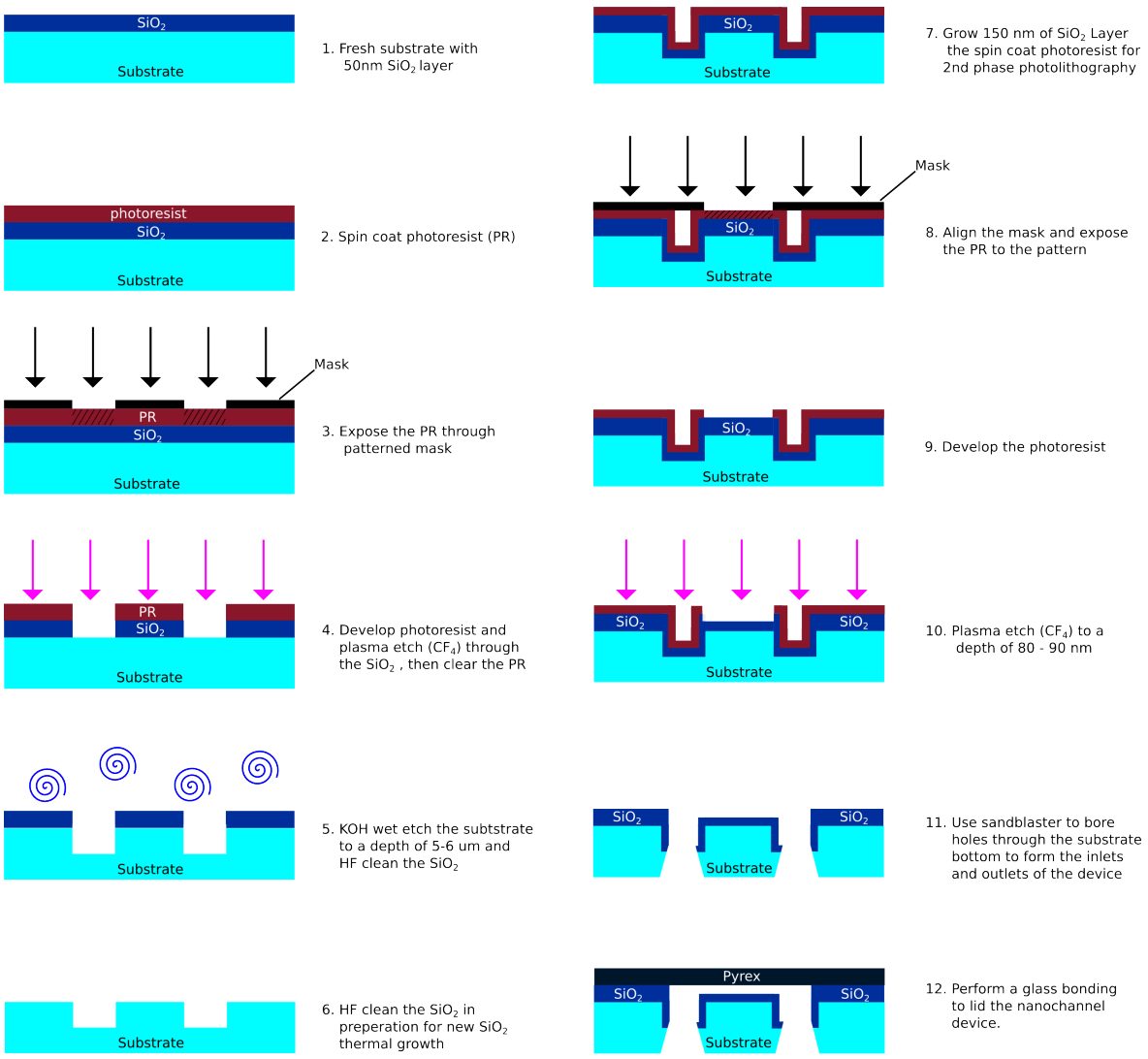

FIGURE A.1-1: Cross-sectional illustration of the fabrication steps. The microchannels are running orthogonal to the page and may not be seen as channels, but rather appear as wells. The nanochannel in between is the focus of the diagram.

A.2 Phase 1: Microchannel Photolithography

A.2.1 Step 1: Spin coating AZ-1518 photoresist and exposure

The first step of the fabrication is a positive photoresist spin coating, followed by an photolithography exposure.

Basic AZ-1518 Resist spin-coat Recipe

1. **Prebake** clean wafer for 5 min on 110 °C hot plate
2. Spin **HMDS** at 4000 rpm for 40 s
3. Spin **AZ-1518** at 4000 rpm for 40 s. Gives thickness of 1.2 - 2.0 μm
4. **Softbake** 60 s on foil covered 90 ^{o}C hot plate
5. **Exposure**: 10 seconds using 360 LP set up, Power = 9 mJ/cm^2.
6. **Develop** in 2.4% TMAH solutions for 45 seconds with agitation.
7. Immerse in water and rinse thoroughly.
8. **Hardbake**: 3 minutes on 95 ^{o}C hot plate. ...

The positive AZ-1518 photoresist used in this procedure was Purchased from Microchem, MA, USA. Prior to spin coating the wafers with AZ-1518, each wafer was treated with Hexamethyldisilazane (HMDS) (Purchased from Sigma Aldrich, Castle Hill NSW, Australia) in order to promote adhesion with the subsequent layer of photoresist. Coated and patterned wafers were "developed" using Tetramethylammonium hydroxide (TMAH) at 2.4% concentration.

A.2.2 Step 2: Plasma Etch

CF_4 Plasma etch the patterned and developed wafers until the pre-grown SiO_2 layer is completely removed from the developed pattern sections of the wafer. We used the March PX-250 plasma asher in our fabrication process.

1. With the wafer inside, **vacuum pump** the chamber to below 280 mTorr before switching on the O_2 and CF_4.
2. Turn on the gasses O_2 and CF_4 at flow rates described in the Plasma Etch protocol table below (Table A.1)
3. Wait for pressure to decrease back down to under 300 mTorr and then turn on the plasma. Note: In our case, the wafers were kept under plasma for no longer than 4 minutes because the etch rate tended to change unpredictably due to the temperature increase.

4. (optional) After first etch, use a swab with acetone followed by a swab with isopropyl on a small unused section of microchannel depth and use a profilometer to confirm the etch rate before the next plasma etch phase.
5. Typically, a total etch time of 6 minutes (two etch phases) should achieve a clearing of oxide according to Table A.1 (experimentally determined).

The etch protocol below indicates how long an etch process must take in order to expect the SiO_2 to be completely removed. Note from Table A.1, that the photoresist etches much faster than the thermal oxide (10 times faster). Therefore, it is important to have a thick enough photoresist protecting the non-patterned sections of the substrate to prevent its depletion before the oxide is successfully removed.

Pressure:	300 mTorr	
Gas 1:	2% MFC1 = 0.84 sccm O_2	
Gas 2:	9% MFC2 = 3.78 sccm CF_4	
Power	150 W	
Rates:	Thermal Oxide on Silicon:	11 nm/min
	Pyrex:	6 nm/min
	Photoresist:	100 nm/min

TABLE A.1: Plasma Etching Protocol 1

A.2.3 Step 3: KOH etching of ⟨100⟩ Si

Once the oxide layer is removed, the silicon must be etched to the desired micro-channel depth of 5-6 μm. To accomplish this, an anisotropic KOH wet etch is performed. For an effective etch, it is important to heat the KOH solution to increase the silicon etch rate.

The recipe for KOH etch solution is as follows:

- 1000 mL Water
- 250 mL Isopropyl Alcohol
- 204.4 g of KOH

Or if less volume is needed, make 500mL of water and 204.4 g of KOH. When solid KOH is dissolved in water, heat is released. Later, mix 150 mL of water and 75mL of isopropyl

alcohol.

Place solution in beaker and heat the beaker with. Place Temperature probe in water bath and bring the solution to $> 65°$C to achieve a reasonable etch rate. The etchant will typically be 5 degrees cooler at the top of the beaker than at the bottom. The channels should be etched leaving the $\langle 111 \rangle$ plane of silicon un-etched giving a triangular channel wall that is 1 unit over and $\sqrt{2}$ units down.

- at 80 ^{o}C etch rate is 86 μm/hour, or 1.4 μm/min
- at 70 ^{o}C etch rate is 50 μm/hour, or 0.8 μm/min
- at 60 ^{o}C etch rate is 28 μm/hour, or 0.47 μm/min
- at 50 ^{o}C etch rate is 15 μm/hour, or 0.25 μm/min

A.2.4 Step 4: Preparation for boring holes through the substrate with an SU-8 protective coating

In order to create the holes that allow capillary tubes to feed the constant flow analyte to the nanochannel structures, we chose to sandblast small openings through the substrate. However, in order to avoid causing the devices to be ablated by the sandblasting as well, it was important to spin a thick protective layer of SU-8 GM-1060 negative photoresist on the wafer. However before coating with SU-8, spin coat the wafer with HMDS and positive photoresist as described in section A.2.1. This is done in order to enable us to remove the SU-8 resist easily with acetone after the process.

$40\mu m$ **SU-8 GM1060**

- Prebake 5 min on 120 ^{o}C hot plate
- (optional in order to make removal easy) Spin on HMDS and AZ-1518 as described in steps 1-3 of section A.2.1
- Spin GM1060 SU-8 at 550 rpm for 60 seconds ($4 \times 15s$). Use razor blade on outside edge at the end of spin to reduce edge bead.
- Softbake: ramp at 2 ^{o}C/min from 55 to 70 ^{o}C on a foil covered hot plate. Hold for 7 minutes.
- Ramp to 100 ^{o}C and hold for 40 minutes. Leave on hotplate while plate cools to 45^{o}C.

Note: always use temperature ramps

After the SU-8 is coated, place tape over top of the surface and mark x's where the vias will be bored with the sandblaster in the next step.

A.2.5 Step 5: Sandblasting

The holes through the substrate were pattered with a miniature tabletop sandblaster ("PrepStart Kit Air Abrasion Cavity Prep unit" and "MicroCab Plus Self Contained Dust Cabinet" Danville Materials, California, USA) using Comco inc. "Precision 'C' Powder, 50 um aluminium oxide" material in the abrasives compartment. Each hole should take a few seconds to bore through [1][2].

After the sandblasting is completed, use acetone to dislodge the SU-8 and tape together from the wafers. (IMPORTANT: be very careful removing the tape because the wafers are very fragile after having holes sandblasted.)

A.3 Phase 2: Nanochannel Photolithography

Before performing photolithography again to form the nanochannels between the microchannels a new thermal oxide must be grown at 1000 °C for $>$ 6 hours until a 150 nm oxide thickness is achieved. In our case, we sent the wafers to University of New South Wales (UNSW) for this process.

A.3.1 Step 1: Spin coating AZ-1518 photoresist and exposure

This procedure is similar to the positive resist coating in the previous phase except it is important to carefully match the alignment marks during the exposure step.

1. **Prebake** clean wafer for 5 min on 110 °C hot plate
2. Spin **HMDS** at 4000 rpm for 40 s
3. Spin **AZ-1518** at 4000 rpm for 40 s. Gives thickness of 1.2 - 2.0 μm
4. **Softbake** 60 s on foil covered 90 ^{o}C hot plate
5. Align the pattern such as to set the alignment marks precisely so that the nanochannels extend to reach both of the perpendicular microchannels.
6. **Exposure**: 10 seconds using 360 LP set up, Power = 9 mJ/cm^2.
7. **Develop** in 2.4% TMAH solutions for 45 seconds with agitation.
8. Immerse in water and rinse thoroughly.
9. **Hardbake**: 3 minutes on 95 ^{o}C hot plate. ...

A.3.2 Step 2: Plasma etching to form the nanochannels

Unlike in phase 1 plasma etch, we are NOT etching completely through the silicon oxide layer. Instead we are carefully timing the plasma etch to create a specific nanochannel depth between 80-100 nm. Also, in this procedure, the oxygen flow is set to 0 to minimize the photoresist etching so that the CF_4 can etch deep enough through the silicon oxide. 4 minute cycles are recommended to minimize temperature effects as in the previous plasma etch step. Three cycles should be enough to reach the desired depth. It is encouraged to test the etch depth at each cycle with the swab method mentioned earlier.

Pressure:	300 mTorr	
Gas 1:	0% MFC1 = 0 sccm O_2	
Gas 2:	9% MFC2 = 3.78 sccm CF_4	
Power	150 W	
Rates:	Thermal Oxide on Silicon:	11 nm/min
	Pyrex:	6 nm/min
	Photoresist:	100 nm/min

Table A.2: Plasma Etching Protocol 2

A.3.3 Step 3: Glass bonding via reverse RCA clean

The final fabrication step is to place a pyrex lid on top of the devices to create the channel seals. This is performed by glass cleaning and bonding procedure called "RCA Clean"

1. Heat each of the baths described in Table A.3 to 65-70 ^oC.
2. One by one, immerse silicon and 7740 pyrex pieces, in RCA 2 for 5 minutes then rinse with water.
3. Immerse wafer in RCA 1 for 5 minutes then rinse with water.
4. If performing this with many wafers, proceed in an assembly line manner, i.e., as one wafer leaves RCA 2 bath, move it to the next bath while immersing the next wafer into RCA 2, etc.
5. Once two cleaned wafers, one silicon, one pyrex, are ready, dry every surface with an N_2 gun and bring them into tight contact. The surfaces should spontaneously.

6. Anneal at as high a temperature as possible. Currently using 350^o C for 12 hours. However, make sure to ramp the temperature slowly, otherwise the wafers will shatter.

RCA 2	1 part 37% HCl	12.5 mL
	1 part 30% H_2O_2	12.5mL
	6 parts water	75 mL
RCA 1	1 part 29% NH_4OH	14.3 mL
	1 part 30% H_2O_2	14.3 mL
	5 parts water	71 mL

TABLE A.3: Reverse RCA Clean Recipe

A.3.4 Step 4: Wafer dicing procedure

Wafer dicing was performed to separate the individual devices from the wafer into individual chips of 76 by 76 mm dimension.

- Apply tape to top surface of the wafer for protection
- Heat dicing wax and apply it to dicing chuck and bottom of wafer to adhere the wafer to the dicing chuck as shown in Figure A.3-2.
- Set width of cut to 76 mm apart adjusting for blade width (usually 0.3 mm). In our case 7.5 cm dicing widths were appropriate.
- Manually cut the perpendicular slices (length of the dicing isn't as critical since the chuck will permit longer chips up to 18 mm so long as the through-holes are aligned at the appropriate edge of the chip)
- Remove tape and clean resist from each individual chip.

Once the chips are complete, they should should appear under magnification as shown in Figure A.3-3. After using the chip, flush the channels with deionized water and store the chips in water. If the channels get clogged with protein or DNA, it is possible to flood the channel with 1M NaOH to clean out the debris.

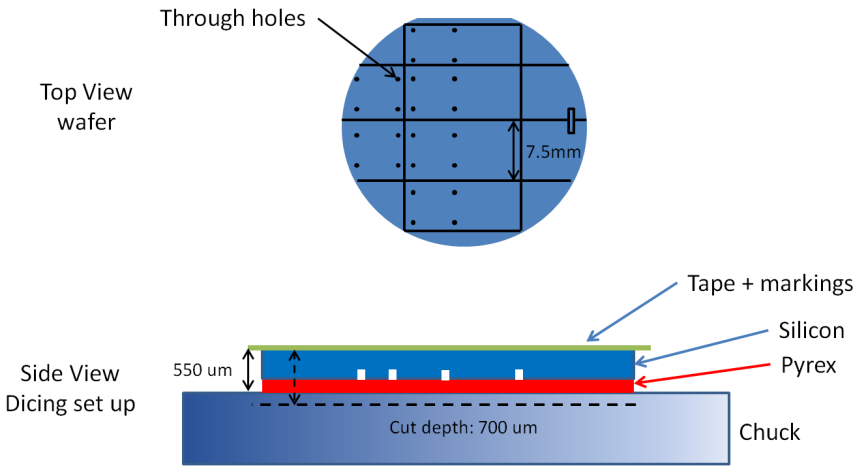

Figure A.3-2: Dicing diagram. The through-holes represent the location of the fluid entry and exit terminals. These can be used as a guide for alignement of the dicing blade.

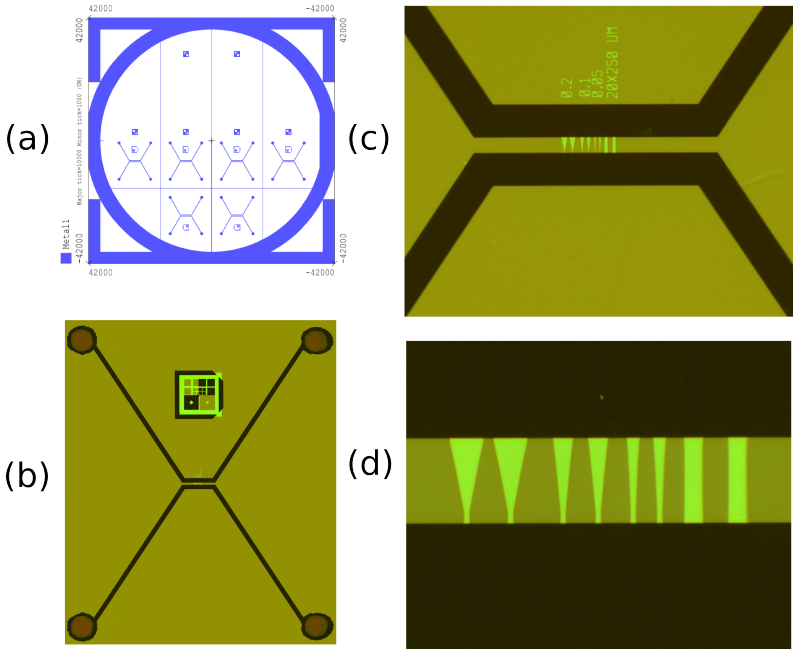

Figure A.3-3: (a) image of the full wafer design. (b) microscope image of a single nanofluidic device chip at 2x magnification. (c) 20x magnification. (d) 40x magnification.

A.4 Bacillus Cereus DNA Extraction Procedure

A standard procedure was used to extract bacillus cereus DNA extraction with the assistance of Dr. Martin Ostrowski (Figure A.4-4).

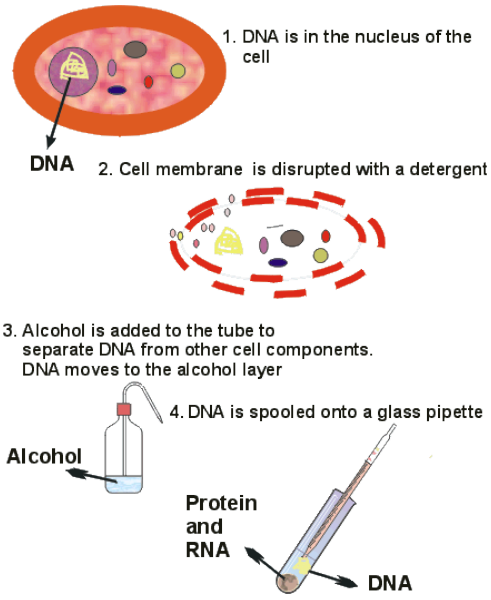

FIGURE A.4-4: Basic illustration of DNA extraction performed in University of Macquarie, Biology PC2 Lab [3].

A.4.1 Bacillus cereus shearing

After extraction, the Bacillus Cereus DNA is still too long to be flowed through the nanochannel device so it was sent to the University of New South Wales for shearing in a Covaris E220 Ultrasonicator. The target length for the DNA strands was approximately 150 bp.

The Standard protocol was used for DNA shearing using microTUBEs with minor modifications because the target length was not achieved initially (Figure A.4-5). The settings were as follows: 10% Duty Cycle, 5 intensity, 200 cycles per burst, and 600 seconds total shearing duration. The DNA was aliquoted into microTUBEs in 130μl volumes in a concentration of 120 ng/μl (found by Qubit fluorometer analysis).

After shearing, an Agilent Bioanalyzer 2100 was used to determine the resultant size distribution shown in A.4-6. The size was confirmed to be a distribution spanning between 50 - 250 bp and peaking at 150 bp.

PROTOCOL Covaris™

TITLE: DNA Shearing with microTUBEs (<1.5kb fragments)

Summary of Operating Conditions:

Target Base Pair (Peak)	150	200	300	400	500	800	1000	1500
Duty Cycle	10%	10%	10%	10%	5%	5%	5%	2%
Intensity	5	5	4	4	3	3	3	4
Cycles per Burst	200	200	200	200	200	200	200	200
Time (seconds)	430	180	80	55	80	50	40	15

Temperature (water bath)	6-8°C
Power mode	Frequency Sweeping
Degassing mode	Continuous
Volume	130µl
Buffer	Tris EDTA, pH 8.0
DNA mass	<5µg
Starting material	> 50kb
Water level (FILL/RUN)	S2 – level 12 E210 – level 6
AFA Intensifier	**Yes**

Figure A.4-5: The Covaris E220 settings for target base pair size of 150bp was applied for 600 seconds instead of 430s.

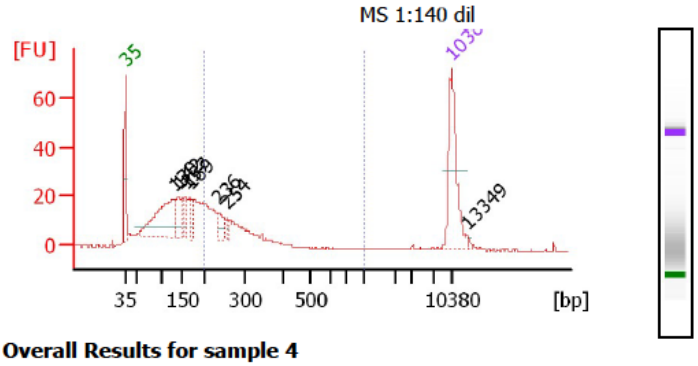

Overall Results for sample 4

Number of peaks found:	7
Noise:	0.2
Corr. Area 1:	217.1

Region table for sample 4

Figure A.4-6: Bacillus Cereus base pair length analysis using the Agilent Bioanalyzer 2100 after shearing within the Covaris E220. The size was confirmed to be a distribution spanning between 50 - 250 bp and peaking at 150 bp.

A.5 Preparation of PNA probe to bind with DNA

For PNA hybridization experiments, two sequences of 18-mer PNA primers were purchased from *Life Technologies Australia Pty. Ltd* targeting the 16S ribosomal RNA sequence from Bacillus cereus [4]. The specific sequence was selected after having been evaluated for primer specificity and sufficient binding affinity [5]. Both primers were labelled with ALEXA 555 [6] at the 5' end. The primers were provided as 200 nMol quantity, 1 mM concentrations which were purified with high performance liquid chromatography (HPLC). PNA-Probe-1 was designed to match the target sequence of DNA precisely while PNA-Probe-2 had one mismatched G-G base pair
PNA-Probe-1 Sequence - TG CGG TT**C** AAA ATG TTA T
PNA-Probe-2 Sequence - TG CGG TT**G** AAA ATG TTA T

A.6 Citric Acid Buffer recipe

(a)

pH	0.1 M citric acid (µL)	0.2 M Na2HPO4 (µL)	Resultant pH	Conductivity mS/cm	Added NaCl 3M (uL)	Added NaCl 0.3M (uL)	Resultant Cond mS/cm
2.6	446	55	2.74	1.183	30	35	4.57
3	397	103	3.06	1.345	30	24	4.62
3.6	339	161	3.65	1.759	22	55	4.62
4	307	193	4.09	2.09	20	53	4.6
4.6	266	234	4.66	2.47	23	0	4.6
5	243	258	5.22	2.73	20	0	4.64
5.6	210	290	5.76	3.07	15	23	4.62
6	184	316	6.2	3.41	8	38	4.6
6.4	154	346	6.55	3.64	8	30	4.59
7	88	412	7.11	4.58	0	0	4.58

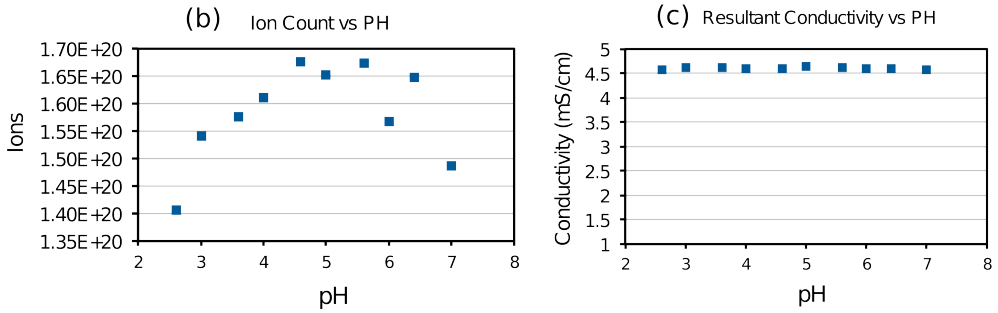

FIGURE A.6-7: (a) Recipe for citric acid buffers (b) Ion count vs pH of resultant buffers (c) Conductivity vs pH of resultant buffers

A.7 Gel Electrophoresis Running Buffer Recipes

10x TBE Running buffer (1L) Recipe

Tris base	107.8 g	⇒ 890 mM
Boric acid	55.0 g	⇒ 890 mM
EDTA	5.8 g	⇒ 20 mM
diH_2O	to 1 L	

do not adjust the pH (∼ pH 8.3)

Loading Dye (Sample Buffer) Recipe

Glycerol	60%
Tris	10 mM
EDTA	60 mM
Bromophenol blue	0.2%
Cresol red	0.2%

adjust the pH to (∼ pH 8.3)

1% Agarose gel Recipe

1x TAE	60 mL
Agarose Powder	0.6 g

Microwave for 2 min in phases
until all powder is dissolved.
Pour the fluid into chamber and let cool

A.8 Fluorescent Labels and Proteins

Name	Excitation (nm)	Emission (nm)
Fluorescein	480	525
SYBR Green	497	520
DyLight 488	493	518
R-phycoerythrin	480, 545, 565	578
Alexa Fluor 555	555	565

Table A.4: Fluorophore excitation and emission wavelengths.

SYBR green [7] was supplied as a 10,000x solution in dimethylsulfoxide (DMSO). One ml of solution prepares 10 litres of Staining Solution, sufficient for 100 mini gels. For our applications, we diluted the 10,000x solution 2μL into 200μL TBE buffer (89 mM Tris base, 89 mM boric acid, and 1 mM EDTA, pH 8.0). Afterwards, 3.2μL was found to be sufficient for reasonable brightness within a 1mL of vial of analyte (phosphate buffer or citric acid buffer) before using.

When running multiple fluorophores in the same trial, in order to detect the fluorophores at the top section of Figure A.4 (fluorescein, SYBR Green and DyLight 488), the red emissions of Alexa Fluor or R-phycoerythrin emissiones were blocked out by a filter cube with a single band excitation filter passing between 475 and 497 nm and an emission filter passing only the wavelengths within the region of 520 nm A.8-8.

the fluorescence was imaging performed in chapter 3,4, and 5 were through a Leica DM-IRB microscope [8]

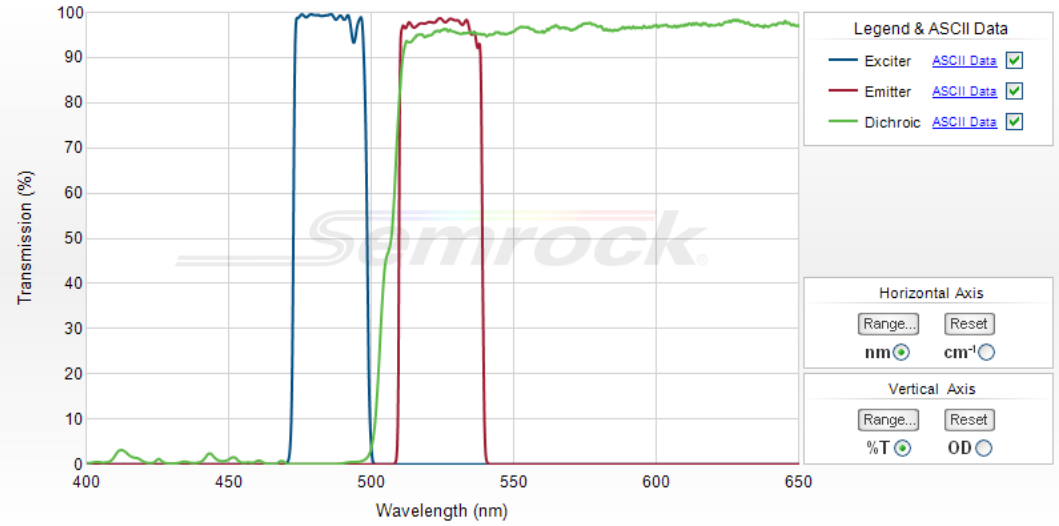

FIGURE A.8-8: Filter cube band pass excitation and emission specifications.

A.9 Compact Form Cartesian Notation

For brevity, some equations and tensors in the theory chapter were represented in a condensed Einstein's index notation, whereby instead of writing out a large cumbersome matrix, indices may be used to indicate the summation of components. Supposing

a vector $\mathbf{a}$ of n dimensions.

$$\mathbf{a} = \begin{pmatrix} a_1 \\ a_2 \\ a_3 \\ \vdots \\ n \end{pmatrix} \tag{A.1}$$

we can write $\mathbf{a}$ in terms of $\mathbf{e}$ component vectors.

$$\mathbf{a} = a_1\mathbf{e}_1 + a_2\mathbf{e}_2 + a_3\mathbf{e}_3 + \ldots + a_n\mathbf{e}_n \equiv \sum_{i=1}^{n} a_i\mathbf{e}_i \tag{A.2}$$

Where

$$\mathbf{e}_1 = \begin{pmatrix} 1 \\ 0 \\ 0 \\ \vdots \\ n \end{pmatrix}, \qquad \mathbf{e}_2 = \begin{pmatrix} 0 \\ 1 \\ 0 \\ \vdots \\ n \end{pmatrix}, \qquad \mathbf{e}_3 = \begin{pmatrix} 0 \\ 0 \\ 1 \\ \vdots \\ n \end{pmatrix} \tag{A.3}$$

The standard Einstein notation can suppresses the summation sign within the equation for notational conciseness like so:

$$\mathbf{a} = \sum_{i=1}^{n} a_i\mathbf{e}_i \equiv a_i\mathbf{e}_i \tag{A.4}$$

For 3 dimensions, $n = 3$, which is the case for most equations in the previous chapters.

A dyadic tensor (2nd order tensor) in 3 dimensions defined as

$$\mathbf{T} = \begin{pmatrix} T_{xx} & T_{xy} & T_{xz} \\ T_{yx} & T_{yy} & T_{yz} \\ T_{zx} & T_{zy} & T_{zz} \end{pmatrix} \tag{A.5}$$

Can, likewise, be written in compact notation with two indices.

$$\begin{aligned} \mathbf{T} = {} & T_{xx}\mathbf{e}_{xx} + T_{xy}\mathbf{e}_{xy} + T_{xz}\mathbf{e}_{xz} \\ & + T_{yx}\mathbf{e}_{yx} + T_{yy}\mathbf{e}_{yy} + T_{yz}\mathbf{e}_{yz} \\ & + T_{zx}\mathbf{e}_{zx} + T_{zy}\mathbf{e}_{zy} + T_{zz}\mathbf{e}_{zz} \end{aligned} \tag{A.6}$$

similarly to how a first order tensor can be condensed in equation A.4, $\mathbf{T}$ can be

written as:

$$\mathbf{T} = \sum_{ij} T_{ij} e_i \otimes e_j \equiv T_{ij}\mathbf{e}_{ij} \tag{A.7}$$

Where $\otimes$ is the tensor product, and it is analogous to vector multiplication in the sense that it can be written as a linear combination of tensor basis: $e_x \otimes e_y \equiv e_{xy}$, where the right side is an abbreviation of the tensor product.

In physics, a common usage of tensors is "stimulus-response". For example, traction force may often be seen as some applied vector, $\mathbf{u}$, acting upon the stress tensor of an object or material:

$$\begin{pmatrix} \sigma_x \\ \sigma_y \\ \sigma_z \end{pmatrix} = \begin{pmatrix} T_{xx} & T_{xy} & T_{xz} \\ T_{yx} & T_{yy} & T_{yz} \\ T_{zx} & T_{zy} & T_{zz} \end{pmatrix} \begin{pmatrix} u_x \\ u_y \\ u_z \end{pmatrix}, \qquad \sigma_i = T_{ij} u_j \tag{A.8}$$

References

[1] H. Wensink. *Fabrication of microstructures by powder blasting.* PhD thesis, University of Twente, Enschede, February 2002. 130

[2] H. Wensink, H. V. Jansen, J. W. Berenschot, and M. C. Elwenspoek. Mask materials for powder blasting. *Journal of micromechanics and microengineering*, 10(2):175–180, June 2000. 130

[3] Creative Commons. https://isbibbio.wikispaces.com/gene+extraction; accessed january 2015. xxi, 134

[4] Wen-Tso Liu, Andrei D. Mirzabekov, and David A. Stahl. Optimization of an oligonucleotide microchip for microbial identification studies: a non-equilibrium dissociation approach. *Environmental Microbiology*, 3(10):619–629, 2001. 136

[5] A Loy, F Maixner, M Wagner, and M Horn. probebase - an online resource for rrna-targeted oligonucleotide probes: new features. *Nucleic Acids Res.*, 35:D800–D804, 2007. 136

[6] Invitrogen Detection Technologies. Molecular probes, http://tools. lifetechnologies.com/ content/sfs/manuals/ x21422.pdf. accessed: January 2015. 136

[7] Sigma-Aldrich. Sybr green product information. http://www.sigmaaldrich.com/content/dam/sigma-aldrich/docs/ sigma/datasheet/8/s9430dat.pdf, online. accessed: January 2015. 138

[8] Leica Microsystems. Leica dm ire2 and leica dm irb manual. http://loci.wisc.edu /files/loci/ dmire2_manual_1.pdf accessed: January 2015. 138

List of Symbols and Abbreviations

The following list is neither exhaustive nor exclusive, but may be helpful.

RPE ..... R-phycoerythrin

PNA ..... peptide nucleic acid

CE ..... concentration enhancement

DNA ..... deoxyribonucleic acid

ss-DNA ..... single stranded deoxyribonucleic acid

ds-DNA ..... double stranded deoxyribonucleic acid

Dyl-Strep ... Dylight labelled streptavidin

IHP ..... inner Helmholtz plane

OHP ..... outer Helmholtz plane

EP ..... electrophoresis

EO ..... electroosmosis

PI ..... isoelectric point

FWHM ..... full-width-half-maximum

TBE ..... tris-borate-EDTA

TAE ..... tris base, acetic acid, EDTA

FSA ..... field amplified stacking

CGF ..... conductivity gradient focusing

TGF ..... temperature gradient focusing

EFGF ..... electric field gradient focusing

CACE ..... counteracting chromatographic electrophoresis

ITP ..... isotachophoresis

MS ..... mass spectrometry

CZE ..... capillary zone electrophoresis

HPLC ..... high-performance liquid chromatography

ELISA ..... enzyme-linked immunosorbent assay

GEMBE .... gradient elution moving boundary electrophoresis

cIEF ..... capillary isoelectric focusing

ICP ..... ion concentration polarization

EDL ..... electric double layer

TFO ..... triplex-forming oligonucleotides

μ, ν ..... viscosity coefficient, kinematic viscosity coefficient

α ..... coefficient of thermal diffusivity

κ ..... coefficient of thermal conductivity

c_p, c_v ..... specific heat capacity at constant pressure, volume

c_i ..... molar concentration of species i

ρ_i ..... mass concentration of species i

ρ ..... density

D_i ..... Fick's law mass diffusivity (or diffusivity coefficient) of ith species

$\mathbf{u_i}$ ..... mass average velocity in fluids

$\mathbf{j_i}$, $\mathbf{J_i}$ ..... vector molar flux and mass average flux of a species i

m_i ..... mass of species i

p ..... pressure

D ..... diffusion coefficient

g ..... gravitational acceleration

K_n ..... Knudsen number

λ_{mfp} ..... mean free path, or interaction length

λ_s ..... slip length

ω_i, x_i ..... dimensionless density mass fraction, molar fraction

$\frac{D}{Dt}$ ..... material derivative aka. the convective derivative

$\mathbf{q}$ ..... vector rate of heat flow per unit area

$\mathbf{E}$ ..... vector of electric field

Φ ..... electrostatic potential

St ..... Strouhal number

Fr ..... Froude number

Re ..... Reynolds number

Pe_T, Pe_D .... Peclet number (thermal), (diffusion)

Pr ..... Prandtl number

St ..... Schmidt number

τ_{ij} ..... stress tensor components of i and j indices

τ ..... characteristic time (occasionally used)

σ ..... stress tensor

ϵ_{ij} ..... rate-of-strain components of i and j indices

p_e ..... charge density

ε_{ij} ..... permittivity

F_c ..... Faraday constant

z_i . . . . . valence of ion species i

ζ . . . . . zeta potential